Aerodynamic Design Optimization of a Flying V Aircraft

F. Faggiano

Registration number: 096#16#MT#FPP

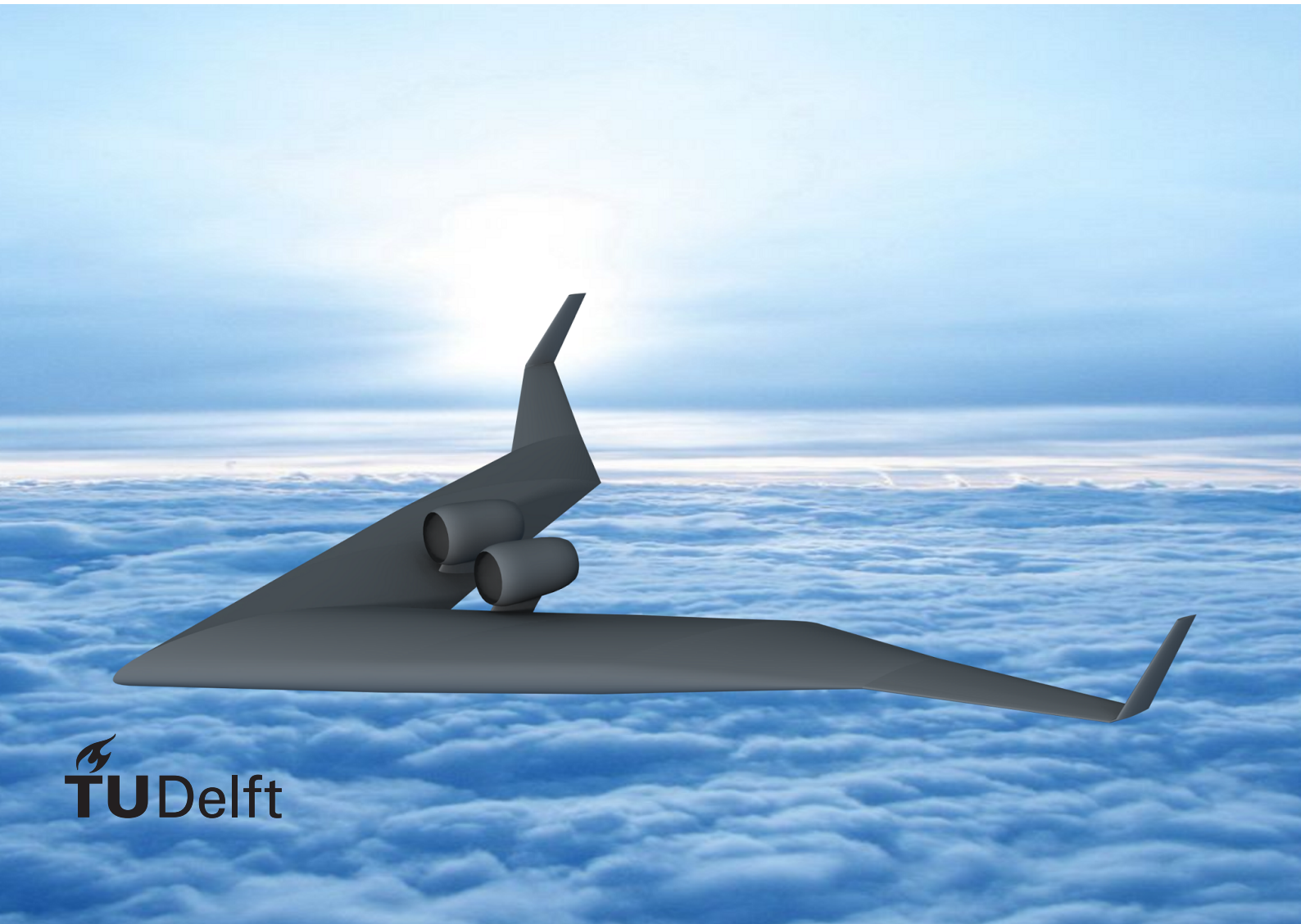

Aerodynamic Design Optimization of a Flying V Aircraft

by

F. Faggiano

to obtain the degree of Master of Science
at the Delft University of Technology,
to be defended publicly on Tuesday November 1, 2016 at 9:00 AM.

Student number:	4419308	
Project duration:	March 29, 2016 – November 1, 2016	
Thesis committee:	Dr. ir. R. Vos,	TU Delft, supervisor
	Prof. dr. ir. L.M. Veldhuis,	TU Delft
	Prof. dr. ir. S. Hickel	TU Delft

An electronic version of this thesis is available at `http://repository.tudelft.nl/`.

TU Delft

Summary

Lately, commercial aviation has been moving towards the reduction of environmental impact and direct operating costs, due to the rapid increase in aircraft demand and air traffic congestion predicted for the next years. Several researchers have been abandoning the fully exploited conventional configuration and exploring novel arrangements, such as flying wings and blended wing bodies. The Flying V concept, proposed at TU Berlin in collaboration with Airbus GmbH, represents the focus of this research project, since the preliminary analyses have estimated remarkable aerodynamic benefits and weight savings. It is a V-shape flying wing with two cylindrical pressurised cabins placed in the wing leading edge and engines over the trailing edge; elevons provide longitudinal control and vertical tails double as winglets. The primary research goal is the aerodynamic design of the Flying V aircraft to assess whether this concept has better aerodynamic performances than the reference conventional configuration during cruise. The design philosophy selected for this project consists of a multi-fidelity design space exploration followed by two different design paths: dual step optimization, where planform and airfoil variables are subsequently varied, and single step optimization. Athena Vortex Lattice is used to rapidly investigate the feasible design space, whereas the Stanford University Unstructured code in the Euler mode is adopted for an accurate wave and vortex-induced drag estimation. The profile drag is computed by a separate empirical module. The three-dimensional geometry is automatically generated within the ParaPy framework (a Knowledge Based Engineering environment) according to a multi-level parametrization: the wing planform shape is parametrized with 10 variables, the profiles with 43 parameters, and the winglets are defined by 3 additional variables. Subsequently, the unstructured volume grid is produced by the Salome platform wrapped in ParaPy and then fed into the aerodynamic solver. The aerodynamic design is performed at one single cruise condition: the Mach number is equal to 0.85, the lift coefficient to 0.26, and the altitude to 13,000 m. The baseline configuration is progressively improved: the wave and vortex induced drag components are reduced, the wetted area is slightly decreased and the pitching moment coefficient about the reference centre of gravity location is almost null. The maximum lift to drag ratio of the single step optimized configuration is 23.7 at the cruise point: this value confirms the estimation of 25 of the conceptual phase. A 12% reduction in subsonic drag is achieved, with the desired pitching moment. The Flying V is then compared to the NASA Common Research Model, a conventional configuration benchmark, by using the same solver and a similar mesh refinement. The maximum lift to drag ratio of the NASA Common Research Model is 18.9, hence the Flying V is 25% aerodynamically more efficient at the design cruise condition.

Acknowledgements

This master thesis project has been successfully accomplished thanks to the help and support of different people.

Foremost, I would like to thank my thesis supervisor Roelof Vos. He has provided me with remarkable support and high-quality feedbacks throughout the whole duration of the project. Without his critical comments and analytical attitude, this work would not have been so complete: he steered me in the best way, whenever I needed it.

Moreover, I would also like to acknowledge Klaus Bender, my thesis advisor from the Future Project Office at Airbus. The monthly meetings we had have been really productive and useful for my final piece of work. Besides, this project could not have been completed without the direct support of the ParaPy team, Reinier van Dijk and Max Baan. They introduced me to the software functionalities and provided constant support, every time it was required. A special thanks goes to Matteo Pini, who has given me valuable suggestions to get familiar with SU2 and tackle optimization problems. Also the Stanford team, managed by Juan Alonso, has been really available towards the end of the project.

I also would like to thank my other dissertation committee members, Stefan Hickel and Leo Veldhuis, for the insights that they provided. I really appreciate they have invested time and provided interesting and valuable feedback. I feel proud and honoured that they have accepted to be part of my committee.

Then, I am really glad I have shared the time of my master thesis with colleagues and friends. My special thanks go to the "guys" of *Via PelleRossi*, with whom I have shared great moments since we were kids, and the two "ladies" Cristina and Rita. They have provided unconditional advises and encouragement. Always present in my life and during my graduation days. And thanks to the really nice guys of *El Nuevo Latinoss* met at TU Delft. Finally, I am happy to thank my girlfriend Erika, always confident in my abilities, supporting me with her love from Italy during these challenging months.

Last but not least, I want to express my very profound gratitude to my parents and my brother, who guided me towards the best choices, encouraged me when I was losing confidence, and supported all my decisions from the beginning to the end. Their profound love, determination and confidence helped me to reach such a great achievement.

F. Faggiano
Delft, November 2016

Contents

Summary iii

List of Tables ix

List of Figures xi

1 Introduction 1
- 1.1 Problem Statement . . . 2
- 1.2 Research Objective and Questions . . . 3
- 1.3 State of the Art . . . 4
  - 1.3.1 Aerodynamic Design of Tailless Aircraft . . . 4
  - 1.3.2 Overview of Aerodynamic Analysis Methods . . . 6
  - 1.3.3 Aircraft Drag Breakdown . . . 6
- 1.4 Flying V Conceptual Study . . . 8
  - 1.4.1 Flying V Design Requirements . . . 8
  - 1.4.2 Current Configuration of the Flying V . . . 9
  - 1.4.3 Aerodynamic Design and Tools . . . 10
- 1.5 Outline . . . 11

2 Flying V Design Methodology 13
- 2.1 ParaPy Framework . . . 13
- 2.2 Program Workflow . . . 14
- 2.3 Aerodynamic Design Strategy . . . 16
  - 2.3.1 Wing Design . . . 16
  - 2.3.2 Twin Fins Design . . . 20
- 2.4 Multi Model Generator . . . 22
  - 2.4.1 Planform Variables . . . 24
  - 2.4.2 Oval Cross Section Cabin . . . 25
  - 2.4.3 Nose Cone Parametrization . . . 27
  - 2.4.4 Rear Airfoil Part Parametrization . . . 28
  - 2.4.5 Airfoil Variables . . . 29
- 2.5 Aerodynamic Analysis Module . . . 30
  - 2.5.1 Analysis Method . . . 30
  - 2.5.2 Unstructured Grid Generation . . . 32
- 2.6 Additional Modules . . . 34
  - 2.6.1 Performance Analysis . . . 34
  - 2.6.2 Payload Capacity . . . 34

3 Validation and Verification 37
- 3.1 Grid Convergence Study . . . 37
- 3.2 Grid Quality Assessment . . . 38

3.3 Aerodynamic Solver Validation and Verification . . . 40
3.3.1 Onera M6 Wing . . . 40
3.3.2 NASA Common Research Model . . . 42

4 Results and Discussions **47**
4.1 Test Case Description . . . 48
4.2 Multi-fidelity Design Space Exploration . . . 50
4.3 Dual Step Optimization . . . 53
4.3.1 SU2 Euler Planform Optimization . . . 53
4.3.2 SU2 Euler Airfoil Optimization . . . 54
4.4 Single Step Optimization . . . 56
4.5 Fin Sizing Results . . . 57
4.6 Aerodynamic Results Summary . . . 58
4.7 Results Comparison with NASA CRM . . . 59
4.8 From Conceptual to Preliminary Design . . . 60
4.8.1 Wing Planform Modification . . . 61
4.8.2 Cabin Cross Section Transformation . . . 61

5 Conclusions and Recommendations **63**
5.1 Conclusions . . . 63
5.2 Recommendations for Future Work . . . 64

Bibliography **67**

A Code Documentation **71**
A.1 Structure of the Code . . . 71
A.2 User's Input File . . . 74
A.3 Aerodynamic Discipline Class (*AerodynamicDiscipline*) . . . 76
A.3.1 AVL Analysis Class (*AVL*) . . . 77
A.3.2 SU2 Analysis Class (*SU2*) . . . 78
A.3.3 Fin Sizing Class (*FinSizing*) . . . 79
A.3.4 Viscous Drag Estimation Class (*ViscousDrag*) . . . 80
A.3.5 Nacelles Viscous Drag Estimation Class (*ViscousDragNacelle*) . . . 80
A.4 Performance Class (*Performance*) . . . 81
A.5 Payload Capacity Class (*PaxConfigurator*) . . . 81

B Relation between Vorticity and Entropy Jump in Inviscid Flows **83**

List of Tables

2.1 Twin fins driving requirements . . . 21
2.2 Wing planform Variables and values of the baseline configuration (0) . . . 25
2.3 Oval cross sections parameters: fixed values . . . 27
2.4 Design variables grouped in design vectors . . . 30
2.5 Fuel fractions for a typical flight mission, reported by Roskam [56] . . . 34
2.6 Values used in the payload capacity module . . . 35

3.1 Grid parameters selected for shape optimization analyses . . . 38
3.2 NASA CRM reference quantities [9]. * The values of the vertical tail are extracted from the CAD provide to NASA by ONERA[1] . . . 44

4.1 Flying V design conditions . . . 47
4.2 Test case: objective(s), constraints and design vectors of each design step . . . 48
4.3 Values of the design variables for the 5 configurations . . . 49
4.4 CST variables of the 5 Flying V configurations. Configurations 1,2,3 have the same values . . . 50
4.5 Summary of the aerodynamic coefficients based on the same reference area. Drag coefficients are expressed in counts and C_{D0} includes also fins, pylons and nacelles . . . 50
4.6 Fin design variables, bounds and optimum values. . . . 57
4.7 Aerodynamic results comparison between Flying V and NASA CRM. The drag coefficients are reported in counts . . . 60

A.1 User's input file description . . . 75
A.2 Aerodynamic discipline class . . . 76
A.3 AVL analysis class . . . 77
A.4 SU2 analysis class . . . 78
A.5 Fin sizing class . . . 79
A.6 Viscous module class for wing, fin and pylon profile drag estimation, based on the empirical equations outlined in Section 2.5.1 . . . 80
A.7 Viscous module class for nacelles profile drag estimation, based on the empirical equations presented in Section 2.5.1 . . . 80
A.8 Performance analysis class . . . 81
A.9 Payload capacity class . . . 81

List of Figures

1.1 Direct operating costs versus passenger seats [5] . . . 2
1.2 Range factor over the years [6] . . . 2
1.3 Flying V 3D geometry resulting from the conceptual study [8] . . . 3
1.4 Overview of numerical flow models from Navier-Stokes equations to linearised potential theory [27] . . . 7
1.5 Drag breakdown proposed by Mason [28] . . . 8
1.6 Flying V planform resulting from the conceptual study [8] . . . 9
1.7 Cabin cross section [8] . . . 10
1.8 Cabin layout [8] . . . 10

2.1 Flying V design application: top level structure . . . 14
2.2 Program activity diagram: geometry generation and aerodynamic assessment . . . 15
2.3 Flying V design strategy: top level structure . . . 17
2.4 Flying V design strategy. Multi-fidelity design space exploration (left) and optimization procedure (right) . . . 18
2.5 Streamwise profile with integrated cabin . . . 22
2.6 Flying V top view: streamwise profile sections on the left and cabin sections on the right . . . 23
2.7 Flying V outer mold line parametrization . . . 23
2.8 Flying V 3D model generated by the MMG . . . 24
2.9 Oval semi cross section cabin and acting forces [44] . . . 26
2.10 Flying V cabin cross section (from section 3 to 4) . . . 27
2.11 Front cone parametrization: representation of the root profile at varying coefficients a_{up} and e_{up} with fixed rear airfoil parameters . . . 28
2.12 Rear airfoil part at $y/c = 0$ at varying coefficients a_{low} . . . 29
2.13 Aerodynamic analysis module . . . 31
2.14 Grid computational domain with dimensions and boundaries (left) and example of coarse grid generated by ParaPy (right) . . . 33

3.1 SU2 grid convergence in terms of aerodynamic coefficients (M = 0.85, C_L = 0.26) . . . 38
3.2 Quality comparison between ParaPy and ICEM grids applied to the baseline configuration . . . 39
3.3 Onera M6 wing [58] . . . 40
3.4 Onera M6 wing: c_p distribution (x/c=0.2) . . . 41
3.5 Onera M6 wing: c_p distribution (x/c=0.44) . . . 41
3.6 Onera M6 wing: c_p distribution (x/c=0.65) . . . 41
3.7 Onera M6 wing: c_p distribution (x/c=0.80) . . . 41
3.8 Onera M6 wing: c_p distribution (x/c=0.9) . . . 42
3.9 Onera M6 wing: c_p distribution (x/c=0.95) . . . 42
3.10 Onera M6 wing drag polar (M=0.8395). Past investigations reported by Durrani and Qin [60] . . . 43
3.11 Geometry of the NASA CRM (right) and Boeing 777-200ER (left) [63] . . . 43
3.12 NASA CRM grid provided by SU2 Stanford team [61] . . . 45

4.1 Spanwise load distribution of the 5 configurations 50
4.2 Local lift coefficient distribution of the 5 configurations 50
4.3 Mach contours of the 5 configurations 52
4.4 Root effect improvement: the suction peak is moved forward and the pressure gradient is reduced 53
4.5 Local inviscid drag coefficient distribution of configurations 2,3 and 4 54
4.6 SU2 Euler airfoil optimization: comparison of pressure coefficient distributions at 6 spanwise locations 55
4.7 SU2 Euler single step optimization: comparison of pressure coefficient distributions at 4 spanwise locations (M = 0.85, C_L=0.26) 56
4.8 Drag polar of the 5 configurations. Limited lift coefficient are used 58
4.9 Maximum lift to drag ratio versus lift coefficient of the 5 configurations 58
4.10 Maximum lift to drag ratio versus pitching moment coefficient of the 5 configurations 59
4.11 Flying V planform comparison. The A350-900 planform is shown on the right hand side 61
4.12 Cabin cross section: from cylindrical (conceptual design) to oval 61

A.1 UML diagram of the Flying V design application developed within the ParaPy framework 72
A.2 ParaPy GUI: objects tree (top left), input management (bottom left) and geometry view (right) . 73

Nomenclature

Latin Symbols

$\frac{b_r}{b_v}$	Ratio between rudder and fin spans	-
$\frac{q_v}{q}$	Ratio between effective dynamic pressure at the tail and free stream one	-
$\frac{t}{c}$	Thickness to chord ratio	-
A_{avail}	Floor area available for passengers	m^2
A_{fin}	Fin (or winglet) aspect ratio	-
a_{low}	Coefficient a of the front cone lower curve	$\sqrt{\text{m}}$
a_{up}	Coefficient a of the front cone upper curve	$\sqrt{\text{m}}$
b	Wing span	m
c_r	Wing root chord	m
C_F	Skin friction coefficient	-
C_n	Yawing moment coefficient	-
c_{low}	Rear airfoil polynomial coefficient (lower curve)	$1/\text{m}$
c_{up}	Rear airfoil polynomial coefficient (upper curve)	$1/\text{m}$
C_{DO}	Profile Drag Coefficient	-
$C_{L_{\alpha_v}}$	Vertical surface lift slope	$1/\text{rad}$
$C_{L_{\text{cruise}}}$	Cruise lift coefficient	-
$C_{n_{\delta_{\text{ail}}}}$	Yawing moment derivative with respect to aileron deflection	$1/\text{rad}$
$C_{n_{\delta_r}}$	Yawing moment coefficient derivative with respect to rudder deflection	$1/\text{rad}$
$C_{n_{\beta_v}}$	Vertical surface yawing moment coefficient dericative	$1/\text{rad}$
D	Drag	N
d	Nacelle Diameter	m
D_{pax}	Number of passenger per square meter	$1/\text{m}^2$
e_{low}	Coefficient e of the front cone lower curve	$1/\text{m}^2$
e_{up}	Coefficient e of the front cone upper curve	$1/\text{m}^2$
FF	Form factor	-
H_1	Oval cabin top height	m
H_2	Oval cabin central height	m
H_3	Oval cabin low height	m
k_1	Kink relative position 1	-
k_2	Kink relative position 2	-
K_{FV}	Carry over effect due to the fuselage	-
L	Lift	N
l	Nacelle Characteristic Lenght	m
l_{engine}	Engine arm	m
l_{x_v}	Vertical tail arm with respect to the reference point	m
M	Mach number	-
M_{cruise}	Cruise Mach number	-

M_{ff}	Overall fuel weight fraction	-
n_{pax}	Passenger capacity	-
p_{cruise}	Air pressure at cruise condition	Pa
R	Range	m
Re	Reynolds number	-
S	Reference Area	m^2
S_{wet}	Wetted Area	m^2
T_{cruise}	Air temperature at cruise condition	K
T_{max}	Engine maximum continuous thrust	N
TP	Transition point in the cabin configuration	-
V	Speed	m/s
W	Weight	kgf
W_F	Oval cabin floor width	m
W_{cruise}	Cruise weight	kgf
W_{fuel}	Fuel weight	kgf
W_{to}	Take off weight	kgf
z_{TE}	Vertical position of the trailing edge of the rear airfoil	m

Greek Symbols

β	Sideslip angle	rad
δ_{r}	Rudder deflection	rad
ϵ_{IV}	Wing twist angle at section IV (kink 2) location	deg
ϵ_{V}	Wing twist angle at section V (tip) location	deg
γ	Heat capacity ratio	-
Λ	Sweep Angle	deg
λ	Wing taper ratio	-
Λ_1	Wing leading edge sweep angle 1	deg
Λ_2	Wing leading edge sweep angle 2	deg
Λ_{fin}	Fin (or winglet) leading edge sweep angle	deg
λ_{fin}	Fin (or winglet) taper ratio	-
ρ_{cruise}	Air density at cruise condition	kg/m^3
σ	Sidewash, difference in flow angle at the the vertical tail	rad
τ_{r}	Rudder angle of attack effectiveness parameter	-

1

Introduction

Over the last five decades, commercial aviation has been monopolised by the traditional tube-and-wing configuration. The main characteristics of a modern subsonic jet are embodied in the B-47, namely cylindrical fuselage, swept wing, rear empennage and engines podded under the wing, attached to pylons [1]. Many improvements in different disciplines, such as aerodynamics, propulsion, structure and avionics have been carried out: the efficiency of the airliners is 100% higher than 50 years ago, when modern jets flew for the first time [2, 3]. Nevertheless, the A380, which is a double-deck and long range jet airliner developed by Airbus, seems to represent an asymptote in terms of overall efficiency and payload capacity. In addition, manufacturers have to cope with a considerable commercial aviation growth predicted for the next decades (increase of 5% in overall revenue passenger-kilometre) and the consequent constraints related to environmental impact, pollution and noise [4]. Hence, different innovative design configurations have been lately explored with the aim of reducing the direct operating costs per passenger and the number of flights. For instance, Bolsunovsky et al. [5] claim that the flying wing (FW) concept represents a viable alternative to solve the above mentioned problems. A flying wing is a tailless fixed-wing airplane which does not feature a well-defined fuselage, therefore crew, payload, fuel, and equipment are typically placed inside the main wing. According to them, this unconventional design is beneficial since different tasks, namely providing lift, trimming the aircraft and accommodating people, are fulfilled by a unique integrated component. This entails a reduction in wetted area for the same payload, hence lower friction drag, which is one of the main drag contributions during cruise. In addition, the A380 already represents the limit in terms of size due to airport infrastructures: also in this particular field, flying wings are claimed to perform better, being smaller than tube-and-wing airplanes. In a nutshell, it is claimed that the direct operating costs per seat and mile can be especially reduced with a high capacity FW, as shown in Figure 1.1. Also Martinez-Val et al. [6] highlight the possible operational benefits of a 300 seats FW by using the range equation [7]. The so called range factor is plotted over the years in Figure 1.2: the trend shows improved aircraft performances of 100% over the last five decades and additional increase of 15-20% is claimed to be reached with the FW introduction.

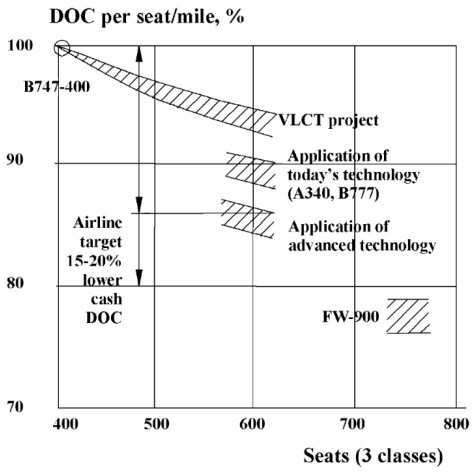

Figure 1.1: Direct operating costs versus passenger seats [5]

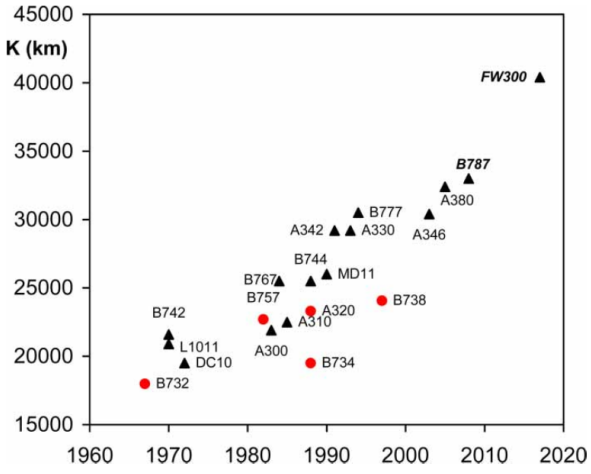

Figure 1.2: Range factor over the years [6]

1.1. Problem Statement

The basic FW concept has been investigated and modified by Benad [8] at Technishe Universitat Berlin and created in collaboration with the Future Project Office at Airbus GmbH (Hamburg, Germany). The result of the conceptual study is displayed in Figure 1.3: it is named Flying V Wing due to the noticeable V-shape planform. It features trailing edge elevons for longitudinal and lateral control, winglets (or fins) mounted on the wing tips and rudders to fulfil directional stability and control functions respectively. High lift devices are not included due to the excessive pitch down moment they introduce at low speeds. Two state of the art turbofan engines are placed over the wing trailing edge, relatively close to the symmetry plane of the aircraft. Unlike the usual cabin configuration of Blended Wing Body (BWB) and pure FW, which is far from being cylindrical, the Flying V is designed to have two cylindrical components, one in each semi wing: this arrangement is really beneficial to bear pressurization loads [7]. One may argue that such a cylindrical component inside a wing could either be purely efficient from a volume perspective or detrimental in terms of transonic wave drag, if the radius of the cylinder is big enough to house passengers; however, due to the high wing sweep, the cabin cut in the streamwise direction is an ellipse. This entails an efficient use of the volume of the wing without a huge structural penalty due to the cylindrical nature of the cabin. In terms of top level requirements, the objective of this new concept is to create a Flying V configuration with the highest lift to drag ratio and lowest structural mass in order to be competitive with the state of the art commercial aircraft, the A350-900. This also means comparable nominal range of 14,350 km, service ceiling of 13,100 m, cruise Mach number of 0.85, and passenger capacity of 440 passengers[1]. Since the A350-900 performance data is not available, the NASA Common Research Model (CRM) [9] is taken as a benchmark for the final comparison.

The Flying V design is at a conceptual stage: the aircraft weight is estimated by handbook methods and multiple assumptions, whereas drag is evaluated by vortex lattice methods and empirical correlations. The concept looks considerably promising: satisfactory gains in terms of drag and weight are estimated, which entail a 10% increase in lift to drag ratio [8]. This is the starting point and more sophisticated analyses are needed to assess the feasibility of the Flying V and confirm the initial estimations. Hence, this research project focuses on the aerodynamic design of the aircraft and it is tightly coupled with the structural design and weight estimation, concurrently performed by Luuk van der Schaft. A unique geometry generator for the outer mold line and internal structure is created and then integrated with aerodynamic analysis and structural sizing. It

[1] Dimensions & key data | airbus, a leading aircraft manufacturer. Retrieved in March 12, 2016 from http://www.airbus.com/aircraftfamilies/passengeraircraft/a350xwbfamily/a350-900/specifications/

is important to keep in mind that the design of tailless aircraft entails a tighter integration of the disciplines if compared to the conventional tube-and-wing airplane. Therefore, although this piece of work deals with the aerodynamic discipline, structural considerations and trim constraints are taken into account from the initial stages.

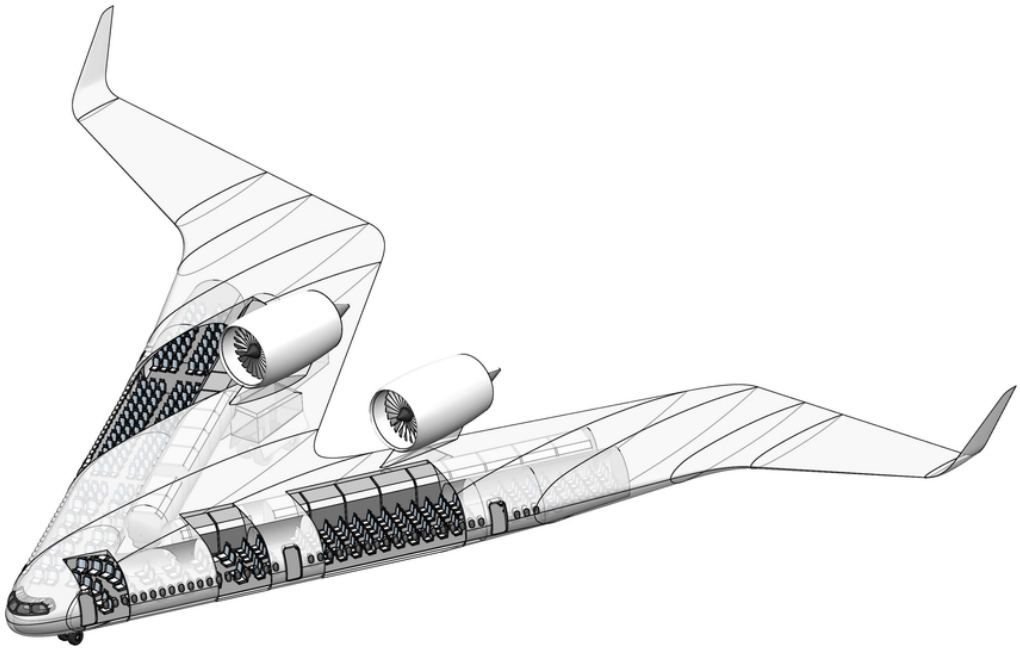

Figure 1.3: Flying V 3D geometry resulting from the conceptual study [8]

1.2. Research Objective and Questions

The main goal of the present research project is:

Performing the aerodynamic design of the Flying V and assessing how the cruise aerodynamic performances compare to the NASA CRM.

This objective is reached by:

- Creating a parametrized outer mold line of the aircraft.
- Coupling the geometry with a meshing tool.
- Analysing the geometry with a suitable aerodynamic solver.
- Setting a design strategy involving aerodynamic shape optimization.

Hence, the main research question is:

Does the Flying V concept boast aerodynamic advantages, as predicted by the preliminary assessment?

In order to answer the central question, it is required to acquire specific knowledge in multiple fields and solve the following sub-questions:

1. Is the conventional aerodynamic design approach (handbook methods) applicable to the Flying V? Or, on the other hand, what design strategy is needed?

2. What is the most suitable aerodynamic analysis method for the design of the Flying V configuration?
3. How can the Flying V three-dimensional geometry be parametrized?
4. What is the maximum lift to drag ratio achievable by the Flying V configuration?

The final outcome of this research project, namely an aerodynamic design method integrated with a geometry generator, is intended to be coupled with other disciplines design tools to accurately determine whether the Flying V will be more efficient than the tube and wing configuration. It is important to remark that the present work focuses on aerodynamic characteristics uniquely during cruise: therefore, low speed performances, field performances and maximum lift coefficient will be addressed by future projects if the results of the present analysis prove to be promising.

1.3. State of the Art

This section provides an insight into three main research areas: aerodynamic design strategies applied to tailless aircraft, aerodynamic analysis methods, and aircraft drag breakdown.

1.3.1. Aerodynamic Design of Tailless Aircraft

The Flying V concept follows the design philosophy of BWBs, FWs and lifting bodies, whose common characteristics are:

- Presence of a single lifting surface. No horizontal surfaces are included, thus static stability is guaranteed by placing the neutral point behind the centre of gravity and longitudinal control is provided by aerodynamic surfaces located on the wing trailing edge.
- Idea of using a unique component, the wing (or wing-body), to fulfil different tasks: providing lift and trim, and accommodating passengers.

Even though flying wings have been a topic of research and development for more than a century, they are still considered as novel and unconventional configurations. The dominant reason for the slow acceptance of this type of vehicles is related to stability and control issues, which limit the mission to the cruise one [10]. Also the non negligible structural penalty coming from the higher pressurization stress level proper of a non cylindrical fuselage, emergency evacuation design and passenger acceptance contribute to slow down the development of these concepts. On the other hand, many researchers point out remarkable aerodynamic and structural advantages due to the lower wetted area, interference drag and beneficial spanwise weight distribution, which relieves the wing root bending moment [3]. Also the decreased noise pollution represents a great advantage: the noise produced by the engines mounted over the trailing edge is shielded by the wing. The first projects date back to the 1930s with Lippisch and Horten and 1940s when Northrop worked on the prototypes of the YB-49 [1]. Lately, researchers have been working on two different tailless aircraft configurations: pure flying wings [1, 2, 4, 5, 11–15], characterized by straight leading and trailing edge, and blended wing bodies [16–21], which feature a smoothly blending of the wing into the body, where passengers are accommodated.

The aerodynamic design philosophy applicable to unconventional configurations is not straightforward due to the non-consolidated knowledge and experience [12]. This is in contrast with the solid expertise regarding the traditional wing design for transonic performances, as stated by Qin et al. [18]. In addition, the design of unconventional configurations entails a tighter integration of several disciplines: for instance, trim is not provided by the horizontal placed far behind, hence the wing pitch down tendency must be constrained in order to avoid a huge drag penalty. Furthermore, the lifting surface needs to have enough volume to store

fuel and payload and be aerodynamically efficient and structural resistant at the same time. Therefore, classical design methodologies based on empirical databases do not apply to the flying wing aerodynamic design. Since high-fidelity aerodynamic optimization has matured remarkably over the last 20 years, shape optimization procedures are extensively implemented to determine the best design. This allows to account for trim and structural design constraints from the initial stages and efficiently explore the design space. Here below, relevant projects from open literature are summarised.

Qin et al. [18, 19] implement a three steps approach within the MOB project on a BWB. Firstly, they use the so called twist inverse design method: they determine the required twist, for a given fixed planform and thickness distribution, in order to generate a certain spanwise target load (low-fidelity codes are employed for this purpose). Than, once the new lift distribution is validated with Merlin (a high-fidelity CFD code designed at Cranfield University), a 2D airfoil optimization for minimum drag is performed: the flow solver BVGK, which couples a full potential solution with a boundary layer solution, is employed for this purpose. The design variables for the optimization are 6 camber parameters for each airfoil (planform and thickness are fixed). Finally, Euler equations in combination with adjoint methods are used for a 3D surface optimization. Optimization procedures are performed with and without pitching moment constraints.

Mialon et al. [12] follow a different design philosophy at ONERA. They prefer to design the flying wing directly in 3D since they do not find any reliable rule which describes the correlation between 2D and 3D flow. Again, the procedure features three subsequent steps: they start by modifying the inboard wing to reduce the required trim force (I) and improving the pressure distribution outboard to avoid shock waves (II). After 37 iterations of modifications, they set up a systematic optimization procedure (III) to maximize the lift to drag ratio (3D surface optimization). The CANARI code, developed at ONERA, is used as a Euler solver coupled to boundary layer equations to account for viscous effects.

Li et al. [22] implement a multi-fidelity procedure: once the baseline geometry is defined, they explore the design space with the aid of low-fidelity codes in order to filter out the design points that do not satisfy aerodynamic and geometry constraints. Vortex lattice methods are used for induced drag, lift and moments, Korn equation for wave drag [23] and friction codes for viscous drag. Then a Reynolds-averaged Navier-Stokes solver is used for a CFD-driven optimization: planform optimization is the relevant aspect, whereas airfoil inverse design method is supplementary. It comes into play only if strong shock waves appear.

Aerodynamic shape optimization with high-fidelity tools is also applied by Reist and Zingg [21] to investigate the BWB configuration from regional to long range wide-body classes, and by Mader [15] to find the optimum flying wing design. The former use Reynolds-averaged Navier Stokes (RANS) equations and implement trim constrained analyses, whereas the latter focuses on stability constraints and uses Euler equations to capture transonic phenomena. The Euler flow model is also used by Zhang et al. [14] to maximize the lift to drag ratio of a BWB.

In a nutshell, the aerodynamic design philosophy applied to tailless aircraft is not based on empirical database, whereas involves aerodynamic shape optimization. Most of the projects follow stepwise procedures and multi-fidelity approaches: usually, low-fidelity codes are used in order to explore the design space and approach a feasible configuration, then more accurate analyses are carried out to find the optimum solution. Besides, some constraints, like trim, stability and deck angle, are implemented to account for other disciplines so that the final design complies with relevant top level requirements.

1.3.2. Overview of Aerodynamic Analysis Methods

During the aircraft design process, different methods are employed to assess its aerodynamic characteristics according to the required accuracy and computational cost. The viscous flow governing equations, the so called time dependent Navier-Stokes equations, are highly non linear and can not be solved analytically: numerical simulations are required. The different levels of possible simplifications of the Navier-Stokes equations are depicted in Figure 1.4. The complexity is maximum at the top and decreases progressively towards linear potential theory. As stated by Rumsey and Ying [24], direct numerical simulation (DNS) over realistic configurations are still beyond the capability of current computer; DNS and large-eddy simulations (LES) are not used in aerospace field at the moment, but they might emerge soon. In particular, according Deck et al. [25], DNS simulations applied to a civil airliner would require about 10^{16} grid points. Even with a supercomputer of 1 Teraflops, several thousand years would be needed. The industry has been focusing on Reynolds-averaged Navier-Stokes (RANS), Euler equations and simpler coupled Integral Boundary Layer (IBL) methods, namely potential flow panel approaches with integral boundary layer equations. The main obstacle of the practical use of LES remains computational resources [25].

RANS equations are based on the idea that, in turbulent flows, the field properties are described by random time and space functions: hence, the flow variables can be split in mean value and fluctuating contribution. Once these variables are substituted in the governing flow equations, a time average is applied and the RANS equations can be derived. Since 3 unknown quantities are introduced, namely the fluctuating contributions, the system of equations is not "closed": therefore, semi-empirical equations are used to model the turbulence and "close" the system. A detailed description of the turbulence models is beyond the scope of this piece of work. RANS equations can be further simplified by neglecting the viscous term as well as the heat transfer contribution, leading to the Euler model. This method assumes inviscid flow, hence it is not capable of predicting viscosity-related drag. The main advantage of this formulation, as shown by Vos et and Farokhi [26], is the capability of accurately predicting the shock wave appearance and its effect on the flow field: this is due to the fact that the flow is assumed to be rotational (the mathematical derivation is reported in Appendix B). Thus, Euler equations provide a good estimation of wave drag in transonic regime. This is the simplest method capable of capturing transonic phenomena since further simplifications are based on the irrotational flow assumption. In particular, potential flow equations assume steady, inviscid and irrotational flow with no body forces. Therefore, they do not model accurately transonic flows characterised by strong shock waves, in which the entropy jump is considerable, proper of rotational flows.

1.3.3. Aircraft Drag Breakdown

Different schemes are commonly adopted to subdivide the drag of an airplane. For instance, the near-field method splits the overall drag into pressure and friction drag: this approach is commonly used by aerodynamic solvers to estimate the overall force. It is based on the integration of normal and shear stress over the surface [28]. However, this method is not able to distinguish the fluid dynamics phenomena responsible for each drag component: therefore, an alternative drag breakdown, which accounts for different physical effects, is shown in Figure 1.5. According to this approach, the drag is divided into:

- **Profile drag**, which includes pressure and friction drag (components of the parasite drag) plus an additional 2D profile drag due to lift. These effects are associated with the flow viscosity, therefore can be accurately estimated by RANS and IBL; inviscid calculations must be combined with a separate empiric viscous module to take these contributions into account.

- **Induced drag**, which is caused by the lift related vorticity shed behind the wing trailing edge, where the airflow is deflected downwards; hence, it is usually estimated by analysing the vortex field behind the wing. The most common induced drag models are Trefftz Plane, Prandtl's lifting line theory and Vortex

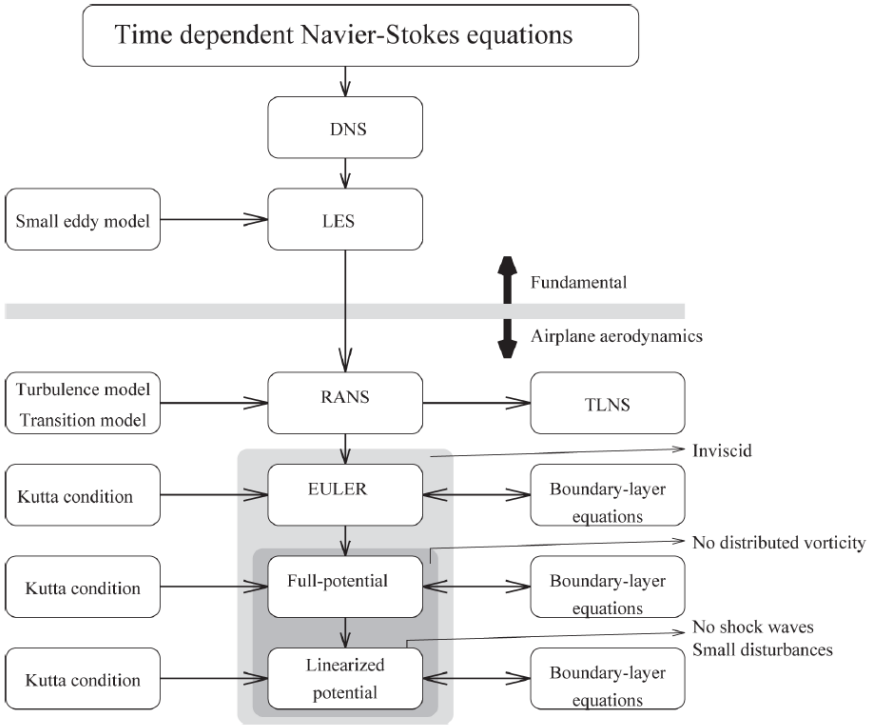

Figure 1.4: Overview of numerical flow models from Navier-Stokes equations to linearised potential theory [27]

lattice method (VLM) [29]. For instance, aerodynamic software like Athena Vortex Lattice (AVL) and Tornado are VLM.

- **Wave drag** appears when the flow becomes supersonic over the aircraft surface and compressibility effects can not be neglected, namely in transonic regime. This drag increase at high Mach numbers is due to shock waves generation, therefore it is an inviscid phenomenon. However, as pointed out by Vos et Farokhi [26], strong shock waves may lead to boundary layer separation (the so called *strong interaction*). Especially at relatively low Reynolds numbers, characterised by higher boundary layer thickness, the flow separates and this shock-induced separation is the main contributor to the exponential drag increase. This phenomena is not captured by inviscid calculations, therefore it is important to verify beforehand that this *strong interaction* does not take place, if boundary layer calculations are not included.

Trim drag is an additional contribution which arises from the need to balance the airplane in steady flight (zero pitching moment about the centre of gravity). In particular, the trim is provided by deflecting the control surfaces, thus increasing drag. In case of flying wings and blended wing bodies, in which the control surfaces are not located really aft with respect to the centre of gravity, trimming the vehicle can lead to considerable drag penalties. Trim drag includes induced and wave drag contributions.

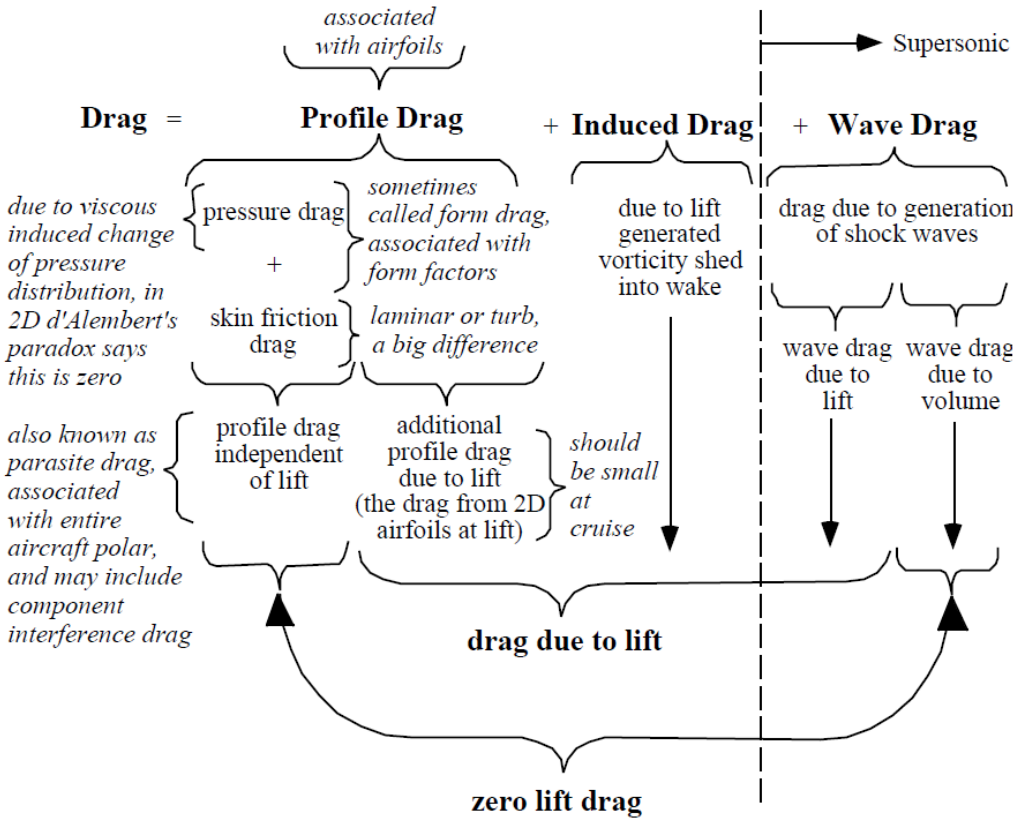

Figure 1.5: Drag breakdown proposed by Mason [28]

1.4. Flying V Conceptual Study

The Flying V concept aims to overcome some of the issues discussed in Section 1.3. Two cylindrical pressurized volumes are arranged in a V shape, placed in the leading edge of the wing: this requires a lower structural mass due to the reduced pressurization stress. Besides, it entails a shorter cabin length in the flight direction than the conventional configuration: this is desirable for a FW, in which a big centre of gravity range could be detrimental for trim and control. In addition, placing a tube parallel to a swept-back leading edge means that the cabin cuts through the streamwise direction in the shape of an ellipse: this arrangement allows a really efficient use of space within the wing. Not less importantly, the feature of the Flying V which makes it unique, namely the V shape, is also beneficial for trim purposes. The centre of gravity and neutral point are more forward if compared to a traditional BWB, since there is a "hole" in the rear part of the inboard wing. This increases the arm of the control surfaces, which are placed on the trailing edge of the outer part: thus, the cruise trim drag is lower due to smaller required elevon deflections.

1.4.1. Flying V Design Requirements

Beside the top level requirements mentioned in Section 1.1, the cabin, which is one the driving features for a commercial aircraft, must be designed according to the same constraints of the reference aircraft, the A350-900 [8]:

- Minimum head clearance over the seat closest to the wall: 1.6 m.
- Minimum head clearance in the aisle: 2.1 m.
- Economy class. Seat pitch: 81.28 cm. Seat width: 50.8. cm. Aisle width: 46.0 cm.

- Business class. Seat pitch: 152.4 cm. Seat width: 75.0 cm. Aisle width: 54.6 cm.

According to CS 25.815 (*Subpart D - Design and Construction* [30]), the passenger aisle width at any point between seats must equal or exceed 38 cm and 51 cm below and above 64 cm from the floor respectively. In addition, the span is limited according to the same aircraft code/group (provided by ICAO [31]) of the A350-900: it has to be less than 65 m. Additional qualitative constraints are set at the preliminary stage. They aim at the feasibility of the concept and must be taken into account during the subsequent analyses. They can be summarized:

- The level of passenger comfort must be as high as in existing configurations.
- The Flying V must be trimmable and longitudinally stable.
- It must comply with emergency evacuation regulations [30, 32];
- It must be able to take-off and land at existing airports and be compatible with ground infrastructure and gate restrictions.

1.4.2. Current Configuration of the Flying V

The planform resulting from the conceptual stage is displayed in Figure 1.6: it is possible to distinguish the inner wing, which contains the pressurized cabin, the outer wing and the winglets. The inner part span is set to 26 m, limited by the maximum acceleration sustainable by the passengers, whereas the aircraft span is restricted to 65 m by the gate limit (see Section 1.4.1). The sweep angle is set to 63° due to the following relevant considerations:

- The higher the sweep, the more stretched the cabin is in the streamwise direction. Therefore, a volume efficient solution can be attained with high sweep angles.
- The high thickness to chord ratio required to accommodate payload volume must be offset by sweeping the wing back. High sweep angles reduce the transonic wave drag.
- High sweep angles increase the distance between control surfaces and centre of gravity, the so called control arm. This solution is beneficial in terms of trim drag.

Further details concerning the aerodynamic shape are discussed in Section 1.4.3.

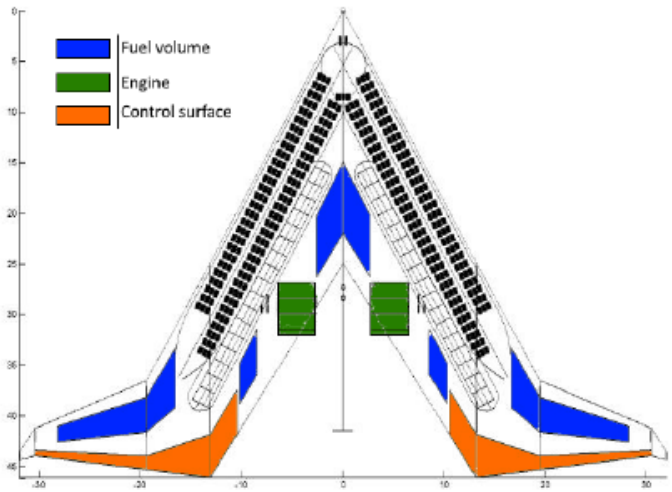

Figure 1.6: Flying V planform resulting from the conceptual study [8]

The cross section of the cabin deserves a special attention due its integration with the wing. A six abreast single aisle cabin must be fit in each of the semi-wings and the initial idea of having a circular section is partially abandoned. The chosen section is displayed in Figure 1.7: it is the result of the intersection of two arcs. The height to width ratio is 0.95, which is really close to 1: thus, the penalty given by the non cylindrical configuration is almost negligible. The red line indicates the cabin requirements mentioned in Section 1.4.1. The adopted cabin layout is really similar to the conventional one: due to the high sweep angle, the passengers orientation has a small angle with respect to the flight direction. In order to slightly increase the leg room, in the arrangement of Figure 1.8, the seats are partially turned towards the flight direction. The cargo holds are not placed under the belly like in the conventional configuration, but behind the pressurized cabin.

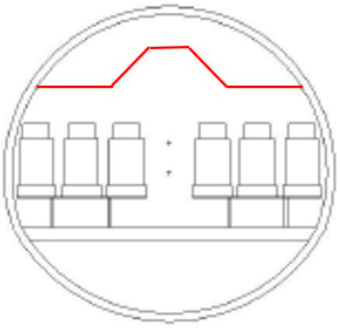

Figure 1.7: Cabin cross section [8]

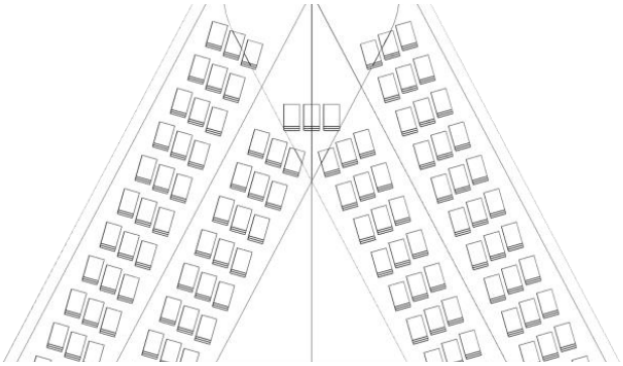

Figure 1.8: Cabin layout [8]

Two turbofan engines are positioned over the wing trailing edge. Although this solution provides noise shielding, it requires special attention due to the impact of engine longitudinal position on centre of mass location. Not less importantly, directional control has to be guaranteed in the one engine inoperative (OEI) condition: hence, also the lateral position of the engines is important. In addition, longitudinal and lateral control is fulfilled by elevons on the wing trailing edge; the winglets double as twin fins. Even though high lift devices are not taken into account during the conceptual design, further analyses must confirm that field performances are within the limits and stall speed is restrained.

1.4.3. Aerodynamic Design and Tools

The aerodynamic assessment tool used for the Flying V conceptual design is called ODILILA, developed by Klaus Bender at the Future Project Office (Airbus, Hamburg): it is a 3D vortex lattice method, employed for lift and drag estimations and also for control and stability derivatives calculations. Being based on potential flow theory, it is capable of assessing lift distribution and induced drag accurately; conversely, profile drag is not computed, hence empirical relations are incorporated in ODILILA to account for it. Also wave drag is not estimated by the code and the Prandtl-Glauert compressibility correction is used to include Mach effects.

Planform Shape

The planform has not been optimized, yet selected by engineering judgement. However, since limited changes in sweep angles, taper ratios and kink locations have a big impact on local lift coefficients, load distribution and wave drag, a dedicated planform optimization is needed.

Twist and Thickness Distributions

The twist distribution is estimated by optimizing the wing for minimum induced drag: this condition is obtained when the lift distribution is elliptical. The optimized wing has a washout moving towards the tip: this is needed to compensate the higher angle of attack of the outboard wing induced by the inner part. This trend

is also the result of many researchers working on pure FW and BWB: for instance, Qin et al. [18] use twist inverse design to gain three different favourable lift distribution and all the resulting designs show a nose down washout. The local lift coefficient is really important in terms of transonic performances: if it is too high, it may be an index of supersonic flow and a shock wave might appear. This would bring about a remarkable increase in wave drag, which has to be avoided during the design phase. In this case, the local lift coefficient is lower than 0.2 in the middle wing, which is claimed to be the most critical region due to the highest thickness to chord ratio, constrained by the cabin volume: the maximum relative thickness is 15.3%. This value is even lower than the 17% investigated by Qin [18] and Liebeck [16], thus wave drag is not deemed by Benad to be a big issue. However, the preliminary estimations are quite simplistic and some relevant parameters like relative thickness and cabin volume might have been underestimated. Therefore, it is important to further investigate the wave drag contribution.

Airfoil Shape

The airfoil investigation is preliminary: Benad [8] claims that the leading edge must be thick enough to accommodate the cabin without big drag penalty. Nevertheless, a conventional airfoil does not seem to be suitable for this purpose and a particular parametrization of the cross section is required for optimization: being the FW an integrated and synergistic design, the airfoil design has a strong effect on multiple disciplines.

Comparison with the Reference Aircraft

In order to prove the benefits of the Flying V configuration over the conventional one, the latter has been analysed with the same tool, ODILILA. The Flying V has an aerodynamic efficiency 10% higher than the tube-and-wing one. This scatter is claimed to originate from the lower wetted area of the chosen geometry, the winglets placed on the wing tips and the reduced mass. However, the area exposed to the flow is remarkably affected by the choice of the cabin height (and volume) and thus the airfoil thickness to chord ratio. Another challenge of highly swept wings is the taper ratio design of the transition and outer parts: low taper ratio increases the lift coefficient of the tip area, which may lead to nose-up pitching moment and loss of aileron effectiveness [33]. Also buffet characteristics are influenced by the outer shape, as stated by Qin et al. [19]. Furthermore, the sweep of the outer wing has to be investigated more thoroughly: a planform optimization is required.

1.5. Outline

This MSc project report is divided in different chapters. Chapter 1 contains an introduction of the research topic, inclusive of aviation background, problem statement and an outline of the research questions and goals. Moreover, it briefly presents the state of the art of unconventional configurations aerodynamic design, aerodynamic analysis methods and aircraft drag breakdown. Finally, it outlines the Flying V concept. In Chapter 2, the Flying V design methodology is thoroughly explained: the choice of the design framework, the aerodynamic design strategy, and the multi model generator are treated extensively. Besides, the choice of the aerodynamic analysis method is introduced and the grid generation is explained. The grid convergence study and quality assessment, validation and verification of the aerodynamic analysis tool are reported in Chapter 3. Subsequently, in Chapter 4, the results of the Flying V aerodynamic design are discussed. Furthermore, a comparison is provided in order to assess whether the Flying V is aerodynamically more efficient than the NASA CRM. Finally, Chapter 5 presents coherent conclusions of the MSc project and some recommendations concerning future studies.

2

Flying V Design Methodology

In this chapter, the Flying V design methodology is thoroughly explained and different aspects are extensively described. First of all, the design framework and the top level structure of the program are outlined. Subsequently, the aerodynamic design strategy, which represents the main core of the project, is explained. Then, the Flying V multi level geometry parametrization and the chosen aerodynamic analysis method are described.

2.1. ParaPy Framework

ParaPy [1] is the Knowledge Based Engineering (KBE) environment chosen for this research work. The platform is coded in Python, hence it presents its intrinsic features: it is simple to debug, encloses many built-in and third parties libraries and boasts a large community of users and developers. ParaPy is conceived for applications in which the automation of repetitive engineering activities may help in reducing cost and time. It incorporates two main features that make it suited for this piece of work:

- Open Cascade geometry kernel: it allows to create a 3D geometry by coding, rather than manually drafting it in a Computed Aided Design (CAD) software. This is computationally more efficient.
- Salome meshing tool: it supports automatic grid generation directly from the 3D geometry. The mesh can be fed into analysis programs (aerodynamic or structural solvers).

This environment collects KBE intrinsic features, which allow the automation of the design procedure by merging the object oriented language with CAD modelling, thus overcoming the lack of flexibility of current CAD systems and analysis tools [34]. La Rocca [35] outline some specific KBE features, namely:

- Runtime caching: the computed values are stored by the system and then reused without extra computation, as soon as the user requests them.
- Dependency tracking: this mechanism checks the validity of the values stored in the cache. If they are no longer valid, they need to be recomputed.
- Demand driven evaluation: objects are generated only on demand (lazy approach).

[1] ParaPy. Retrieved in September 15, 2016, from https://www.parapy.nl/

To summarize, ParaPy is selected due to the capability of automating repetitive tasks in a fast, efficient and demand-driven way (a), opportunity of re-using and maintaining classes (peculiarity of the object oriented approach) (b), the advantages of Pyhton language (c) and the wide range of possible applications (automatic geometry and grid generation, coupling with analyses tools, and support for Multidisciplinary Design and Optimization) (d).

The design method is implemented in ParaPy. The core of the design application is the multi model generator (MMG), which creates the Flying V geometry according to a limited set of user's input parameters (see Appendix A.2). Then, the aircraft geometry is fed into different analysis and sizing modules: the aerodynamic discipline is the focus of this project, whereas the structural sizing is concurrently performed. Two additional modules are built in order to create a top level design structure: the performance analysis class provides an estimation of the required fuel weight for a certain mission, aerodynamic efficiency and weight, whereas the payload capacity module calculates the amount of passengers that can be accommodated in the cabin, based on the given Flying V geometry and some statistical factors. The top level design structure is shown in Figure 2.1. An extensive documentation of the Flying V design application is reported in Appendix A.

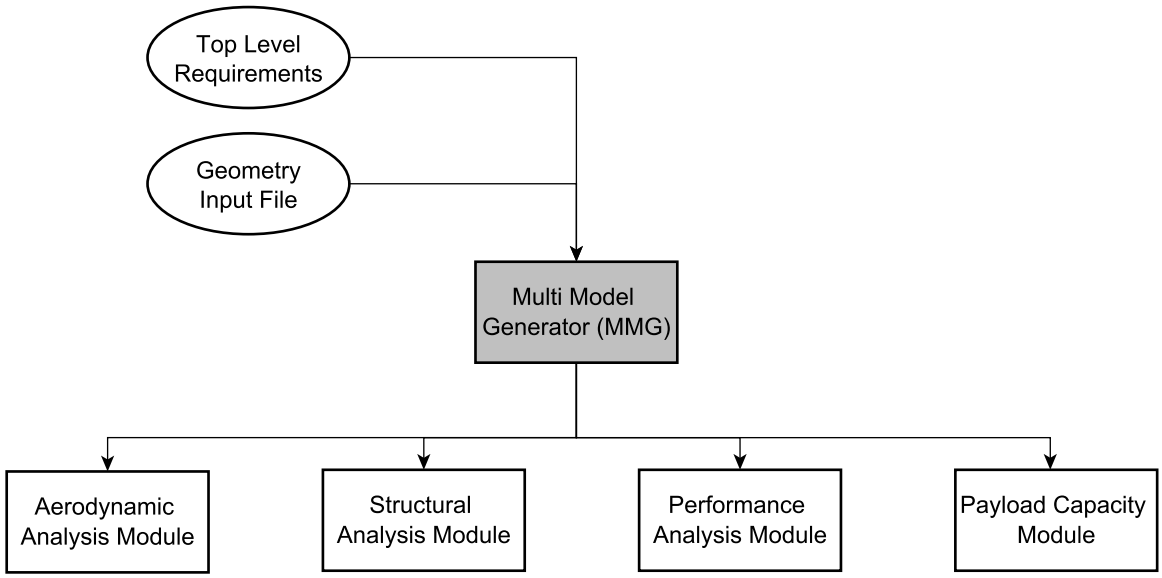

Figure 2.1: Flying V design application: top level structure

2.2. Program Workflow

The program workflow is explained through the activity diagram reported in Figure 2.2. This aims to display the sequence of the subsequent activities performed by the design application: the two main phases are the geometry generation workflow and aerodynamic analysis. This set of activities is then included in a design loop in order to find the optimum design (see Section 2.3).

When the user, for instance, requires the lift to drag ratio of the aircraft, a succession of activities starts. First of all, the geometry of the Flying V is created. In particular, the wing loft is built according to the following steps:

- The outboard profiles are created by the Class-Shape Transformation (CST) coefficients provided in the input file.

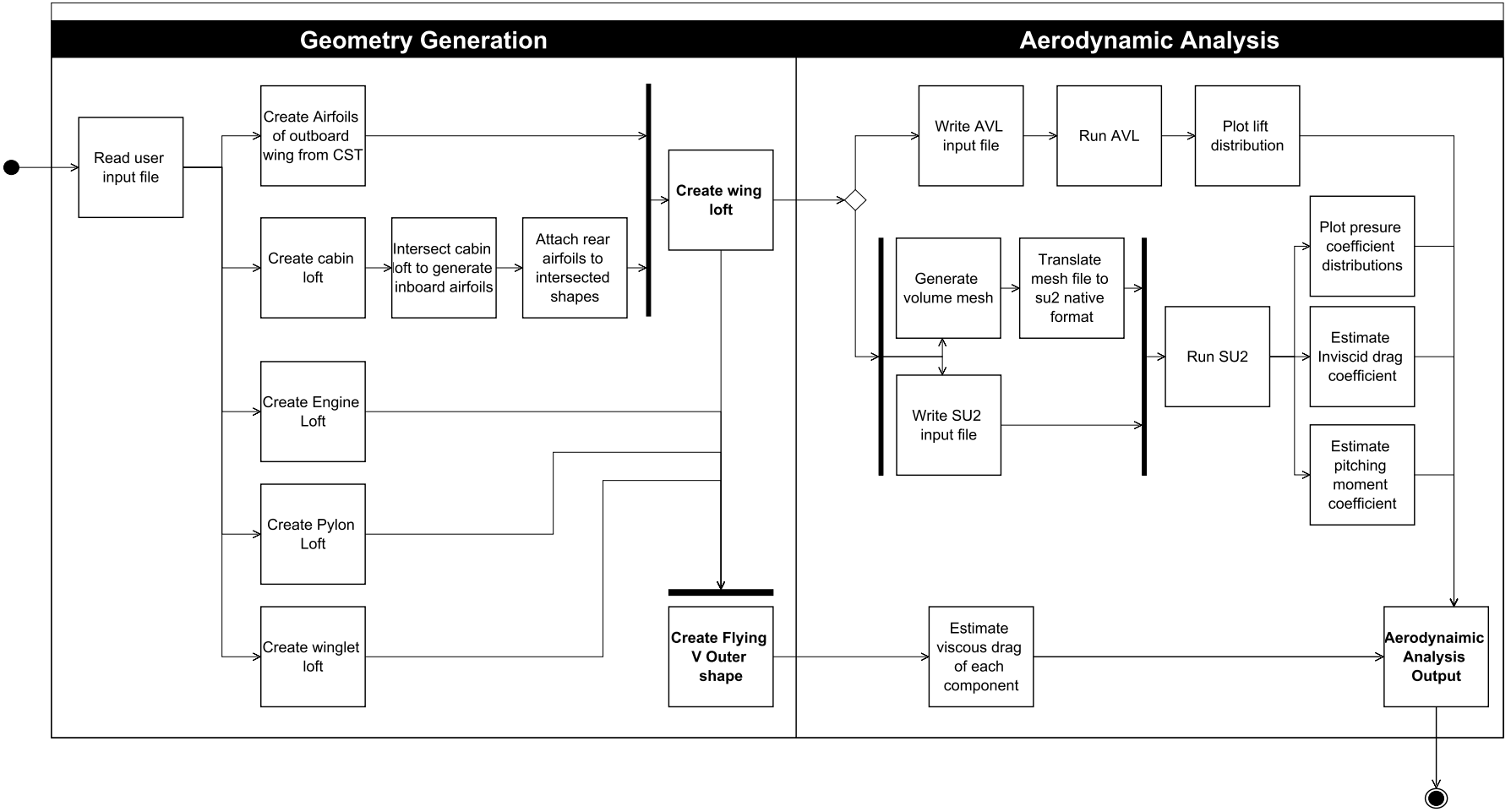

Figure 2.2: Program activity diagram: geometry generation and aerodynamic assessment

- The cabin loft is generated according to planform parameters and cabin sections variables, as explained in Section 2.4.
- The cabin loft is then intersected with 3 spanwise planes and a rear fairing is attached to each intersected shape in order to create the 3 inboard profiles. This guarantees that the inboard wing features a *single shell* structure.
- The wing (outer shape) loft is then created by linearly lofting inboard and outboard profiles.

In parallel, engine nacelles, pylons and winglets are built and the Flying V outher shape is created. It looks clear that the inboard part of the aircraft is driven by cabin parameters, whereas the outboard region has more freedom and is defined by CST coefficients. Geometry parametrization is thoroughly explained in Section 2.4.

Once the geometry of the Flying V is created, it is fed into the aerodynamic analysis module. The wing loft is analysed by AVL and Stanford University Unstructured (SU2) programs to have a quick representation of the lift distribution and accurate inviscid coefficients respectively. Then, the Flying V profile drag is estimated by empirical equations. Finally, the last activity of the program is the generation of the aerodynamic output in terms of numerical coefficients and graphical plots. The overall description of the aerodynamic analysis module is reported in Section 2.5.

2.3. Aerodynamic Design Strategy

In this section, the aerodynamic design strategy of the Flying V is thoroughly explained. It is commonly stated in open literature (see Section 1.3) that traditional empirical approaches do not apply to unconventional configurations due to the lack of knowledge and empirical database. Hence, shape optimization is used from the initial stages in order to determine the most efficient design. The design approach for the Flying V is divided into wing design and twin fins design, which are treated separately. They are explained in the following paragraphs.

2.3.1. Wing Design

The wing design strategy chosen for the Flying V follows a stepwise procedure, similarly to most of the open literature studies (see Section 1.3): it is depicted in Figure 2.3. Initially, multi-fidelity design space exploration is applied to the baseline configuration (0), then two different design paths are followed: a dual step optimization, which consists of planform and subsequent airfoil optimization, and single step optimization, where planform and airfoil variables are simultaneously varied. The dual step procedure is chosen in order to investigate the effect of the different variables on the aerodynamic characteristics and decrease the computational time. The single step optimization is tested and the resulting configuration (4) is compared to the dual optimized one (3). The twin fins are sized at the end of these procedures.

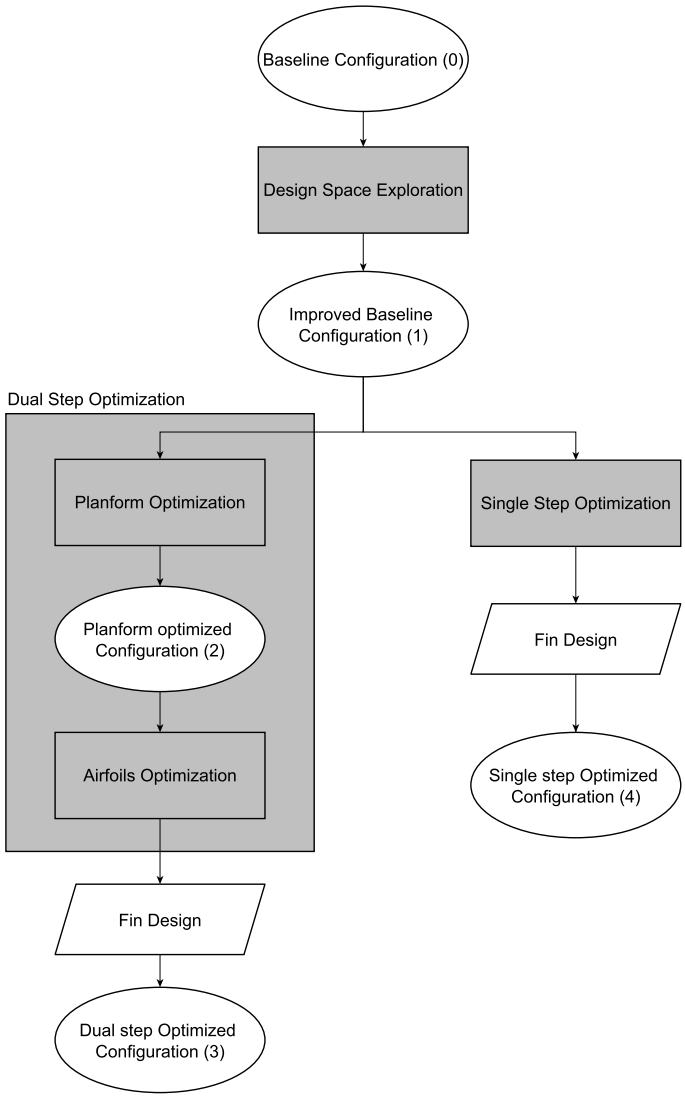

Figure 2.3: Flying V design strategy: top level structure

Multi-fidelity Design Space Exploration

The design space exploration is adopted to efficiently move towards the optimal configuration. It is an iterative procedure, characterised by two loops, as shown on the left hand side of Figure 2.4:

1. Internal low-fidelity loop, in which AVL is run for a certain design vector $\bar{y}$. Then, lift and local lift coefficient distributions are analysed, together with induced drag coefficient and pitching moment. If the results are satisfactory, the Euler solver is run to validate the case, otherwise the design vector is modified.

2. External Euler loop, in which SU2 is run when the results of the low-fidelity tool are promising. If induced drag coefficient and isobars look satisfactory to the designer, the procedure is assumed to be converged.

The design variables involved in the multi-fidelity design space exploration are reported in Table 4.2. It is important to remark that this is not an automatic procedure, yet the different iterations are done manually. However, since AVL takes few seconds to run, this multi-fidelity approach is computationally really efficient.

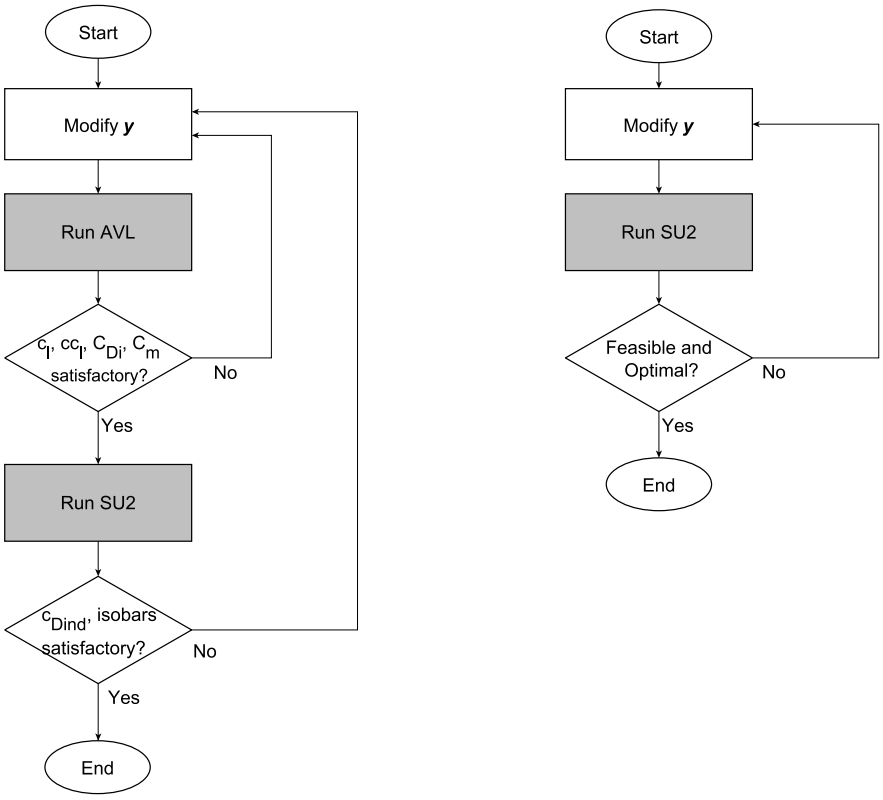

Figure 2.4: Flying V design strategy. Multi-fidelity design space exploration (left) and optimization procedure (right)

SU2 Euler Optimization

The SU2 Euler optimization procedure is drafted on the right hand side of Figure 2.4. This holds for the 3 procedures: planform, airfoil and single step optimization. It is a single-objective pure aerodynamic optimization, hence the goal is to maximize the Flying V lift to drag ratio (calculated by Equation (2.24)). In mathematical notation:

$$\begin{aligned} \min_{\bar{y}\in R^n} \quad & -L/D(\bar{y}) \\ \text{s.t.} \quad & \bar{g}(\bar{y}) \quad \leq \quad 0 \end{aligned} \tag{2.1}$$

Where $\bar{y}$ is the design vector, n the length of the vector and $\bar{g}(\bar{y}) < 0$ represents a set of inequality constraints. The design vector $\bar{y}$ and inequality constraints $\bar{g}(\bar{y})$ of each optimization step are reported in Table 4.2 of Chapter 4. Being a single-point design, the objective is to increase the aerodynamic efficiency at the the cruise condition, namely Mach 0.85, altitude of 13,000 m, and cruise weight estimated during the conceptual study.

The procedure is automatic: for each evaluation, the optimizer changes the design parameters and all the sequential activities explained in Section 2.2 take place. The optimization algorithm used for this research project is described in the following paragraph.

Optimization Algorithm

The optimization algorithm selected for the project is called Differential Evolution (DE), developed by Storn and Price [36]. It is a direct search algorithm capable of finding the global minimum of a multivariate function. In particular, this method is implemented in the *SciPy* optimization library, developed for the Python

programming language, hence it is easily integrated with the ParaPy framework. The main features that make it suited for this type of application are presented by Storn and Price [36]:

- Robustness and capability of handling non differentiable and highly non linear cost functions. For instance, if the geometry or grid are not well defined, the optimizer discards the solution without negatively affecting the optimum search. On the other hand, in a gradient-base approach, this would strongly impact on the gradient evaluation.
- Capability of finding global minima, by avoiding to get stuck into local minima, which is one of the drawbacks of gradient-based methods.
- Suitability for parallel computation, which is important for computationally demanding analyses.
- Ease of use, due to few control variables involved.
- Good convergence properties.

Differential evolution is similar to traditional evolutionary algorithms (EAs), which are population-based metaheuristic algorithms inspired by natural evolution. The optimization procedure can be divided into 4 main repetitive phases:

1. **Population generation.** A population P of size NP, which covers the entire design space, is generated according to Latin hypercube sampling (LHS). It can be expressed as:

$$\mathrm{P} = \{x_{(1,\mathrm{G})}, x_{(2,\mathrm{G})}, ..., x_{(\mathrm{NP},\mathrm{G})}\} \tag{2.2}$$

   In which, each individual $x_{(i,\mathrm{G})}$ is a the i^{th} design vector at generation G.

2. **Mutation**. For each design vector, a mutant vector is created according to:

$$v_{(i,\mathrm{G}+1)} = x_{(\mathrm{r1},\mathrm{G})} + \mathrm{F} \cdot (x_{(\mathrm{r2},\mathrm{G})} - x_{(\mathrm{r3},\mathrm{G})}) \tag{2.3}$$

   Where r1,r2,r3 are random indexes, integer and mutually different and F is a real and constant factor between 0 and 2, responsible for controlling the amplification of the variations. Increasing the mutation constant increases the search radius, but slows down convergence.

3. **Crossover**. Once the mutant vectors are created, new trial vectors are generated by exchanging parameters between mutant and reference vectors. The crossover is applied as follows:

$$u_{(ji,\mathrm{G}+1)} = \begin{cases} v_{(ji,\mathrm{G}+1)}, & \text{if (randb(j)<=CR) or j=rnbr(i).} \\ x_{(ji,\mathrm{G})}, & \text{if (randb(j)>CR) or j} \neq \text{rnbr(i)} \end{cases} \tag{2.4}$$

   In which randb(j) is the evaluation of a uniform random number generator, whose output is between 0 and 1 and rnbbr(i) is a randomly chosen index which ensures that the trial vector is not equal to either the reference or the mutant one. CR is the crossover constant between 0 and 1: it controls the diversity of the perturbed parameter vectors.

4. **Selection**. This is the last phase, in which the trial and reference vector are compared by evaluating the cost function. The one that yields a smaller value becomes member of the next generation.

These steps are repeated until the convergence criteria are met, namely tolerance on the cost function or maximum number of iterations.

In constrained optimization problems, a method to bind the feasible regions must be found. A common approach used for metaheuristic algorithms is the adoption of penalties when a non feasible region is entered, as proposed by De Melo and Carosio [37]. In mathematical terms:

$$f(\bar{x}) = \begin{cases} \text{objfun}(\bar{x}), & \text{if } \bar{x} \in \text{F}. \\ \text{objfun}(\bar{x}) + \text{penalty}, & \text{otherwise}. \end{cases} \tag{2.5}$$

Where F indicates the feasible design space. Since the *SciPy* function handles minimization problems, the penalty value added to the cost function is very high (1e10). In this way, an unfeasible solution is discarded and removed from the population in the next iteration. This approach is quite simple and effective at the same time. The results of the work performed by De Melo and Carosio [37] put DE with simple penalty function to handle constraints as a top performer in the two engineering problems they have worked on.

2.3.2. Twin Fins Design

In this section, the twin fins design procedure is outlined. According to Obert [38], tail surfaces in general must accomplish three main tasks:

1. Fulfil static and dynamic stability functions.
2. Provide aircraft control.
3. Trim the aircraft in each flight condition.

These functions can be translated into design requirements.

Driving Requirements

The three driving requirements that have to be satisfied are:

1. **Directional static stability**, which means that the forces created by a disturbed state push the aircraft back to its original state. This condition is satisfied by a positive yawing moment coefficient derivative with respect to sideslip angle. This can be expressed as:

$$C_{n_\beta} > 0 \tag{2.6}$$

In which C_n is the yawing moment coefficient, positive to the right, and β the sideslip angle, positive when the right wing is windward. Adding two vertical surfaces behind the centre of gravity has a stabilizing effect. The minimum yawing moment derivative of 0.0005 1/deg [39] is set as a directional stability target. The yawing moment derivative in tail-off condition is evaluated by SU2, since the empirical values proposed by handbook methods are not suitable for such a configuration. The fins contribution is then evaluated as:

$$C_{n_{\beta_\text{v}}} = C_{L_{\alpha_\text{v}}} \left(1 + \frac{d\sigma}{d\beta}\right) \frac{q_\text{v}}{q} K_\text{FV} \frac{S_\text{v} l_{x_\text{v}}}{Sb} \tag{2.7}$$

Where $C_{L_{\alpha_\text{v}}}$ is the vertical tail force slope, σ the sidewash, namely the difference in flow angle at the tail, $\frac{q_\text{v}}{q}$ is ratio between effective dynamic pressure at the tail and free stream one, K_FV is the carry-over effect due to the fuselage and l_{x_v} is the arm of the tail aerodynamic centre with respect to the reference point. This relation holds for a conventional configuration, in which the flow encountering the tail is heavily influenced by wing, body and horizontal tail. This is not the case of the Flying V, in which the fins are placed over the wing tips: the flow is deemed to be almost undisturbed, the only effect is the interaction with the wing. The so called end-plate effect is accounted by using the effective aspect ratio, rather than the geometric one, in the lift slope calculation [40]. The value of $C_{L_{\alpha_\text{v}}}$ as function of aspect ratio, taper

ratio, and sweepback can be either deduced by the graph proposed by Campbell and McKinney [41] or estimated based on empirical relations [40]. The latter approach is chosen in order to easily automatize the procedure. Dynamic stability is not analysed at this stage. Eventually, yaw dampers can be included in order to reduce the Dutch roll mode.

2. **One engine inoperative (OEI) condition at take off**, in which the control forces must balance the yawing moment generated by the engine operating at a high thrust setting. The aircraft must be able to sustain a zero angle of sideslip at take-off speed at the most aft centre of gravity position, considered as the worst case scenario [40]. The rudder deflection to balance the aircraft should not exceed 20°, so that additional manoeuvring is allowed within rudder deflection limits. Thus, from the equilibrium equation and assuming zero sideslip and zero aileron deflection, the required rudder deflection can be calculated as [42]:

$$\delta_r = \frac{T_{max} \cdot l_{engine}}{C_{n_{\delta_r}} qSb} < 20° \tag{2.8}$$

Where T_{max} is the maximum continuous thrust, l_{engine} is the engine arm and $C_{n_{\delta_r}}$ is the yawing moment coefficient derivative with respect to rudder deflection. The engine maximum continuous power is the one of the reference engine, Trent XWB 84, namely 317.6 KN [43], whereas the take-off speed taken into account comes from the reference aircraft, 150 kts [8]. The rudder deflection derivative is calculated based on Sadraey approach [42]:

$$C_{n_{\delta_r}} = -C_{L_{\alpha_v}} \frac{S_v l_{x_v}}{Sb} \frac{q_v}{q} \tau_r \frac{b_r}{b_v} \tag{2.9}$$

In which, τ_r is the so called rudder angle of attack effectiveness parameter, which depends on the ratio between rudder and fin chord, whereas $\frac{b_r}{b_v}$ is the ratio between rudder and fin spans.

3. **Landing in maximum crosswind condition**, when the wind speed equals 20% of the take-off speed: this corresponds to an angle of sideslip of 11.5°. Again, the rudder deflection should not exceed 20°. From the equilibrium about the z-axis:

$$\delta_r = -\frac{C_{n_\beta} \beta}{C_{n_{\delta_r}}} < 20° \tag{2.10}$$

The aileron deflection impact is not considered at this stage, since the aileron-induced adverse yaw strongly depends on aileron design and differential deflection. This means that the yawing moment derivative with respect to aileron deflection $C_{n_{\delta_{ail}}}$ can be either positive or negative. In addition, this contribution is considered small with respect to the other two terms of Equation (2.10).

Generally speaking, in case these requirements (summarised in Table 2.1) are not met, the brute-force method suggests to increase the vertical surface area, but this has a negative impact on weight and drag. Other solutions could be moving the engine inboard, or increasing the rudder chord and span to improve its effectiveness [40]. In Table 2.1, the fin driving requirements are summarised.

Requirement	Description	Criteria
Directional static stability	The yawing moment induced by the sideslip must push the aircraft back to the initial state	$C_{n_\beta} \geq 0$
OEI condition at take off	When one engine fails, the aircraft must be able to balance the asymmetric thrust ($\beta = 0°$)	$\delta_r \leq 20°$
Crosswind landing	An aircraft must be balanced during landing at 11.5° sideslip	$\delta_r \leq 20°$

Table 2.1: Twin fins driving requirements

Design Procedure

The twin fins design procedure applied to the Flying V is simple and straightforward. The candidate fin is the smallest one which satisfies the driving requirements explained in the previous paragraph in order to minimize zero lift drag, which is proportional to wetted area. Hence, the cost function is the fin area and the constraints are represented by the driving requirements. The design variables are aspect ratio, leading edge sweep angle and taper ratio. In mathematical notation:

$$\begin{aligned} \min \quad & S_{\text{fin}}(\Lambda_{\text{fin}}, A_{\text{fin}}, \lambda_{\text{fin}}) \\ \text{s.t.} \quad & C_{n_\beta} \geq 0 \\ & \delta_{\text{r}}^{\text{OEI}} \leq 20° \\ & \delta_{\text{r}}^{\text{CW}} \leq 20° \end{aligned} \tag{2.11}$$

The rudder is assumed to be full span and the chord ratio is 0.3. The lift slope is mainly dependent on aspect ratio [38], whereas the sweep angle has a non-negligible impact on fin arm. Therefore, since it is a pure aerodynamic optimization, tight bounds on the variables are required to prevent a high sweep angle and low taper ratio. Again, the DE optimization algorithm is used.

2.4. Multi Model Generator

This section provides an overview of the structure of the multi model generator and a description of the design parameters. The concept proposed by Benad [8], described in Section 1.4, envisions a *single shell* structure, which is able to carry pressurization stresses but also aerodynamic and inertia loads. In particular, a cylindrical passenger cabin is placed in the wing leading edge and an additional cabin compartment is located behind it. Even though this layout is optimal for structural reasons, it does not allow for enough design flexibility. As an alternative, the oval cross section proposed by Vos et al. [44] represents a viable solution. The oval section provides more design flexibility than the cylindrical one: it is defined by 4 variables. Moreover, being the cabin shells parallel to the highly swept leading edge, the cabin cut in the streamwise direction resembles a stretched ellipse: this solution proves to be volume efficient. The two streamise profiles with the integrated cabin shells are shown in Figure 2.5. In addition, the aerodynamic performances of this new configuration are not penalised due to the relatively low thickness to chord ratio involved. This is the concept intended to be used for the Flying V and will be further explained in Section 2.4.2.

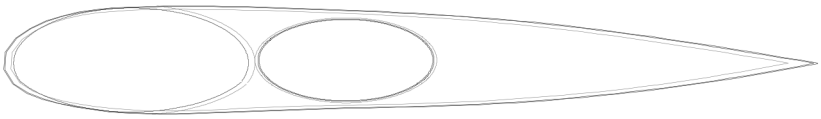

(a) Conceptual design [8]

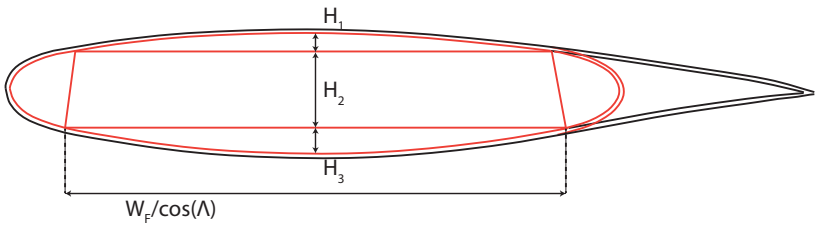

(b) New solution with oval cross section

Figure 2.5: Streamwise profile with integrated cabin

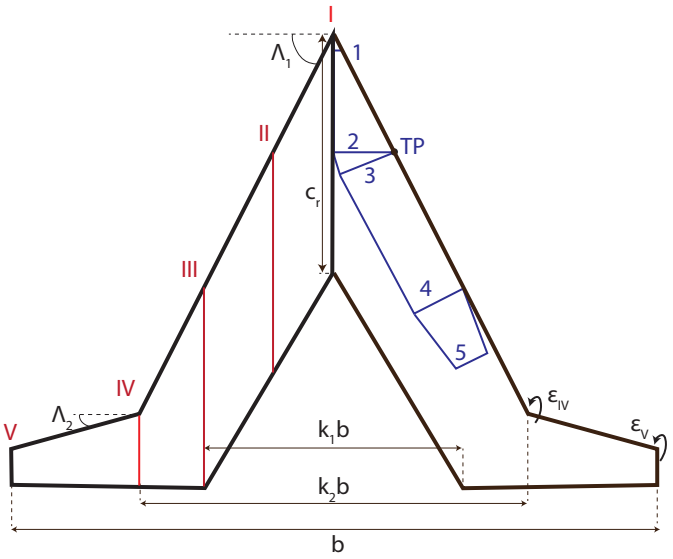

Figure 2.6: Flying V top view: streamwise profile sections on the left and cabin sections on the right

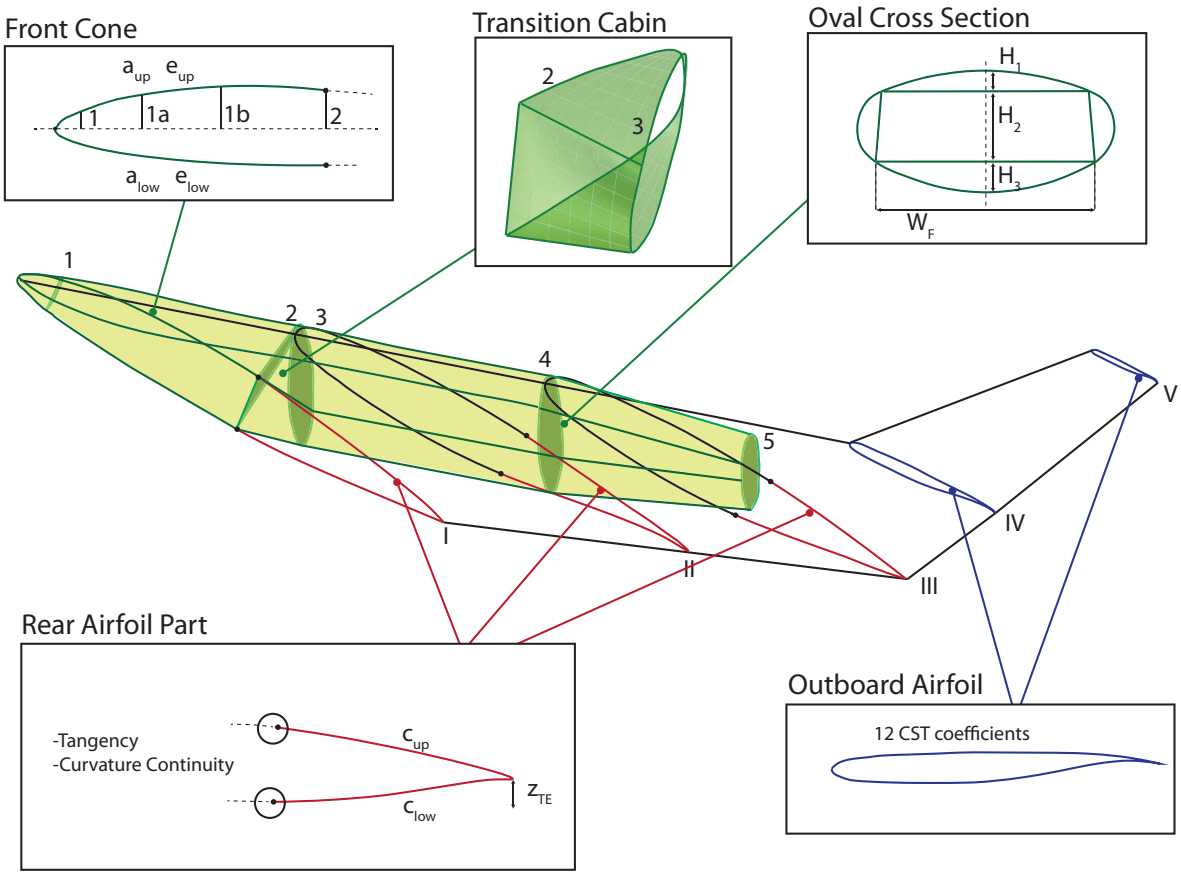

Figure 2.7: Flying V outer mold line parametrization

The cabin configuration is shown in Figure 2.6 (blue): the oval cross sections are perpendicular to the leading edge (from sections 3 to 4) until a certain point, called transition point (TP) for sake of simplicity,

where they become perpendicular to the flight direction (as Vos et al [44] envision the concept). This means that, in the nose cone (from sections 1 to 2), the wide oval cabin is cut in its middle point by the center line. Hence, there is a transition region (from sections 2 to 3) in which the cross sections rotate. The segment from sections 4 to 5 is not a single shell, yet it is created such that it fits within the outer skin.

In terms of outer mold line parametrization, 10 planform design variables are defined to control the planform shape of the wing and additional 3 parameters define the fins. They are presented in Section 2.4.1. Then, regarding the cross sections, the inboard part (where the passengers are allocated) is cabin driven, whereas the outboard region is really similar to the wing of a conventional configuration. The multi-level parametrization is displayed in Figure 2.7. The oval cabin parameters are discussed in Section 2.4.2, the nose cone variables in Section 2.4.3, the rear airfoil part parametrization is explained in Section 2.4.4 and the outboard airfoil one in Section 2.4.5. The engines of the reference aircraft, namely Trent XWB 84, are considered. Furthermore, a preliminary shape of the pylon is determined to account for the wetted area increase, which has a non negligible impact on profile drag. No dedicated analyses on engines and pylons are included. The control surfaces are not included in the MMG at this stage. An example of the Flying V complete geometry created by the MMG is displayed in Figure 2.8.

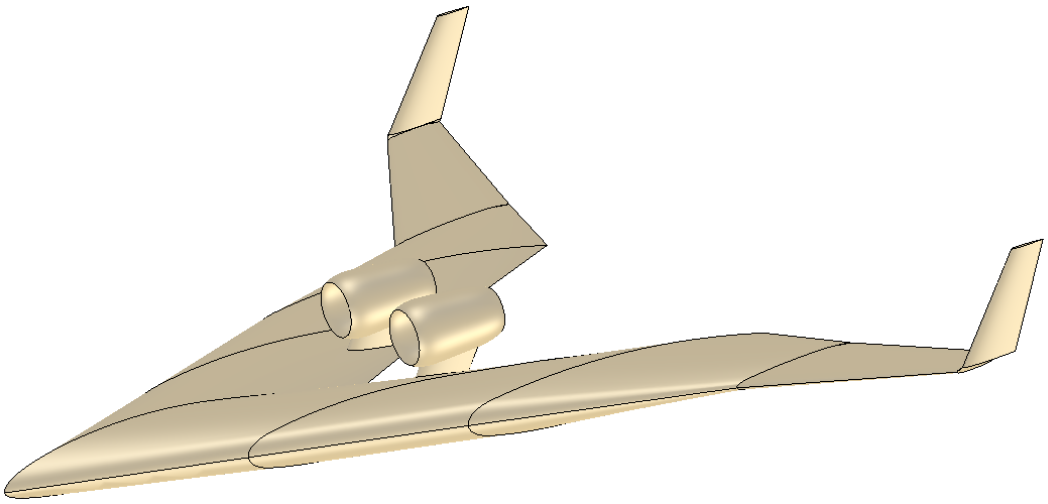

Figure 2.8: Flying V 3D model generated by the MMG

This integrated parametrization of outer mold line and internal cabin configuration proves to be beneficial for the Flying V design for two main reasons. First of all, the shape resulting from the aerodynamic optimization procedures is compatible with the internal cabin, hence it is a feasible configuration. Certainly, the freedom of the single shell region is partially limited. In addition, such a parametrization is more suitable for MDO involving structural design since it can easily couple outer shape with cabin structure.

2.4.1. Planform Variables

The planform can be viewed as the two-dimensional shadow of the airplane and it is usually the starting point for the creation of the three-dimensional aircraft body, as stated by Kim et al. [45]. The planform has to be uniquely defined by a set of independent design variables. This implies that when a single (or multiple) parameter is modified by the designer, the whole planform changes accordingly. The parametrization proposed for the Flying V follows the common philosophy recommended in open literature [15, 18, 19, 21]: it includes sweep angles, chords and twists at different locations, and spans of different wing segments. The twist angles

Design Variable	Symbol (unit)	Initial value
Surface area	S (m^2)	895.0
Span	b (m)	65.0
Root chord	c_r (m)	24.0
Leading edge sweep angle 1	Λ_1(°)	63.0
Leading edge sweep angle 2	Λ_2(°)	15.0
Kink relative position 1	k_1 (-)	0.400
kink relative position 2	k_2 (-)	0.600
Taper ratio	λ (-)	0.18
Twist kink 2	ϵ_{IV} (°)	-1.5
Twist tip	ϵ_V (°)	-1.0

Table 2.2: Wing planform Variables and values of the baseline configuration (0)

are defined only for the outboard sections IV and V (Figure 2.6) because the inboard ones are driven by cabin sections parameters. In particular, the cabin floor is constrained to be level at zero angle of attack. Besides, the design parameters are chosen based on the assumption that the planform features two kinks: the inner trailing edge kink and outer leading edge one. The design variables of the wing planform and the initial values are reported in Table 2.2.

Within this planform, several defining spanwise sections have been identified: they are shown in Figure 2.6 and their parametrization is discussed in Sections 2.4.2 to 2.4.5. Section I is congruent with the wing root; section II is positioned at the TP location (see Figure 2.6), where the transition cabin ends. The trailing edge kink determines spanwise section III, whereas the leading edge kink defines spanwise section IV. The wing tip is defined by section V and the winglet, which is not displayed, ends at section VI.

The wing planform variables, reported in Table 2.2 and shown in Figure 2.6, are the optimization variables of the test case described in Chapter 4. Moreover, three additional variables are used to define the fin (or winglet) planform shape: aspect ratio (A_{fin}), leading edge sweep angle (Λ_{fin}) and taper ratio (λ_{fin}). The fin root chord is assumed to equal the wing tip chord. At this stage, the fin is constrained to be vertical, since the span already equals the gate limit mentioned in Section 1.4.1. These are the design variables used in the twin fins sizing procedure, explained in Section 2.3.2.

2.4.2. Oval Cross Section Cabin

As mentioned before, Vos et al. [44] have investigated a new cross section, able to bear loads via in plane loading, the so called wide oval cabin. At the same time, this innovative design takes into account passenger comfort since no vertical pillars are positioned inside the cabin. As shown in Figure 2.9(a), the section is characterised by four arcs of different radii smoothly connected to each other: thanks to its geometry, although the radii are different, the transition is smooth. The working principle is the following: when the cabin is pressurized, the horizontal panels carry the compression load, whereas the side panels are in tension (see Figure 2.9(b) and Figure 2.9(c)). The panels also fulfil the function of a wing box, carrying the torque loads. It has been shown that this concept is structurally efficient and allows for specific tailoring to satisfy cabin requirements. Especially for such an integrated design, it combines good flexibility and structural efficiency.

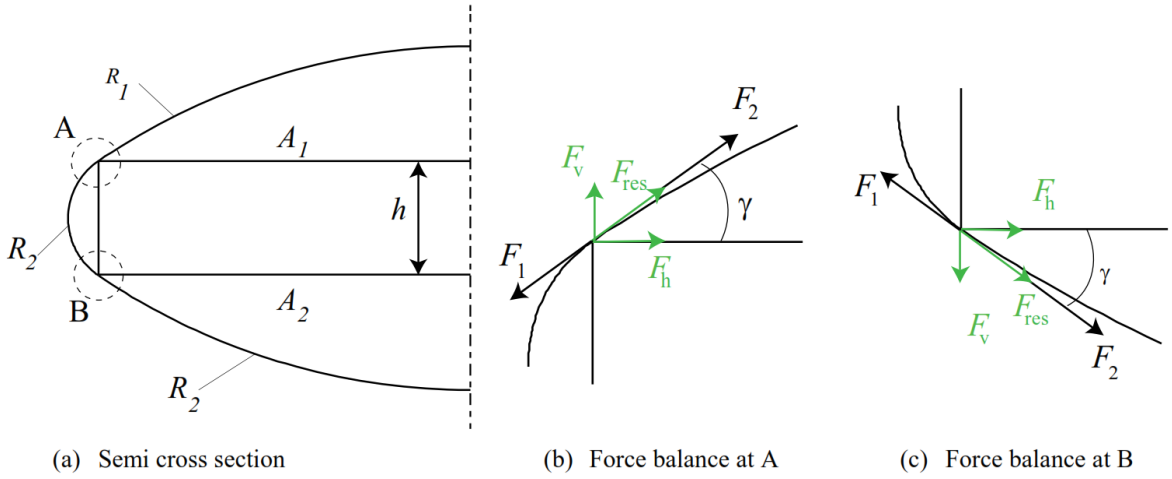

(a) Semi cross section (b) Force balance at A (c) Force balance at B

Figure 2.9: Oval semi cross section cabin and acting forces [44]

In order to fully define the oval cross section in the symmetric case, 4 variables are required (they are displayed in Figure 2.7):

1. H_1: top height;
2. H_2: central height;
3. H_3: low height;
4. W_F: floor width.

The width of the ceiling and the total width of the oval come out as a result. This type of parametrization allows to easily meet the cabin requirements: for instance the variable H_2 represents the height of the cabin and can be modified according to new specifications during the design phase.

Cabin Layout

An initial trade off has been carried out to select the cabin layout, in particular the relative arrangement of cabin and cargo hold. Even though Benad [8] proposed a configuration in parallel (cargo hold behind the passenger cabin, see Figure 2.5(a)), the wide oval cabin is more suitable for a series arrangement with the cargo hold placed outboard. The latter seems more promising since it uses the available volume more efficiently. Also the load factor perceived by the passengers is reduced because the last row is moved inboard. Hence, assuming a cabin width of 6 m, 10 people fit in a single row in a twin-aisle configuration, considering seat and aisle width of the reference aircraft (see Section 1.4.1). A section of the cabin is shown in Figure 2.10. The value of 6 m is fixed for cross sections 3 and 4. In addition, the cabin height (H_2) of sections 2,3 and 4 is set to 2.1 m, according to the top level requirements reported in Section 1.4.1. The upper and lower heights of the cross sections, which define the radii of the respective arcs, are free and they strongly affect structural and aerodynamic performances. Since a multi-disciplinary optimization is not included in this work, these design variables are varied during the initial design exploration and then held fixed during the aerodynamic optimization. It is also important to specify that a small cargo compartment in the front might be required to prevent the Flying V tip over when loading the aircraft, similarly to the Fokker 50: a small weight is enough to balance the airplane due to the big distance from the centre of gravity.

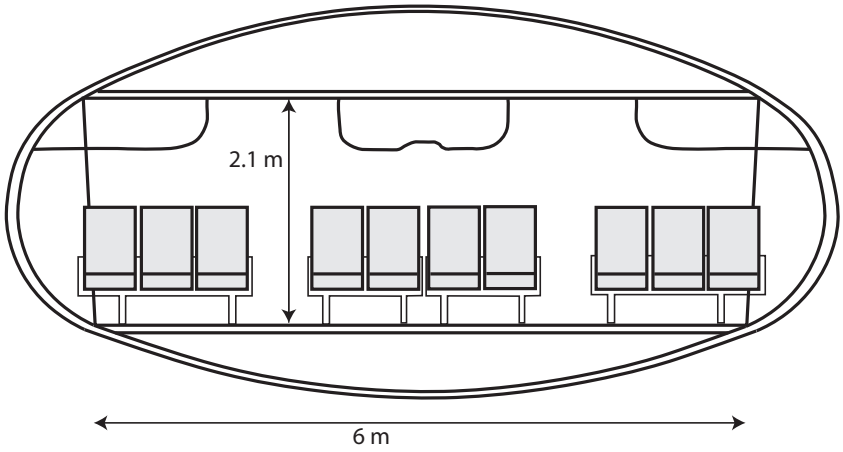

Figure 2.10: Flying V cabin cross section (from section 3 to 4)

Oval cross section	Variable (unit)	Value	Explanation
1	H_1 (m)	dependent	Based on nose cone parametrization (a_{up}, e_{up})
	H_2 (m)	1.2	Minimum height where cockpit starts
	H_3 (m)	dependent	Based on nose cone parametrization (a_{low}, e_{low})
	W_F (m)	dependent	Determined by H1, H2, H3 and total oval width
2	H_2 (m)	2.1	Top level requirements
	W_F (m)	dependent	Determined by H1, H2, H3 and total oval width
3	H_2 (m)	2.1	Top level requirements
	W_F (m)	6	Design choice to have 10 people twin-aisle rows
4	H_2 (m)	2.1	Top level requirements
	W_F (m)	6	Design choice to have 10 people twin-aisle rows

Table 2.3: Oval cross sections parameters: fixed values

The complete set of the fixed oval section parameters is reported in Table 2.3. It is important to remark that H_1 and H_3 of section 1 are determined according to the nose cone parametrization, described in Section 2.4.3. Moreover, W_{F} of sections 1 and 2 is not a design variable: this is computed based on H_1, H_2, H_3 and the total oval width, which is determined by the planform variables. Not less importantly, section 5 is within the outer shape, hence it is not determined by aerodynamic considerations, yet volume and structural ones: it does not impact on the outer mold line of the Flying V. Hence, 6 oval sections parameters are free to vary: H_1 and H_3 of sections 2,3 and 4 (Figure 2.7).

2.4.3. Nose Cone Parametrization

To increase the flexibility and tailoring of the nose cone, four additional variables are defined. In particular, two additional oval cross sections between sections 1 and 2, named 1a and 1b (see Figure 2.7), are added and their heights are defined by two interpolating polynomials at the center line (one for the upper and one for the lower part) of the type:

$$z(x) = a\sqrt{x} + dx^2 + ex^3 + b \tag{2.12}$$

In which the parabolic term $a\sqrt{x}$ is included to guarantee the tangency of the two curves at the leading edge, similarly to the equation of a 4-digit NACA airfoil. Then, each curve is imposed to pass through two points,

namely the most forward point of the aircraft and the upper (and lower) point of sections 2 (Figure 2.7). Therefore, two degrees of freedom allow to tailor each curve. Figure 2.11 shows the center line profile (root profile), in which the front part is defined by two polynomials of Equation (2.12): it is noticeable that changing the coefficients a and e of the suction side (a_{up} and e_{up}) leads to modifications in the shape of the cone. The same holds for the pressure side. All the curves intersect in two points: the one on the right is where the front cone finishes and rear airfoil part starts. The rear fairing construction is described in Section 2.4.4. Notice that the automatic adjustment of the rear shape of Figure 2.11 is due to the imposed tangency and curvature continuity, while keeping the other parameters fixed.

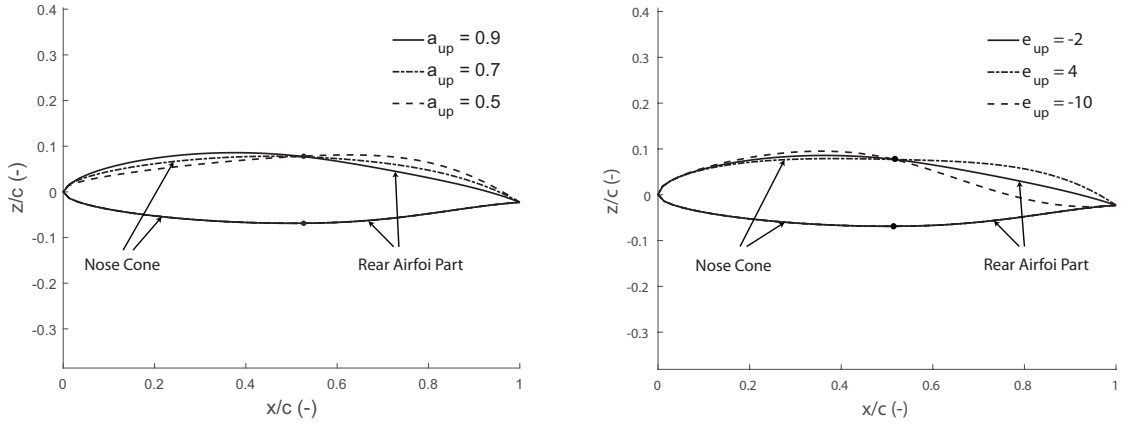

Figure 2.11: Front cone parametrization: representation of the root profile at varying coefficients a_{up} and e_{up} with fixed rear airfoil parameters

Hence, for each combination of coefficients a_{up} and e_{up} (the same holds for a_{low} and e_{low}), the polynomial is fully defined, and the total height is calculated at the different locations of sections 1, 1a and 1b. For instance:

$$z(x_1) = z_{1_{\text{tot}}} = \frac{H_{2_1}}{2} + H_{1_1} \tag{2.13}$$

H_{1_1} can be calculated by inverting Equation (2.13). The same holds for sections 1a and 1b.

2.4.4. Rear Airfoil Part Parametrization

Once the cabin shape is defined, a rear airfoil part (or fairing) is attached to the front part at three spanwise positions (profiles I, II and III of Figure 2.6). Then, the complete profiles are lofted to create the wing shape. The upper and lower curves of the rear profile are defined by 4^{th} order polynomials of type:

$$z(x) = ax^4 + bx^3 + cx^2 + dx + e \tag{2.14}$$

Then, three conditions are imposed for each curve, namely: passing through the last point of the front part, tangency and curvature continuity. As proved by Korakianitis [46] using Navier-Stokes equations, the flow characteristics (velocity and pressure distributions) have an evident dependence on airfoil curvature: hence, curvature continuity is important to ensure a good aerodynamic behaviour. Moreover, the suction and pressure sides intersect at the same trailing edge point. Hence, the total degrees of freedom for upper and lower curves are three: c_{up}, c_{low} and the vertical position of the trailing edge z_{TE}. Hence, the rear fairings of profiles I, II and III are defined by 9 variables. Figure 2.12 shows the behaviour of the root rear airfoil at varying coefficients c_{low}; the same holds for the suction side.

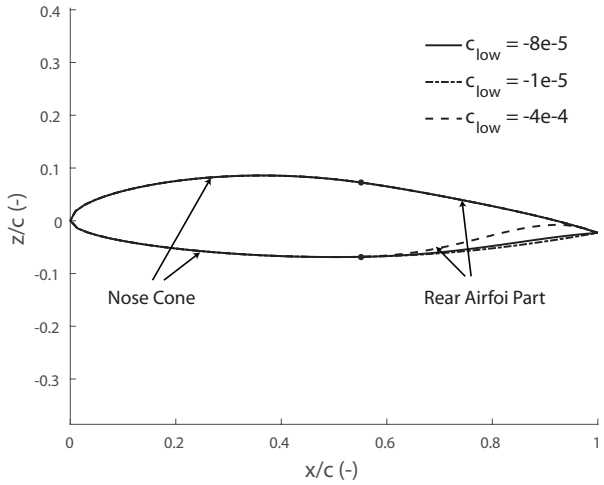

Figure 2.12: Rear airfoil part at $y/c = 0$ at varying coefficients a_{low}

2.4.5. Airfoil Variables

An airfoil can be represented by a cloud of points and this would allow precise local modifications. However, it is not efficient to use coordinate based methods within an optimization process, due to the huge amount of variables involved [47]. Moreover, if the coordinates of the nodes are free to move around the space, there is a big tendency to generate unrealistic and unfeasible designs: hence, additional time would be required to converge to a practicable shape [48]. This is the reason why many researchers have been implementing different methods to describe the airfoil in an efficient way, namely involving a limited number of parameters and maintaining a certain accuracy.

According to Straathof et al. [49], curves represent a way to define the airfoil with a reduced amount of variables. For instance, Bezier curves and B-splines make use of this principle. Then, the so called CST method, which was developed by Kulfan [50] at Boeing Commercial Airplane Group, can also be suitable for this purpose. Here below, a brief description of the different approaches is presented, with their advantages and drawbacks.

A Bezier curve can be expressed as:

$$\mathbf{p}(u) = \sum_{i=o}^{n} \mathbf{p}_i B_{i,n}(u) \tag{2.15}$$

Where $\mathbf{p}_i$ is the i^{th} control point and $n+1$ the number of control points: this means that the order of the polynomial is n. The term $B_{i,n}(u)$ can be written as:

$$B_{i,n}(u) = \binom{n}{i} u^i (1-u)^{n-i} \tag{2.16}$$

In a Bezier curve, an increase of the number of control points leads to a higher order polynomial, which is not always desired. B-splines are really similar to Bezier curves but, instead, they depend on a separate parameter k. In particular, adding more vertices does not entail a higher degree of the polynomial, since k is the degree. This can be useful since it allows an increase of control points locally to get a higher accuracy. Azamatov et al. [51] proposes also a weighted version of the B-splines, the so called NURBS (Non-Uniform Rational B-Splines).

The CST method [50] is a parametrization characterised by two functions: the class function defines the general shape, namely the presence of certain geometrical features and the shape function modifies the shape without changing its properties. The method can be defined as:

$$\xi(\psi) = C_{\mathrm{N1}}^{\mathrm{N2}}(\psi) S(\psi) \tag{2.17}$$

In which C and S are class and shape functions respectively. Furthermore, the values of N1 and N2 define the class: a round-nose airfoil is described by N1=0.5 and N2=1, thus:

$$C(\psi) = \sqrt{\psi}(1-\psi) \tag{2.18}$$

The shape functions can be expressed in the form of Bernstein polynomials, B-splines or a combination of the two in the so called Class-Shape-Refinement-Transformation method (CSRT) proposed by Straathof [52]. As stated by Straathof et al. [49], the use of Bernstein polynomials is beneficial since every reasonable set of coefficients leads to feasible and realistic airfoils; nevertheless, local modifications of the airfoil are not possible and an increase in control points leads to a higher order polynomial. These drawbacks are overcome by the use of B-splines, which allow a much more accurate local control. The combination of the two is claimed by Straathof [52] to be suitable to a stepwise approach: firstly, the Bernstein coefficients of the shape function are modified, then the B-spline coefficients of the refinement function are varied to adjust the shape locally.

For the purpose of this project, the CST method with Bernstein polynomials as shape functions is deemed to be the most suitable to represent the airfoils of profiles IV and V of Figure 2.6. First of all, the improved flexibility of CSRT also entails higher complexity, which is not desired at this stage. Then, according to Selvan [47], a parametrization of a complete airfoil is deemed to be satisfactory if the error is lower than $5 \cdot 10^{-4}$: the CST method proposed requires 8 parameters, whereas a Bezier curve needs 24 variables. To achieve higher accuracy, 12 CST parameters are used for profiles IV ad V (see Figure 2.6), 6 for the suction and 6 for the pressure side. Hence, the total number of design parameters is 56: they are grouped in different vectors, as reported in Table 2.4.

Vector	Variables	Number
$\bar{y}_{\mathrm{planf}}$	S, b, c_{r}, Λ_1, Λ_2, λ, k_1, k_2, ϵ_{IV}, ϵ_{V}	10
$\bar{y}_{\mathrm{oval}}$	H_{1_2}, H_{3_2}, H_{1_3}, H_{3_3}, H_{1_4}, H_{3_4}	6
$\bar{y}_{\mathrm{nose}}$	a_{up}, e_{up}, a_{low}, e_{low}	4
$\bar{y}_{\mathrm{rear}}$	$c_{\mathrm{up_I}}$, $c_{\mathrm{low_I}}$, $z_{\mathrm{TE_I}}$, $c_{\mathrm{up_{II}}}$, $c_{\mathrm{low_{II}}}$, $z_{\mathrm{TE_{II}}}$, $c_{\mathrm{up_{III}}}$, $c_{\mathrm{low_{III}}}$, $z_{\mathrm{TE_{III}}}$	9
$\bar{y}_{\mathrm{CST}}$	$CST_{\mathrm{i_{IV}}}$ for i = 1,2,...,12, $CST_{\mathrm{i_V}}$ for i = 1,2,...,12	24
$\bar{y}_{\mathrm{fin}}$	A_{fin}, λ_{fin}, Λ_{fin}	3

Table 2.4: Design variables grouped in design vectors

2.5. Aerodynamic Analysis Module

The aerodynamic analysis module features three sub-modules as shown in Figure 2.13. The chosen analysis method is outlined in Section 2.5.1, and the unstructured grid generation is explained in Section 2.5.2.

2.5.1. Analysis Method

The main purpose of the aerodynamic analysis method is to obtain an accurate estimation of the aerodynamic coefficients at the cruise condition, far from separation and stall, and drive aerodynamic shape optimization analyses. Therefore, the Euler model is selected due to its capability of accurately estimating wave drag (Section 1.3), which represents a relevant component of the overall drag in transonic regime. Lack of

knowledge in designing such an unconventional configuration has been another driver of this choice: there are no references about shock waves strength for the Flying V configuration, therefore the outcome of potential flow equations could be misleading. In addition, it has a relatively low computational cost compared to RANS equations. The Stanford University Unstructured code (SU2) is selected: it is an open-source package of C++ software tools designed with Computational Fluid Dynamics (CFD) and aerodynamic shape optimization in mind [53].

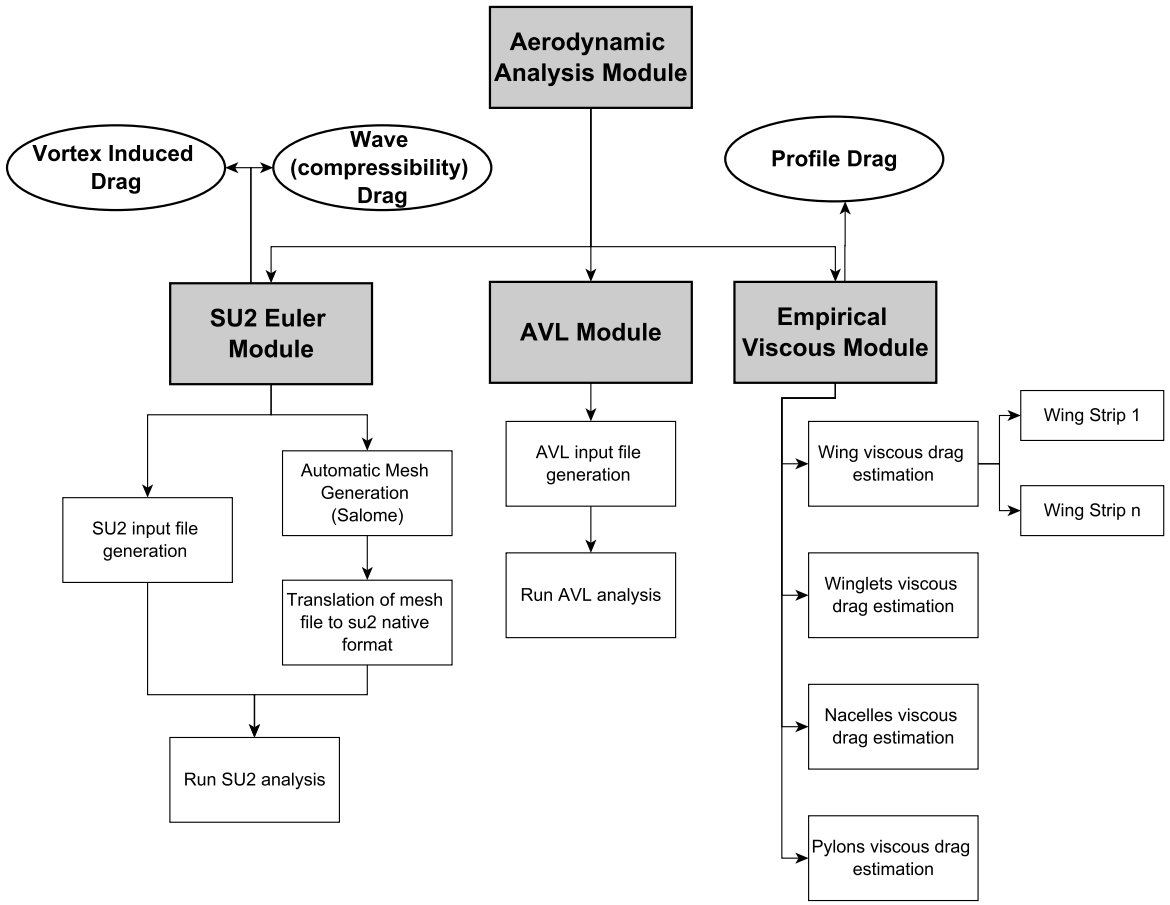

Figure 2.13: Aerodynamic analysis module

The SU2 module, implemented in ParaPy, generates the configuration file for the solver, which contains a set of user's options, such as flight conditions, reference system, numerical solver and convergence criteria. In addition, it produces the unstructured mesh by involving the Salome package in ParaPy. Subsequently, it translates the grid file into the native format required by the SU2 suite. Then, it runs the program, extracts the aerodynamic coefficients, and plots pressure coefficient distributions at different spanwise locations. Nacelles, pylons and fins are not included in the SU2 simulations.

Since the Euler flow model neglects viscosity, it is able to estimate only vortex induced drag and wave drag. These contributions are grouped in $C_{D_{\text{inv}}}$, because they originate from inviscid phenomena. Hence, a separate viscous module is created to compute the Flying V profile drag (Figure 2.13). In particular, the profile drag is made up by three contributions: skin friction, pressure, and lift-related profile drag. As explained by Gur et al. [29], the third contribution can be neglected since the analysis focuses uniquely on cruise condition: this assumption is further verified in Section 3.3. The remaining two components are addressed simultaneously

with the following formulation:

$$C_{D0} = C_F \cdot FF \cdot \frac{S_{\text{wet}}}{S} \tag{2.19}$$

Where C_F is the flat plate skin friction coefficient, FF is the form factor of each component, which accounts for pressure drag due to viscous separation and it is valid until drag divergence [40], S and S_{wet} indicate reference area and wetted area respectively. The Flying V is separated into components like wing, winglets, nacelles and pylons and Eq. 2.19 is applied to each of them. While the wing is divided into strips, which are then treated separately (each component has its own wetted area), each body (nacelles in case of the Flying V) is considered as a single component. For each part of the aircraft, while S_{wet} and S are defined by the geometry, the form factor and flat plate skin friction coefficient can be computed by semi-empirical equations. The skin friction coefficient for turbulent flow, which applies to the case of the Flying V aircraft since it flies at high Mach and Reynolds numbers, is expressed by Raymer [40] as:

$$C_F = \frac{0.455}{(\log_{10} Re)^{2.58}(1 + 0.144M^2)^{0.65}} \tag{2.20}$$

In which Re and M are Reynolds and Mach number respectively. However, if the surface has a relatively high roughness, the friction coefficient is higher than the one calculated by Equation 2.20; this effect can be taken into account by comparing the actual Re to the so called "cut-off Reynolds number" (see Raymer [40]). The lower of the two is then plugged in Equation 2.20. In terms of form factor, open literature outlines various models: for this purpose, the Torenbeek one [7] is chosen for the wing strips since its agreement with experimental results is satisfactory (see Section 3.3). It can be expressed as:

$$FF = 1 + \left(2.7 \cdot \frac{t}{c} + 100 \cdot \left(\frac{t}{c}\right)^4\right) \cos^2(\Lambda_{0.5}) \tag{2.21}$$

In which, $\frac{t}{c}$ is the thickness to chord ratio of each strip and $\Lambda_{0.5}$ is the mid chord sweep angle. Equation 2.21 is also used to estimate pylons drag contribution. Then, the form factor used for the nacelles is given by Raymer [40]:

$$FF = 1 + 0.35 \cdot \frac{d}{l} \tag{2.22}$$

In which d and l are nacelles diameter and length respectively. The higher the nacelle aspect ratio ($\frac{l}{d}$), the lower the pressure drag. The total profile drag is computed by adding the different contributions, as follows:

$$C_{D0} = C_{D0_{\text{wing}}} + C_{D0_{\text{fins}}} + C_{D0_{\text{pylons}}} + C_{D0_{\text{nacelles}}} \tag{2.23}$$

The lift to drag ratio is estimated by adding the profile drag to the wing inviscid drag resulting from SU2:

$$\frac{C_L}{C_D} = \frac{C_L}{C_{D0} + C_{D_{\text{inv}}}} \tag{2.24}$$

Finally, the AVL module is created to efficiently explore the design space during the multi-fidelity design space exploration (see Section 2.3) and produce aerodynamic loads for the structural analysis module. This sub-module generates the AVL required input file, runs the program and produces the lift and moment distributions at a low computational cost.

2.5.2. Unstructured Grid Generation

When solving numerical simulations, the grid plays a relevant role since its quality directly affects the accuracy of the results. Generally speaking, two different grid topologies can be distinguished: structured and unstructured. The former discretization shows a certain "regularity" (internal cells are topologically similar) and usually relies on regular arrays of quadrilateral or hexahedral cells in 2D and 3D respectively. On the other hand, there is no general connectivity rule in unstructured grids and the cells can have arbitrary shapes (usually they are triangles in 2D and tetrahedra in 3D) [54]. This alternative provides a great flexibility for meshing

complex domains; at the same time, it allows easy implementation of adapting meshing techniques, according to which the cells are modified locally to enhance the accuracy of the results. SU2 uses unstructured grids. Moreover, there is no need to discretize the boundary layer with hexahedral cells since the Euler flow model is implemented. Furthermore, SU2 incorporates multi grid techniques to increase convergence speed: once the user provides the input mesh, the code generates coarser meshes to speed up the calculations [53]. This technique is used for the purpose of this project.

The tetrahedral unstructured grid is generated by the Salome meshing tool embedded in ParaPy, starting from the 3D geometry. An example of a coarse grid is shown in Figure 2.14 on the right hand side. The generation follows the so called bottom-up flow: nodes on vertices are created first, subsequently edges are split into segments, and the surface and volume cells are created. This automatically guarantees the conformity of the mesh. The computational domain used for the numerical analyses is a large parallelepiped and the far-field boundary is located around 20 body lengths away from the airplane. As stated by Chan et al. [55], in a 3D transonic flow problem, the sensitivity to far field distance is less severe than the correspondent 2D case, where a 40 body lengths distance is required. In order to confirm this assumption, a sensitivity test is performed and the changes in terms of forces and moments are considered negligible. The dimensions of the computational domain used for the analyses are shown in Figure 2.14 on the left hand side. The mean aerodynamic chord, which is about 18 m, is considered the Flying V reference length: therefore, a length of the domain equal to 400 m proves to be sufficient. Moreover, meshed surfaces are assembled in groups in order to assign boundary conditions (see Figure 2.14), namely:

- **Euler boundary condition**, which prevents flow penetration inside the wing surface.
- **Far-field condition**, namely free stream values applied to the faces of the computational domain.
- **Symmetry condition** specified on the plane to which the semi wing is attached. This allows to analyse half wing, hence save computational time. This condition is not applied when analysing the full model in sideslip conditions.

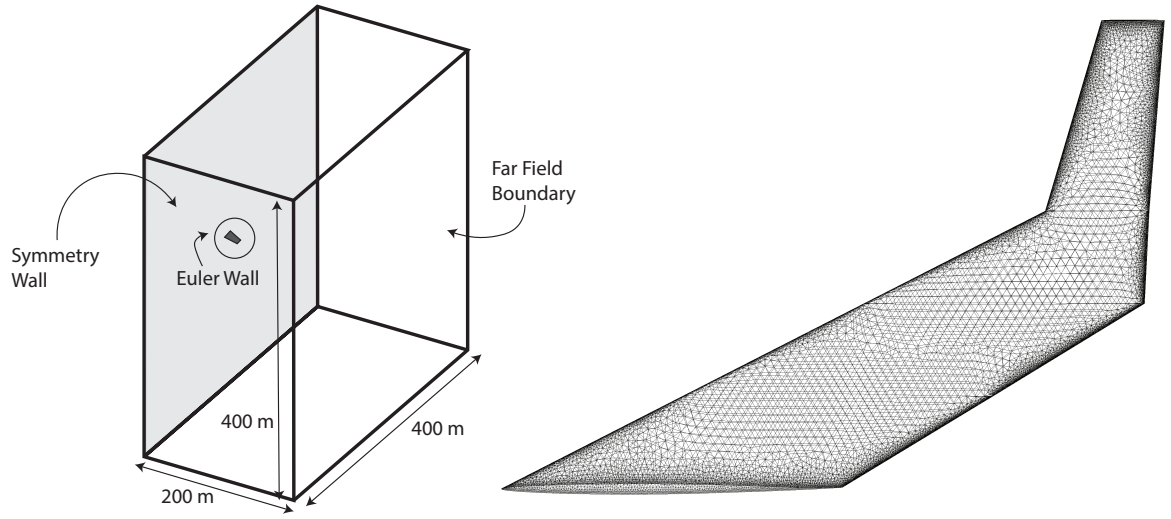

Figure 2.14: Grid computational domain with dimensions and boundaries (left) and example of coarse grid generated by ParaPy (right)

2.6. Additional Modules

Although the main objective of the research project is the aerodynamic design, it is important to have a look at the big picture, the overall Flying V design. In particular, the structural sizing and weight estimation module is being built. Moreover, the simplified performance analysis and the payload capacity module are outlined in Sections 2.6.1 and 2.6.2.

2.6.1. Performance Analysis

The performance analysis module is implemented to estimate the fuel weight required to complete the flight mission. The method is presented by Roskam [56] and is called *Fuel Fraction Method*: the fuel weight required for cruise is evaluated using the Breguet range equation, whereas the other segments contributions are calculated with statistical factors. Each fuel fraction value represents the ratio between the aircraft weight at the end and at the beginning of the segment: hence, the overall fuel weight ratio M_{ff} is the product of the single contributions. The Breguet equation can be expressed as:

$$R = \frac{V}{c_T} \cdot \frac{L}{D} \cdot \ln\left(\frac{W_{5_{\text{start}}}}{W_{5_{\text{end}}}}\right) \tag{2.25}$$

Where V is the cruise speed, $\frac{L}{D}$ the lift to drag ratio, c_T the specific fuel consumption and $\left(\frac{W_{5_{\text{start}}}}{W_{5_{\text{end}}}}\right)$ the fuel fraction during cruise. The fuel fractions for the other segments are reported in Table 2.5 [56]. Thus, the fuel weight is calculated as:

$$W_{\text{fuel}} = 1.05 \cdot (1 - M_{\text{ff}}) W_{\text{to}} \tag{2.26}$$

In which, M_{ff} is the overall fuel weight fraction, W_{fuel} and W_{to} are the fuel and take off weight respectively; the coefficient 1.05 accounts for a 5% reserve fuel.

Segment	Fuel weight fraction
Start and warm-up (1)	0.990
Taxi (2)	0.990
Take-off (3)	0.995
Climb (4)	0.980
Cruise (5)	Breguet Formula (see Equation (2.25))
Descent (6)	0.990
Landing, taxi and shut-down (7)	0.992

Table 2.5: Fuel fractions for a typical flight mission, reported by Roskam [56]

2.6.2. Payload Capacity

The payload capacity module is intended to provide a preliminary estimation of the amount of passengers that can be accommodated in the Flying V. The objective is to reach the maximum capacity (in a single class layout) of the reference aircraft, namely 440 passengers as reported in Section 1.4.1; the required total freight volume is 172.4 m^3 [2]. This implies an area of around 82 m^2, being the cargo stored in a volume of 2.1 m height. The required lavatories and galleys areas are calculated with statistical correlations suggested by Raymer [40]. Raymer recommends 40-60 passengers per lavatory (40" $\cdot$ 40", around 1 m^2) for the economy configuration: hence, considering 44 passengers per lavatory means 10 toilets, which require 10 m^2 in total. Furthermore, according to the empirical factors, a galley volume of 1-2 ft^3 per passenger is required: therefore, an area of

[2] Dimensions & key data | airbus, a leading aircraft manufacturer. Retrieved in March 12, 2016 from http://www.airbus.com/aircraftfamilies/passengeraircraft/a350xwbfamily/a350-900/specifications/

around 10 m^2 must be addressed to galleys, considering a cabin height of 2.1 m. The cockpit of a transport aircraft with 4 crew members typically has an overall length of 150 in, as suggested by Torenbeek [7]; considering an average width of 4 m of the reference airplane cockpit, the required floor area for the cockpit is around 15 m^2. The total floor area addressed to payload is extracted from the geometry model implemented in ParaPy; by subtracting the above mentioned areas to the total one, the floor area available (A_{avail}) to accommodate passengers can be computed. The passenger capacity is subsequently calculated as:

$$n_{\text{pax}} = A_{\text{avail}} \cdot D_{\text{pax}} \tag{2.27}$$

In which D_{pax} indicates the number of passenger per square meter. This value is based on a twin aisle cabin with 10 passengers per row, 6 meters width and 0.8128 m seat pitch (see Section 1.4.1). This leads to a passenger density of 2.053 passengers per square meter. This procedure is based on the maximum capacity layout and could be extended to multi classes configurations by changing lavatories and galleys area and passenger density. All the values used are summarised in Table 2.6.

Parameter (unit)	Value	Notes-Source
Lavatories area (m^2)	10	Raymer [40]
Galleys area (m^2)	10	Raymer [40]
Cockpit area (m^2)	15	Torenbeek [7]
Freight area (m^2)	82	Airbus, Dimensions & key data[3]
Total area (m^2)	Variable	Calculated from geometry model
Passenger density (pax/m^2)	2.053	Benad [8]

Table 2.6: Values used in the payload capacity module

This module aims to provide an initial estimation of the passenger capacity, given the geometry and simple statistical correlations. It could be used to investigate the effect of the increase in aircraft size and the possible development of the Flying V family. In addition, the estimation of the maximum amount of passengers is employed as a constraint in the optimization procedures in order to make sure that the final configuration has the same (or higher) payload capacity of the reference aircraft (see Table 4.2).

3

Validation and Verification

This chapter can be divided into two main parts. The first deals with the unstructured grid convergence study and quality assessment, whereas the second focuses on the validation and verification of the aerodynamic assessment method, presented in Section 2.5.1.

3.1. Grid Convergence Study

A grid convergence analysis is performed in order to determine the coarsest mesh which guarantees acceptable results. In particular, for aerodynamic shape optimization, in which the computational time plays a relevant role, it is more important that the aerodynamic phenomena are accurately captured rather than the exact coefficients are estimated. Therefore, the selected mesh for aerodynamic shape optimization is relatively coarse.

Regions characterised by higher curvature, like the wing leading edge, and the trailing edge require higher refinement. Moreover, it is good practice to estimate the element size of the surface grid based on the local chord. In particular, according to Chan et al. [55], a typical size of 0.1% of the local chord close to leading edge is fine enough to accurately resolve the flow physics. Also the refinement of regions far from leading edge and trailing edge is progressively increased in order to enhance the accuracy close to the shock waves. In particular, some parameters are selected in order to control the element size of surface and volume grid:

1. Maximum size of 2D elements (triangles) on the wing surface.
2. Maximum size of 2D elements (triangles) on the far-field boundary.
3. Maximum size of 3D elements (tetrahedra).
4. Growth ratio of 2D elements on the wing and far-field boundary.
5. Growth ratio of 3D elements.
6. Number of points to length ratio on the wing leading edge and trailing edge. This is implemented to have more control on high curvature edges.

The refinement is progressively increased by decreasing maximum size and growth ratio of 2D and 3D elements and increasing the number of points on leading edge and trailing edge. The results of the convergence test are shown in Figure 3.1. The error is relative to the value of the finest tested grid: for instance, the

inviscid drag coefficient error is computed as:

$$\text{Error} = \frac{C_{D_{\text{inv}}} - C_{D_{\text{inv}}}^{\text{fine}}}{C_{D_{\text{inv}}}^{\text{fine}}} \cdot 100 \tag{3.1}$$

The test is applied to the Flying V improved baseline configuration for a fixed lift coefficient (C_L = 0.26) and Mach number equal to 0.85.

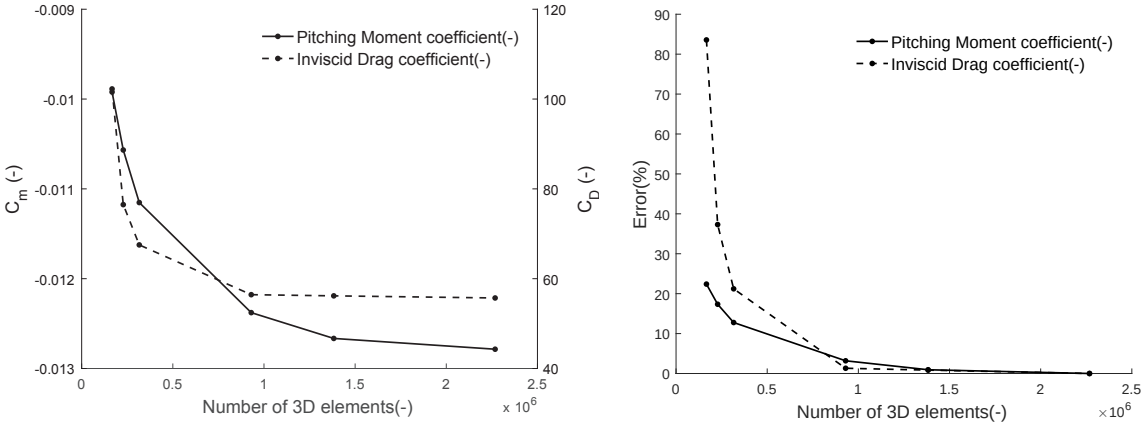

Figure 3.1: SU2 grid convergence in terms of aerodynamic coefficients (M = 0.85, C_L = 0.26)

As depicted in Figure 3.1, the results obtained with around 1 million cells are accurate enough for the shape optimization purpose, because the drag and pitching moment coefficients are within the 1% and 3% error respectively. This grid is obtained with the parameters specified in Table 3.1.

Grid parameter	Value
Max size 2D elements wing (m^2)	0.2
Max size 2D elements far field (m^2)	15
Max size 3D elements (m^3)	15
Growth ratio 2D elements (−)	0.15
Growth ratio 2D elements (−)	0.3
Point to length ratio LE and TE (−)	30

Table 3.1: Grid parameters selected for shape optimization analyses

The parameters reported in Table 3.1 are used to automatically generate the volume mesh once the outer mold line of the Flying V is produced by the MMG.

3.2. Grid Quality Assessment

Due to the relevant impact of the grid on the accuracy of the results, some criteria are commonly used to assess the quality of the mesh. According to Woodard et al. [57], different types of quality measures can be distinguished: those which apply to individual elements only and those which account for the interaction with the surrounding elements. In particular, in case of a three dimensional grid, the dihedral angle and aspect ratio are relevant parameters belonging to the former type, while the equiangle skewness to the latter. Dihedral angle and aspect ratio are measures of the shape of the tetrahedron, which is really important for the numerical method. The former should not be close to 0° and 180°: good practice is to constrain it with lower and upper limits of 10° and 170° respectively. The aspect ratio is calculated as the ratio between the

volume of the element and the radius of the circumscribed sphere to the third power, then normalized with the equilateral tetrahedron. It can be expressed as:

$$\text{Aspect Ratio} = \frac{(V/r^3)_{\text{actual}}}{(V/r^3)_{\text{ideal}}} \tag{3.2}$$

This means that the value should be as close as possible to 1. The equiangular skewness, on the other hand, is a measure of the distortion of surrounding cells: this parameter should not exceed 0.9 in case of tetrahedrons. Notice that in ICEM CFD the value is the complementary $1-x$, hence it is desired to be higher than 0.1.

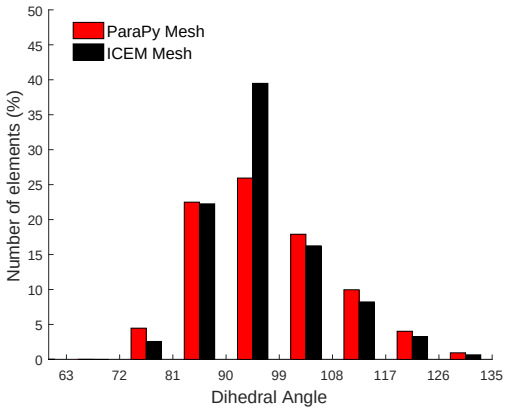

(a) Dihedral angle

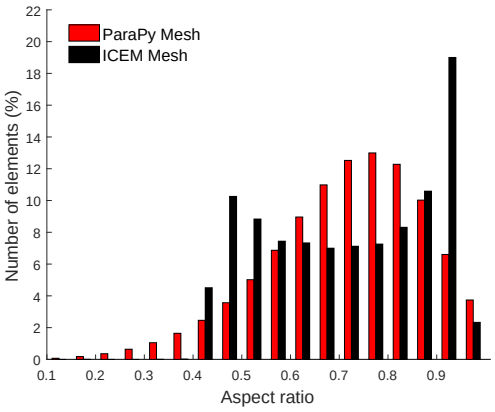

(b) Aspect ratio

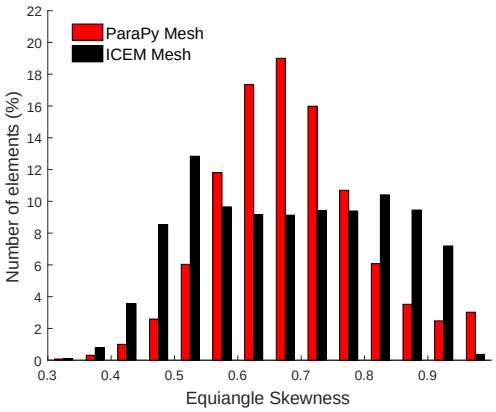

(c) Equiangle skewness

Figure 3.2: Quality comparison between ParaPy and ICEM grids applied to the baseline configuration

In order to estimate the quality of the grid automatically generated in ParaPy, the Flying V baseline configuration is meshed in ICEM CFD, which has multiple options to locally change refinement and incorporates advanced smoothing algorithms. The two grids have comparable size and refinement. Subsequently, the two grids are compared within ICEM CFD based on the above mentioned criteria: dihedral angle, aspect ratio and equiangle skewness. The results of the comparison are presented in Figures 3.2(a) to 3.2(c). The dihedral angle (see Figure 3.2(a)) of both the grids satisfies the upper and lower bounds of 170° and 10°. In terms of aspect ratio (see Figure 3.2(b)), the ICEM grid has 20% of elements with values higher than 0.9 and the others spread in a uniform way from 0.4 to 0.9; there are really few elements with low aspect ratio. On the other hand, the aspect ratio of the ParaPy grid shows a distribution similar to a Gaussian one: the majority of the elements is between 0.6 and 0.9, but there are some elements with values lower than 0.4. In a nutshell, even though

the mean value (0.717 for the ICEM mesh and 0.714 for the ParaPy one) is almost the same, the ICEM grid has a higher quality in terms of aspect ratio due to less elements with low values. Similar trends are depicted in Figure 3.2(c), in case of the equiangle skewness. However, elements with really low values are not present in both the grids. The mean value is 0.679 and 0.687 for the ICEM and ParaPy grids respectively, hence the latter performs slightly better according to this quality measure. To conclude, the quality of the ParaPy mesh, generated automatically for any input geometry with few inputs, is satisfactory since it is comparable to a mesh produced by a more sophisticated program.

3.3. Aerodynamic Solver Validation and Verification

The aerodynamic analysis method described in Section 2.5.1 is validated with the experimental results of the Onera M6 wing and verified with higher order codes. Furthermore, verification is obtained by testing the solver on the NASA CRM and comparing the results with open literature.

3.3.1. Onera M6 Wing

The Onera M6 wing represents a standard validation case for external flow fields due to its simple geometry and complexities of transonic flow, including shock waves and turbulent boundary layer separation. The Onera M6 wing is shown in Figure 3.3. It is a 30 degrees swept, semi-span untwisted wing. It uses a symmetric airfoil using the ONERA D section. The simulation performed to validate the aerodynamic solver uses the flow conditions of Test 2308 reported by Schmitt et Charpin [58]: Mach number equal to 0.8395, angle of attack of 3.06° and zero sideslip. This condition corresponds to a Reynolds number of $11.72 \cdot 10^6$ based on the mean aerodynamic chord of 0.64607 m.

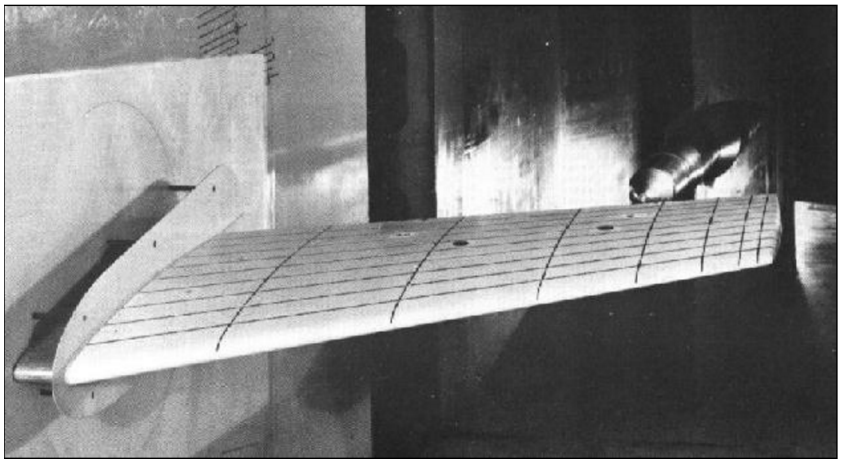

Figure 3.3: Onera M6 wing [58]

The computational domain of the SU2 Euler implementation is a large parallelepiped. The mesh is characterised by 140,244 tetrahedral elements and three boundary conditions are applied: Euler wall on the wing (no-penetration proper of inviscid flows), far field characteristics based on free stream conditions and symmetry boundary condition on the wall where the half-span wing is attached. Different numerical methods to solve the convective flow equations are tested: the Jameson-Schmidt-Turkel (JST) scheme proves to be really stable and reaches convergence faster, while the Roe solver is more accurate with the same mesh refinement. The pressure distributions resulting from the numerical analysis are compared to the experimental data [58]. Six different spanwise locations are analysed and the comparison is shown in Figures 3.4 to 3.9. The overall agreement is satisfactory since the trends are captured well by the Euler analysis. The strong shock wave in the outer part is accurately predicted; however, as pointed out by Mayeur et al. [59], the meeting of the

two shock waves is predicted at a different spanwise section (see Figure 3.7). This may be caused by the fact that the ideal symmetry condition proper of the computational approach does not exactly simulate the experimental flow field induced by the half wing flow diverter placed in the wind tunnel. Furthermore, it is noticeable that JST (solid line) is slightly less accurate then Roe (dotted line): this means that JST probably requires a finer mesh to obtain the same accuracy.

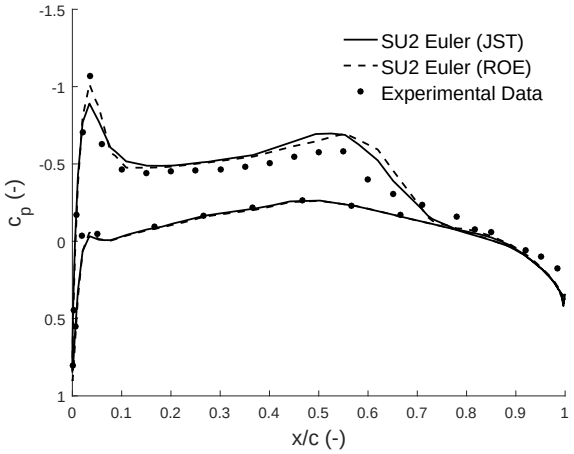

Figure 3.4: Onera M6 wing: c_p distribution (x/c=0.2)

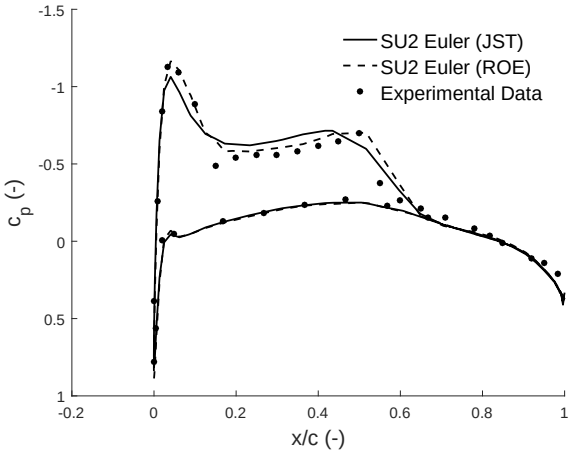

Figure 3.5: Onera M6 wing: c_p distribution (x/c=0.44)

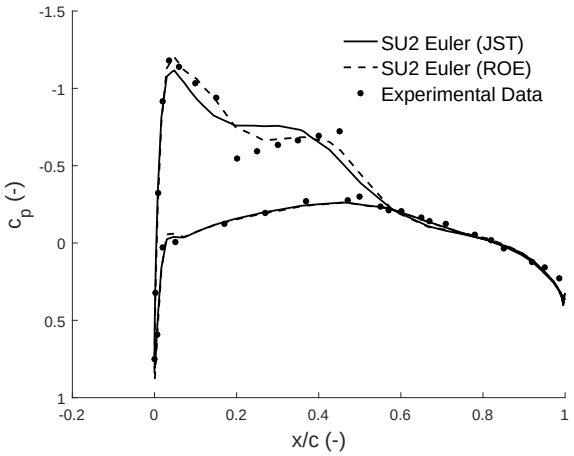

Figure 3.6: Onera M6 wing: c_p distribution (x/c=0.65)

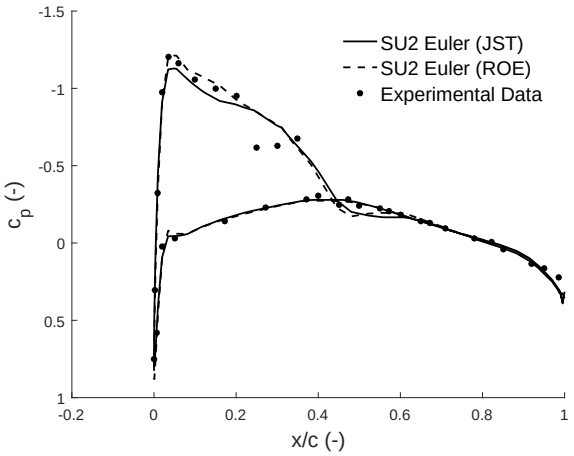

Figure 3.7: Onera M6 wing: c_p distribution (x/c=0.80)

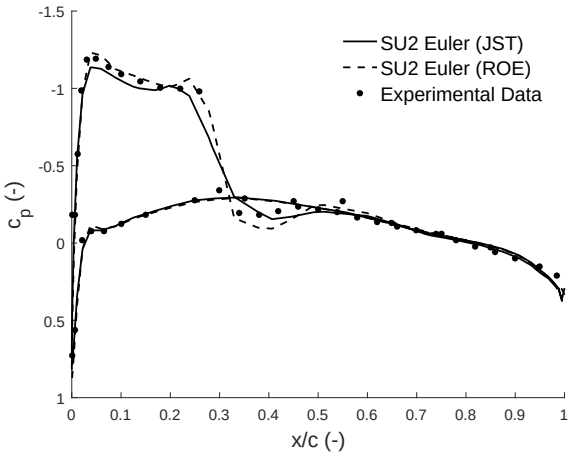

Figure 3.8: Onera M6 wing: c_p distribution (x/c=0.9)

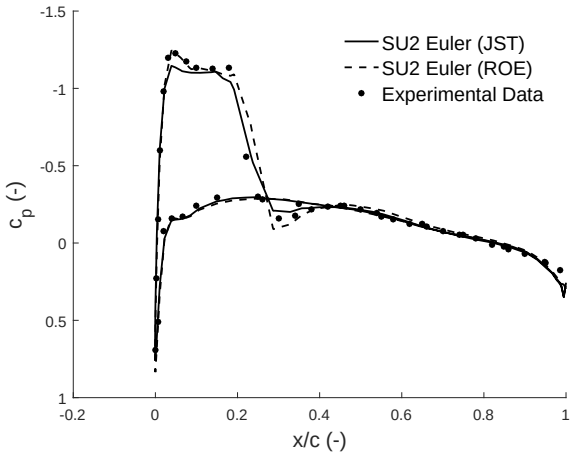

Figure 3.9: Onera M6 wing: c_p distribution (x/c=0.95)

Beside the validation of the tool in terms of pressure distributions, it is important to compare the aerodynamic coefficients, which drive the aerodynamic design and shape optimization. Since the experimental data does not include coefficients, the results obtained from SU2 Euler are compared to other studies involving RANS, Delayed Detached Eddy Simulation (DDES) and Detached Eddy Simulation (DES), as previously done by Durrani and Qin [60]. This represents the verification process. Furthermore, RANS simulations are performed with SU2 in order to compare the Euler results at different angle of attacks with a higher order code. The drag coefficient resulting from the Euler analysis does not account for viscous effects, therefore the profile drag coefficient is added to it (see Section 2.5.1). The form factor outlined by Torenbeek is used since it compares well with the RANS (SU2) calculations and previous studies. The drag polar is shown in Figure 3.10. The results obtained with the JST method show a really good agreement with the RANS SU2 outcome; moreover, the curve fits perfectly between the points generated by other investigations with RANS, DES and DDES, represented with star markers. The Roe scheme results have a small offset at low lift coefficients and then they converge to the JST ones. Besides, the assumption of neglecting the additional 2D profile drag at low lift coefficients (Section 2.5.1) is further confirmed by this verification. Certainly, when separation starts occurring, the profile drag dependent on lift increases; however, at the cruise condition, which is the focus of the present analysis, this effect can be neglected.

Overall, the agreement of the aerodynamic solver for the Flying V aircraft with experimental results and higher order codes is satisfactory. The Euler code accurately predicts shock waves location and strength, which is really promising for an aerodynamic shape optimization. Moreover, the obtained lift and drag coefficients values are encouraging since they agree really well with past RANS, DDES and DES simulations. JST is selected as the numerical solver due to its combined stability and accuracy.

3.3.2. NASA Common Research Model

As introduced in Section 1.1, the NASA CRM is adopted as a benchmark in order to assess whether the Flying V is aerodynamically more efficient than a state of the art tube-and-wing configuration. It is good practice to further verify the aerodynamic analysis method by comparing the results applied to the NASA CRM with estimations from open literature. The NASA CRM configuration has been designed by Vassberg et al. [9] in order to have a reference case for drag predictions, hence serve the AIAA Drag Prediction Workshops. It aims to reproduce the geometry of a modern, long-range commercial airplane operating at transonic flight conditions (M = 0.85). Besides, the advanced supercritical wing is attached to a Boeing 777-200ER fuselage geometry, which has a passenger capacity similar to the A350-900 (313 in two-class configuration) and similar range.

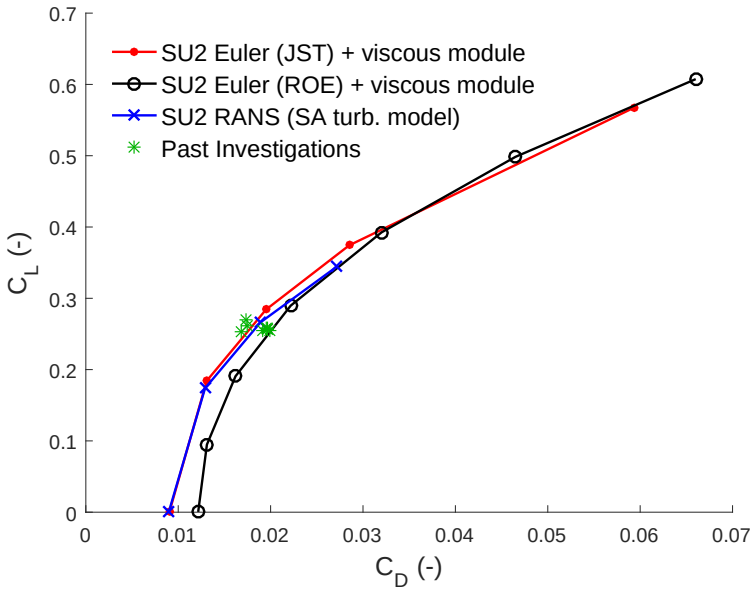

Figure 3.10: Onera M6 wing drag polar (M=0.8395). Past investigations reported by Durrani and Qin [60]

The geometry of the NASA CRM and 777-200ER are displayed in Figure 3.11. The NASA CRM, beside being object of many simulations and validation cases, has been analysed with SU2 by Palacios et al. [61]. Hence, the results of SU2 in the Euler version are combined with the viscous module (Section 2.5.1), and they are compared to the study performed by Ueno et al. [62]. It is a far-field drag analysis of the NASA CRM (wing, body and horizontal tail) based on the CFD simulations performed by JAXA for the fourth drag prediction workshop. The simulation is relative to Mach equal to 0.85, lift coefficient of 0.5 and Reynolds number of $5 \cdot 10^6$. The total drag counts resulting from the far-field analysis are 268 (slightly lower than 271, computed by JAXA).

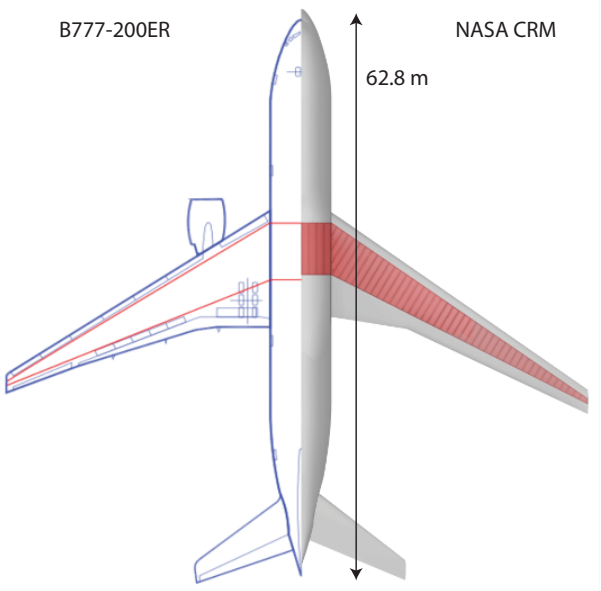

Figure 3.11: Geometry of the NASA CRM (right) and Boeing 777-200ER (left) [63]

The geometry of the NASA CRM used in the JAXA and current simulation features wing, fuselage, horizontal tail plane and wing-body fairing. Hence, engine nacelles, pylons and vertical tail are not included in the simulation. Since the Euler flow model is adopted for this project, the profile drag is calculated with Equation (2.19). Moreover, the NASA CRM, compared to the Flying V, has a fuselage. Hence, the form factor for this body is defined from Raymer [40] and can be expressed as:

$$FF = 1 + \frac{60}{\left(\frac{l}{d}\right)^3} + \frac{\frac{l}{d}}{400} \tag{3.3}$$

The dimensions and reference quantities of the different NASA CRM components are reported in Table 3.2. The grid used for this simulation is the same that is employed for the RANS analyses described by Palacios et al. [61]: it is displayed in Figure 3.12.

	Parameter (unit)	Value
Wing	Reference area (m^2)	383.7
	Reference chord (m)	7.0
	Span (m)	58.8
	Quarter chord sweep angle (deg)	35
	Average thickness to chord ratio (-)	0.108
Horizontal tail	Reference area (m^2)	99.9
	Reference chord (m)	4.6
	Span (m)	21.4
	Quarter chord sweep angle (deg)	37
	Average thickness to chord ratio (-)	0.090
Vertical tail *	Reference area (m^2)	55.5
	Reference chord (m)	5.2
	Height (m)	10.6
	Quarter chord sweep angle (deg)	46
	Average thickness to chord ratio (-)	0.110
Fuselage	Length (m)	62.8
	Diameter (m)	6.2

Table 3.2: NASA CRM reference quantities [9]. * The values of the vertical tail are extracted from the CAD provide to NASA by ONERA[1]

The total drag of the NASA CRM (wing, body and horizontal tail) predicted by SU2 and the viscous module (Section 2.5.1) is 0.0252. This value is slightly lower than 0.0268 and the difference is within 6%. This deviation might be due to the increase in wetted area of the wing body fairing, which is not accounted by the viscous module in the fuselage and wing profile drag components. Overall, the agreement is deemed to be satisfactory and the analysis method of Section 2.5.1 is verified not only with the Onera M6 wing but also with a full aircraft configuration, the NASA CRM. This verification is relevant because it allows to fairly compare the Flying V with a state of the art conventional configuration (see Section 4.7).

[1] Nasa Common Research Model. Retrieved in September 20, 2016 from https://commonresearchmodel.larc.nasa.gov/geometry/vertical-tail-geometry/

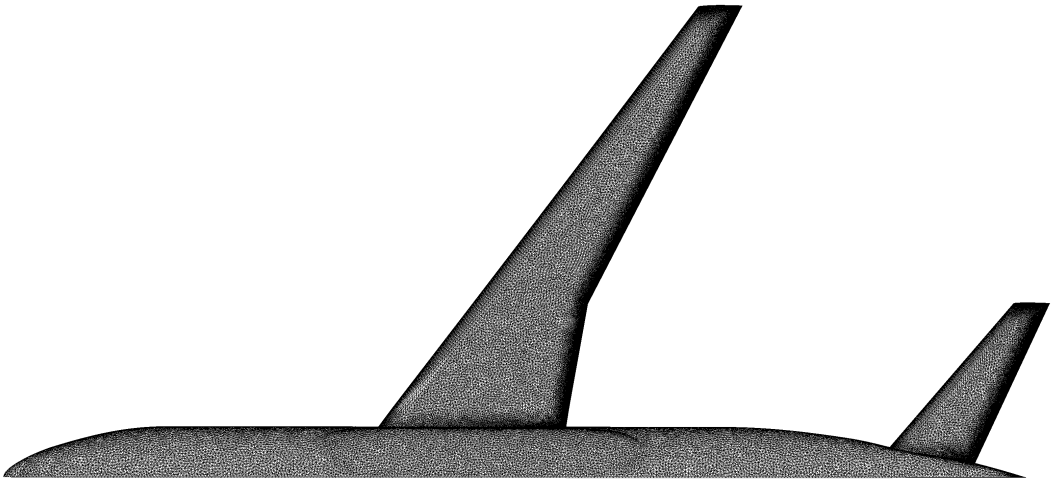

Figure 3.12: NASA CRM grid provided by SU2 Stanford team [61]

4

Results and Discussions

The aerodynamic design of the Flying V is performed at a single condition, the cruise point. The cruise weight is assessed by Benad during the preliminary assessment [8]:

$$W_{\text{cruise}} = 200,000 \text{ kgf} \tag{4.1}$$

This is based on a maximum take-off weight of 260,000 kgf. The nominal cruise lift coefficient can be defined according to cruise weight, Mach number, nominal altitude and reference area (equal to the wing surface area), considering ISA conditions:

$$C_{L_{\text{cruise}}} = \frac{2W_{\text{cruise}}}{p_{\text{cruise}}\gamma M^2_{\text{cruise}} S} \tag{4.2}$$

Where p_{cruise} is the air pressure at cruise condition, γ the heat capacity ratio of an ideal gas (1.4) and M_{cruise} the cruise Mach number. The cruise Mach number is equal to 0.85 (see Section 1.4.1) and the design altitude is chosen to be 13,000 m, slightly lower than the reference aircraft service ceiling (see Section 1.4.1). The deign lift coefficient of the Flying V resulting from Equation (4.2) is considerably lower than the reference aircraft one due to a bigger reference area. In particular, considering the reference area of the baseline configuration (895 m^2), the cruise lift coefficient is equal to 0.26. Although the wing area changes during the design process, the coefficients refer to the reference area of the baseline configuration. The design conditions are summarised in Table 4.1. It is relevant to remark that the SU2 is run with a fixed lift coefficient input, therefore the Flying V angle of attack is varied iteratively to converge to the required lift.

Parameter (unit)	Value
Mach (-)	0.85
$C_{L_{\text{cruise}}}$ (-)	0.26
p_{cruise} (Pa)	16510.38
ρ_{cruise} (kg/m^3)	0.27
T_{cruise} (K)	216.65

Table 4.1: Flying V design conditions

Since the weight and centre of gravity estimation module is not available, an assumption has to be made in order to estimate the reference point for the pitching moment computation. Therefore, for each Flying

V planform, the neutral point is computed with AVL, and the centre of gravity is placed ahead of it in order to guarantee longitudinal static stability. A typical transport aircraft usually have a static margin (distance between neutral point and centre of gravity) of 5% of the MAC at the most-aft centre of gravity position [40]; however, since the MAC of the Flying V is twice as much the reference aircraft one, a static margin of 2.5% is chosen in order to have a similar absolute distance. Hence, the centre of gravity is assumed to be 6% MAC ahead of the neutral point at the design point, as done by Benad [8]: this distance is around 1 m for the baseline configuration and is assumed to be an average between the most forward and aft possible centre of gravity locations.

The Flying V baseline configuration is mainly deduced from the Airbus report [8] and the NASA/Langley Withcomb supercritical airfoil with thickness to chord ratio of 9% is selected for sections IV and V (Figure 2.6), due to satisfactory performance in transonic regime [64].

4.1. Test Case Description

The different steps of the Flying V aerodynamic design procedure are shown in Figure 2.3 and extensively explained in Section 2.3. The objectives, constraints and design variables of each design step are reported in Table 4.2. The multi-fidelity design space exploration does not have hard constraints and the objectives are verified by the designer's judgement, hence they are more qualitative. On the other hand, the three optimization procedures have the same objective: maximize the lift to drag ratio.

Design Step	Objective(s)	Constraints	Design Variables
Design Space Explor.	Reduce induced drag Reduce pitch down Reduce supersonic flow Improve isobars	-	Λ_2, λ, ϵ_{IV}, ϵ_V, $\bar{y}_{oval}$, $\bar{y}_{nose}$, $\bar{y}_{rear}$
Dual step Planform Optimiz.	min $-L/D$	$C_m \geq -0.015$ $\alpha \leq 3^\circ$ $n_{pax} \geq 440$	$\bar{y}_{planf}$
Dual step Airfoil Optimiz.	min $-L/D$	$C_m \geq -0.010$ $\alpha \leq 3^\circ$ $n_{pax} \geq 440$ $(t/c)_{IV,V} \geq 0.085$	$\bar{y}_{CST}$, ϵ_{IV}, ϵ_V, $\bar{y}_{rear}$
Single step Optimiz.	min $-L/D$	$C_m \geq -0.015$ $\alpha \leq 3^\circ$ $n_{pax} \geq 440$ $(t/c)_{IV,V} \geq 0.085$	$\bar{y}_{planf}$, $\bar{y}_{CST}$

Table 4.2: Test case: objective(s), constraints and design vectors of each design step

Four types of inequality constraints are set for the optimization procedures:

- Pitching moment coefficient (C_m). It is constrained so that the Flying V can be trimmed with a negligible force at the design condition.
- Angle of attack (α). It is equal to the deck angle, which is limited to 3° to favour passenger acceptance.
- Passenger capacity (n_{pax}). It must be higher than the reference aircraft one, 440 passengers in a single class layout.

- Thickness to chord ratio (t/c). This constraint is active only when the airfoil parameters are free to vary (airfoil optimization and single step optimization) with the aim of avoiding excessively thin wings.

The DE algorithm requires some inputs: the population size is set to 4 times the number of design variables and the maximum number iterations to 20. Moreover, for the mutation constant F, dithering is used in order to speed up convergence: for each generation, the constant is chosen between 0.5 and 1. The crossover is selected to be 0.7: this value, if too high, might impact on the population stability due to a big amount of mutants progressing into the next generation. Each SU2 simulation is stopped after 100 iterations because the results in terms of aerodynamic coefficients are within a 0.5% error with respect to the converged solution: this helps saving computational time. Such a fast convergence is achieved by the use of multigrid. Each run takes about 20 minutes to complete on a single machine with the following performances: Intel i7 2.4 GHz processor, 16 Gb RAM DDR3 1600 Mhz.

	Variable (unit)	Config. 0	Config. 1	Config. 2	Config. 3	Config. 4
Planform shape	S (m^2)	895.0	895.0	883.7	883.7	883.3
	b (m)	65.0	65.0	65.0	65.0	65.0
	c_r (m)	24.0	24.0	24.8	24.8	24.0
	Λ_1(°)	63.0	63.0	63.6	63.6	64.4
	Λ_2(°)	15.0	30.0	33.8	33.8	37.8
	k_1 (-)	0.400	0.380	0.385	0.385	0.386
	k_2 (-)	0.600	0.600	0.588	0.588	0.623
	λ (-)	0.18	0.15	0.13	0.13	0.13
	ϵ_{IV} (°)	-1.5	-4.0	-4.7	-4.3	-4.3
	ϵ_V (°)	-1.0	-3.0	-4.9	-5.0	4.4
Oval cross section 2	H_1 (m)	0.7	0.8	0.8	0.8	0.8
	H_3 (m)	0.5	0.6	0.6	0.6	0.6
Oval cross section 3	H_1 (m)	0.5	0.6	0.6	0.6	0.6
	H_3 (m)	0.7	0.7	0.7	0.7	0.7
Oval cross section 4	H_1 (m)	0.4	0.4	0.4	0.4	0.4
	H_3 (m)	0.7	0.7	0.7	0.7	0.7
Nose cone	a_{up} ($\sqrt{m}$)	0.8	0.9	0.9	0.9	0.9
	a_{low} ($\sqrt{m}$)	0.7	0.6	0.6	0.6	0.6
	e_{up} ($1/m^2$)	-2.5	-2.0	-2.0	-2.0	-2.0
	e_{low} ($1/m^2$)	-1.5	-1.0	-1.0	-1.0	-1.0
Rear Airfoil section I	c_{up} (10^{-3}/m)	-0.10	-0.08	-0.08	-0.05	-0.08
	c_{low} (10^{-3}/m)	-0.10	-0.08	-0.08	-0.07	-0.08
	z_{TE} (m)	-0.40	-0.55	-0.55	-0.50	-0.55
Rear Airfoil section II	c_{up} (10^{-3}/m)	-0.20	-0.10	-0.10	-0.11	-0.10
	c_{low} (10^{-3}/m)	0.10	0.10	0.10	0.15	0.10
	z_{TE} (m)	-0.100	-0.070	-0.070	-0.069	-0.070
Rear Airfoil section III	c_{up} (10^{-3}/m)	-0.100	-0.010	-0.010	-0.012	-0.010
	c_{low} (10^{-3}/m)	0.1	0.1	0.1	0.2	0.1
	z_{TE} (m)	-0.05	-0.05	-0.05	-0.04	-0.05

Table 4.3: Values of the design variables for the 5 configurations

The variables values of the 5 different configurations (Figure 2.3) are reported in Table 4.3. The CST pa-

rameters of the 5 configurations are reported in Table 4.4 (the CST of configurations 0, 1 and 2 are the same). The aerodynamic results are reported in Table 4.5. In the following paragraphs, the results of the subsequent steps are thoroughly discussed.

Config.-Prof.	$\bar{y}_{CST}$
0,1,2-IV	{0.1557, 0.0533, 0.1783, 0.0599, 0.1853, 0.2543, -0.1502, -0.1091, -0.0309, -0.3185, 0.0493, 0.2168}
3-IV	{0.1335, 0.0617, 0.2019, 0.0308, 0.1520, 0.2601, -0.0843, -0.0712, -0.0296, -0.3329, 0.0308, 0.1246}
4-IV	{0.0879, 0.0658, 0.2116, 0.0794, 0.2394, 0.2292, -0.1328, -0.0882, -0.3153, -0.3057, 0.0691, 0.2035}
0,1,2-V	{0.1557, 0.0533, 0.1783, 0.0599, 0.1853, 0.2543, -0.1502, -0.1091, -0.0309, -0.3185, 0.0493, 0.2168}
3-V	{0.1224, 0.0685, 0.2324, 0.0879, 0.1779, 0.2662,-0.1128, -0.0836, -0.0372, -0.2936, 0.0454, 0.2339}
4-V	{0.1354, 0.0680, 0.2030, 0.0778, 0.1419, 0.2866, -0.0985, -0.0841, -0.0254, -0.3873, 0.0615, 0.1711}

Table 4.4: CST variables of the 5 Flying V configurations. Configurations 1,2,3 have the same values

Config.	C_m Constr.	α (°)	C_L(-)	C_D(-)	C_{D0}(-)	$C_{D_{\text{inv}}}$(-)	M_{max}(-)	C_m(-)	C_L/C_D(-)
0	-	1.4	0.26	131	60.3	70.7	1.47	-0.053	20.0
1	-	2.4	0.26	115	58.4	56.6	1.41	-0.024	22.8
2	$C_m > -0.015$	2.7	0.26	113	57.5	55.5	1.32	-0.014	23.3
3	$C_m > -0.010$	2.8	0.26	112	57.4	54.6	1.25	-0.009	23.5
4	$C_m > -0.015$	2.8	0.26	111	57.2	53.8	1.25	-0.014	23.7

Table 4.5: Summary of the aerodynamic coefficients based on the same reference area. Drag coefficients are expressed in counts and C_{D0} includes also fins, pylons and nacelles

4.2. Multi-fidelity Design Space Exploration

Before starting the design procedure, the baseline configuration (0) is analysed with SU2. The results of the 5 configurations in terms of lift and local lift coefficient distribution are displayed in Figure 4.1 and Figure 4.2 respectively. In addition, the Mach contours are depicted in Figure 4.3.

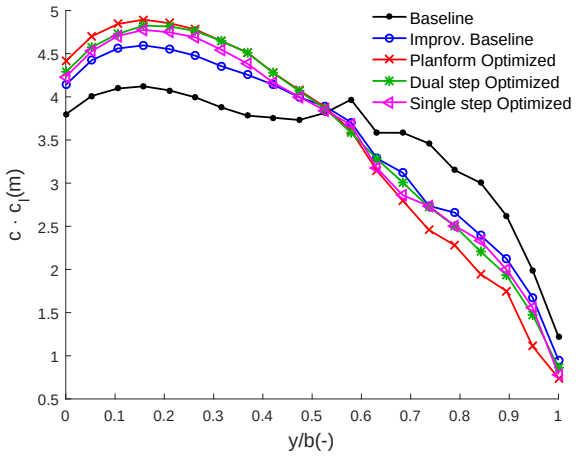

Figure 4.1: Spanwise load distribution of the 5 configurations

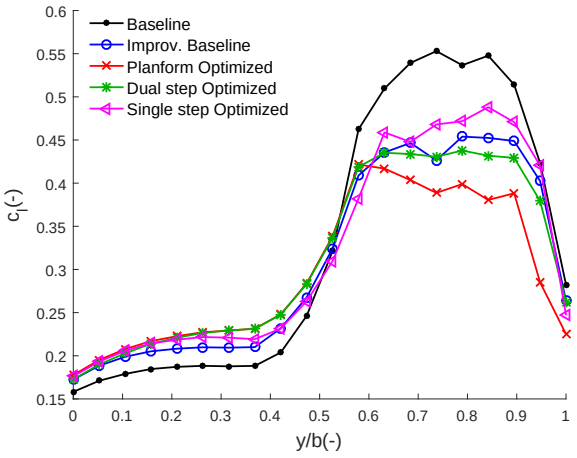

Figure 4.2: Local lift coefficient distribution of the 5 configurations

In the lift distribution of Figure 4.1 (black line), a relevant peak can be noticed at $y/b = 0.6$, where the leading edge kink is located. The peak occurs due to two main reasons: strong leading edge sweep change

and big increase in local lift coefficient of the Withcomb airfoil, positioned at this spanwise position. This sudden increase in local lift coefficient is shown in Figure 4.2: in particular, the outboard local lift coefficient is remarkably higher than the one predicted by Benad [8]. The difference is due to the fact that a supercritical airfoil is used for the outboard wing, which entails higher lift coefficient because of the rear loading, still maintaining the same twist distribution of Benad [8]. However, high local lift coefficients entail high Mach numbers, hence are responsible for wave drag increase. This is the case of the baseline Flying V configuration, where the maximum Mach number over the wing surface is 1.47 (see Table 4.5). In particular, by looking at the Mach contours of Figure 4.3(a), a shock wave appears at a considerable aft location: this means that the flow accelerates for a big portion of the airfoil and is subsequently decelerated with a strong shock wave [26]. The 15° leading edge sweep angle proves to be too small for an aircraft flying in high-subsonic regime. In a nutshell, the Flying V baseline configuration features excessive outboard load, which comes with three non negligible drawbacks:

- High inviscid drag predicted by SU2, mainly due to excessive wave and vortex induced drag.
- Strong pitching moment coefficient (see Table 4.5), which must be trimmed by elevon deflections. It is not desirable because of the relevant wave drag penalty.
- The high Mach number peaks may cause boundary layer induced separation, which is not taken into account by an Euler solver [26]. Therefore, the actual drag might be higher than the one computed by SU2.

As reported in Table 4.2, the aim of the design space exploration is to improve the spanwise load distribution (reduce the induced drag and pitch down moment), reduce the supersonic region over the outboard wing surface and align the isobars close to the root. The first goal can be achieved by modifying the spanwise twist distribution and thickness; the second one can be attained by sweeping the outboard wing back and changing the taper ratio. Finally, the third goal deserves an additional explanation: the isobars need to be perpendicular to the streamwise direction at the root due to symmetry requirements. Hence, they tend to bend rearward close to the root in a swept back wing: the pressure peak is shifted backward, which may cause a steeper pressure gradient. Due to the suction in the rear part, an additional drag force is generated. This effect can be partially removed by moving the root profile thickest point forward in order to shift the suction peak, and reducing the aft camber [26]. The design variables chosen for the multi-fidelity design space exploration are reported in Table 4.2. There are no hard constraints and the convergence is achieved after 11 manual SU2 iterations (external loop of Figure 2.4).

The improved baseline configuration (1), resulting from the design space exploration, represents the first step towards reduced drag and pitch down. As reported in Table 4.3, sections IV and V are twisted down to unload the outboard wing: this effect is evident in Figure 4.1 and Figure 4.2, where the maximum local lift coefficient decreases from 0.55 to 0.45. Besides, the supersonic region over the wing surface is reduced, as depicted in Figure 4.3(b): also the maximum Mach number decreases from 1.47 to 1.41. This is mainly attained by changing the outer sweep angle from 15° to 30°. Furthermore, the improvement of the root pressure distribution is shown in Figure 4.4: the suction peak is moved forward so that the pressure recovery towards the trailing edge is less steep. The rear loading close to the root is completely removed in order to reduce the Flying V pitch down moment. The aerodynamic performances of the improved baseline configuration can be compared to the baseline one:

- Relevant reduction of inviscid drag (from 70.7 to 56.6 drag counts, see Table 4.5), obtained with a more elliptical lift distribution, reduction in outboard local lift coefficient and maximum Mach number. The first effect entails lower induced drag, whereas the second and third ones are responsible for decreased wave drag.

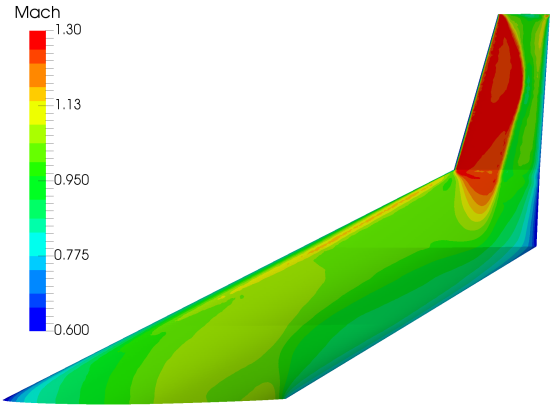

(a) Baseline configuration (0)

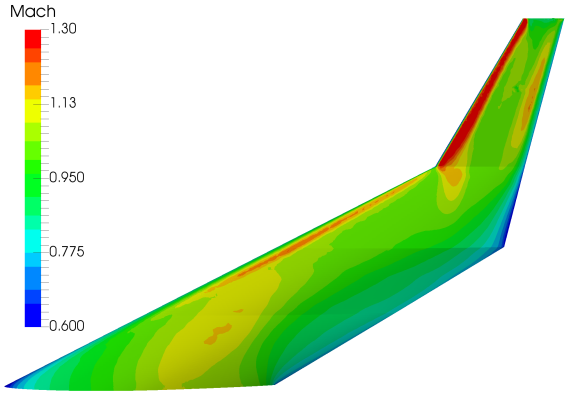

(b) Improved baseline configuration (1)

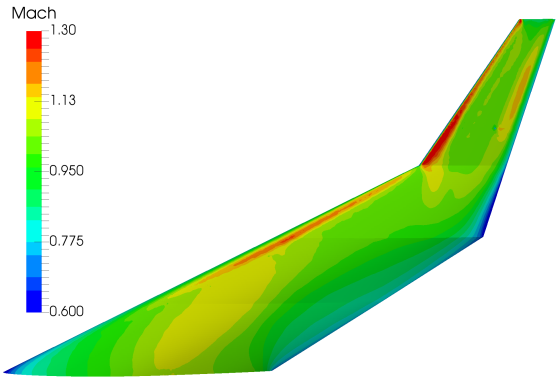

(c) Planform optimized configuration (2)

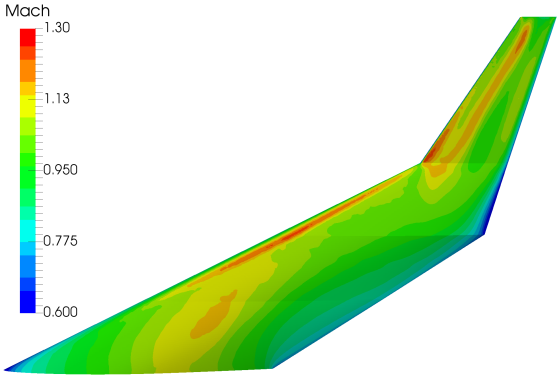

(d) Dual step optimized configuration (3)

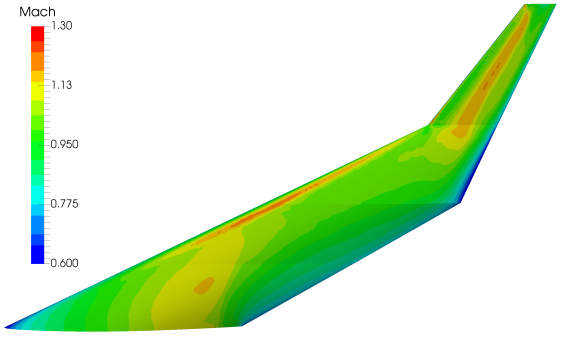

(e) Single step optimized configuration (4)

Figure 4.3: Mach contours of the 5 configurations

- Halved pitching moment coefficient, from -0.0533 to -0.0241, see Table 4.5.

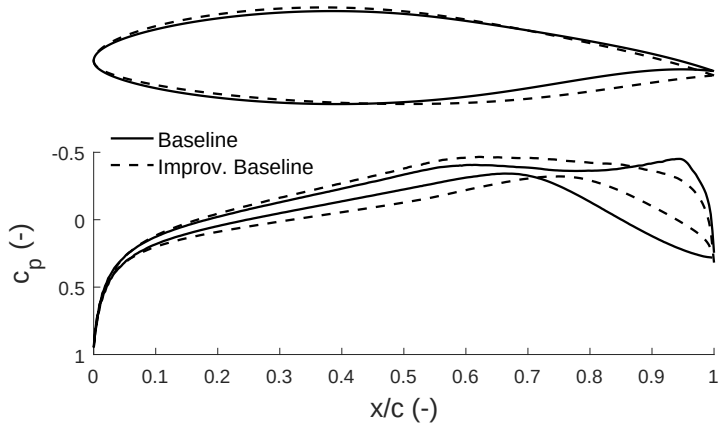

Figure 4.4: Root effect improvement: the suction peak is moved forward and the pressure gradient is reduced

The improved baseline configuration already represents a big step forward, however additional improvements are investigated with automatic optimization procedures, outlined in the next sections.

4.3. Dual Step Optimization

The dual step optimization is one of the two paths towards the optimum configuration (Figure 2.3). It features subsequent planform and airfoil SU2 Euler optimizations.

4.3.1. SU2 Euler Planform Optimization

The SU2 Euler planform optimization is applied to the improved baseline configuration (Figure 2.3). The design variables are the 10 planform shape parameters reported in Table 2.4: since the span is constrained to the 65 m gate limit (Section 1.4.1), the number of parameters decreases to 9. The constraints regarding angle of attack, pitching moment coefficient and passenger capacity are specified in Table 2.4. In addition, the DE algorithm requires lower and upper bounds for the variables, so that the elements of the population are chosen within the feasible design space: ±20% of the initial value is selected, except for the twist angles (±100%). The planform optimization procedure takes 32.85 hours in total. It is important to remark that two tricks are adopted to save computational time:

1. Five simulations are simultaneously run in parallel. Hence, 5 simulations take 27 minutes in total, much less than 100 minutes that would be required if the simulations are run in series (20 minutes per SU2 analysis, as reported in Section 4.1).

2. Each design, before being analysed with SU2, is tested with AVL, which takes few seconds. This is used to filter out non feasible design points when one of the following criteria is not satisfied: $C_m \geq -0.025$ and $\alpha \leq 4°$. A certain margin is used with respect to the actual constraints due to the relatively low accuracy of AVL. This low-fidelity filter proves to be computationally really efficient because it avoids to run SU2 if the design point is unfeasible.

In Figure 4.1, the lift distribution of the planform-optimized configuration (red line) is compared to the previous ones: the trend resembles an averaged elliptical/triangular distribution, which provides the best aerodynamic trade off, as proved by Qin et al. [18, 19]. Although the elliptical distribution entails the lowest induced drag, the triangular one gives the highest wave drag reduction: a combination of the two proves

to be the most efficient. This is mainly obtained by sweeping the outboard wing further back to 33.8°, reducing the taper ratio from 0.15 to 0.13 and increasing the nose down wash out (Table 4.3). The last change is responsible for the decrease in local lift coefficient in the outboard wing, as displayed in Figure 4.2. The maximum Mach number is lowered to 1.32 and the supersonic region occurs only close to the trailing edge: the pressure gradient is not really steep, which means that a shock wave does not appear (see Figure 4.3(c)). These modifications are responsible for the reduction in inviscid drag coefficient of 2 counts, reported in Table 4.5. Moreover, the profile drag is reduced by diminishing the wetted area (the wing area is 1.5% lower) and increasing the sweep angle (see Equation (2.21)). All the constraints are satisfied: the deck angle is 2.72°, the pitching moment coefficient is -0.0139 and the required payload capacity is respected.

4.3.2. SU2 Euler Airfoil Optimization

The planform optimized configuration (2) is the starting point for the SU2 Euler airfoil optimization, as shown in Figure 2.3, in which the design variables are the CST coefficients and 2 twist angles of profiles IV and V, and the 9 rear airfoil parameters of sections I, II and III (Table 4.2). The design space is limited by the constraints reported in Table 2.4. In particular, the thickness to chord ratio of profiles IV and V (Figure 2.6) must be higher than 8.5% to avoid a really thin outer wing, which may involve a relevant weight penalty. Different upper and lower bounds are chosen for the design variables:

- (30%, 300%) of the initial values for c_{up} and c_{low} of sections I, II and III.
- (40%,160%) of the initial values for z_{TE} of sections I, II and III.
- ±50% of the initial values for the CST coefficients of sections IV and V.
- ±10% of the initial values of the twist angles ϵ_{IV} and ϵ_{V}.

This analysis is computationally more costly than the planform optimization due to a larger amount of variables involved (35 compared to 9). The total time is 133.22 hours.

In Figure 4.1 the load distribution of the dual step optimized Flying V (green line) is compared to the previous designs. The spanwise load is similar to the one of the previous configuration (red line); however, the local lift coefficient of the outboard wing is slightly higher and the load is reduced inboard (Figure 4.2).

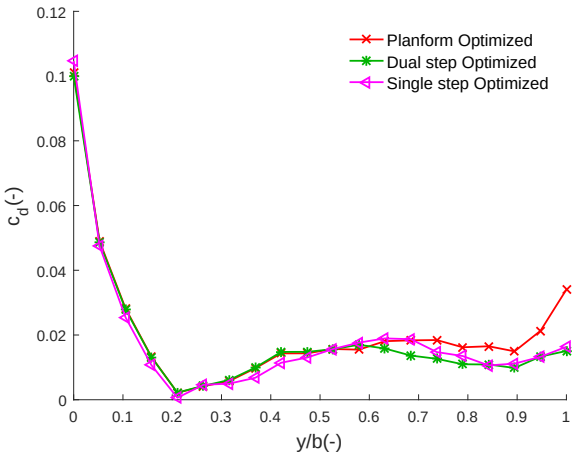

Figure 4.5: Local inviscid drag coefficient distribution of configurations 2,3 and 4

The aerodynamic efficiency of the outboard wing is greatly improved by the airfoil optimization: the local drag coefficient decreases, as shown in Figure 4.5. It is noticeable that the green and red lines start diverging

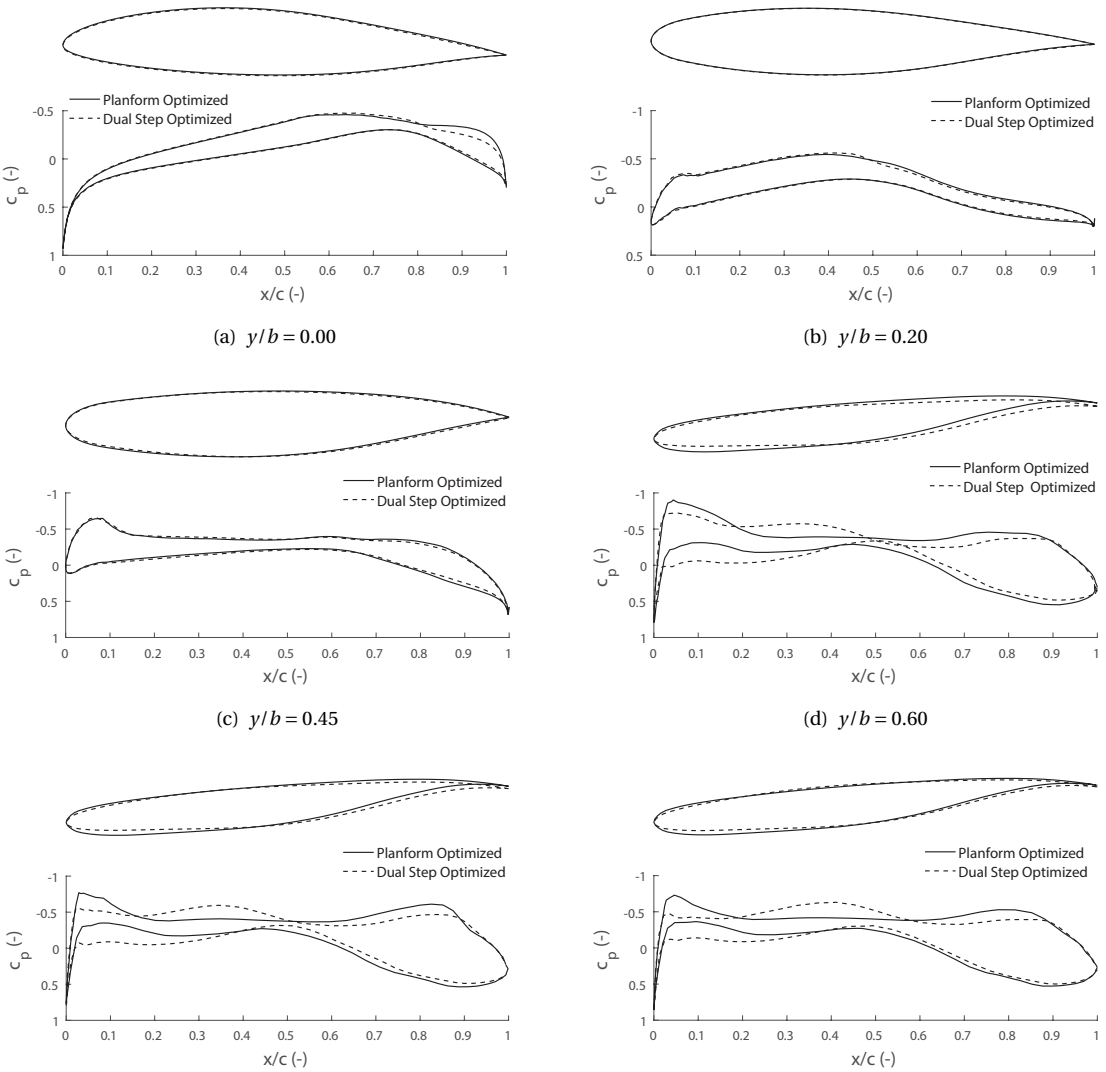

(a) $y/b = 0.00$ (b) $y/b = 0.20$

(c) $y/b = 0.45$ (d) $y/b = 0.60$

(e) $y/b = 0.75$ (f) $y/b = 0.90$

Figure 4.6: SU2 Euler airfoil optimization: comparison of pressure coefficient distributions at 6 spanwise locations

at $y/b = 0.6$, where section IV is positioned. In particular, the outboard portion of the wing is unconstrained and free to vary, whereas the inboard part is driven by the cabin parameters. Moreover, the local inviscid drag coefficient is remarkably higher close to the root: this is due to the higher downwash, typical of highly swept wings, which is responsible for vortex induced drag generation. The thickness to chord ratio of profiles IV and V is 8.6% and 9.5% respectively, hence the constraint is respected.

In Figure 4.6, six different spanwise sections of the dual step optimized Flying V (dotted lines) are compared to the planform optimized ones (solid lines), together with the pressure coefficient distributions. The root airfoil, shown in Figure 4.6(a), is slightly modified and the trailing edge pressure recovery is smoother and less steep. The sections of Figure 4.6(b) and Figure 4.6(c) (in which the rear part of the airfoil only is allowed to change, see Section 2.4) do not undergo meaningful modifications. In the outer wing airfoils, shown in Figures 4.6(d) to 4.6(f), four beneficial changes can be noticed:

- The leading edge radius is smaller, which entails lower supervelocities and reduced maximum Mach over the surface (from 1.32 to 1.25, see Table 4.3).

- The airfoil curvature in the rear part is reduced, hence the adverse pressure gradient is less steep.
- The flow accelerates towards the mid chord, where the maximum thickness to chord ratio is, then it is smoothly decelerated.
- Front loading is created and rear loading is slightly reduced.

Overall, the pressure distribution of the outboard wing is improved. These modifications justify the higher aerodynamic efficiency of the outboard wing and the reduction in pitch down moment. The former is appreciable in the Mach contours of Figure 4.3(d), where the supersonic flow area decreases considerably. This Flying V configuration results in a higher lift to drag ratio (23.5), obtained by saving 1 drag count.

4.4. Single Step Optimization

As shown in Figure 2.3, also a single step SU2 optimization for maximum lift to drag ratio is applied to the improved baseline configuration (1). The variables and inequality constraints are reported in Table 4.2. The total computational time is 125.36 hours, slightly lower than the airfoil optimization time, mentioned in Section 4.3.2: in particular, the 9 rear airfoil part parameters ($\bar{y}_{\text{rear}}$) are not involved in this analysis in order to reduce the computational effort.

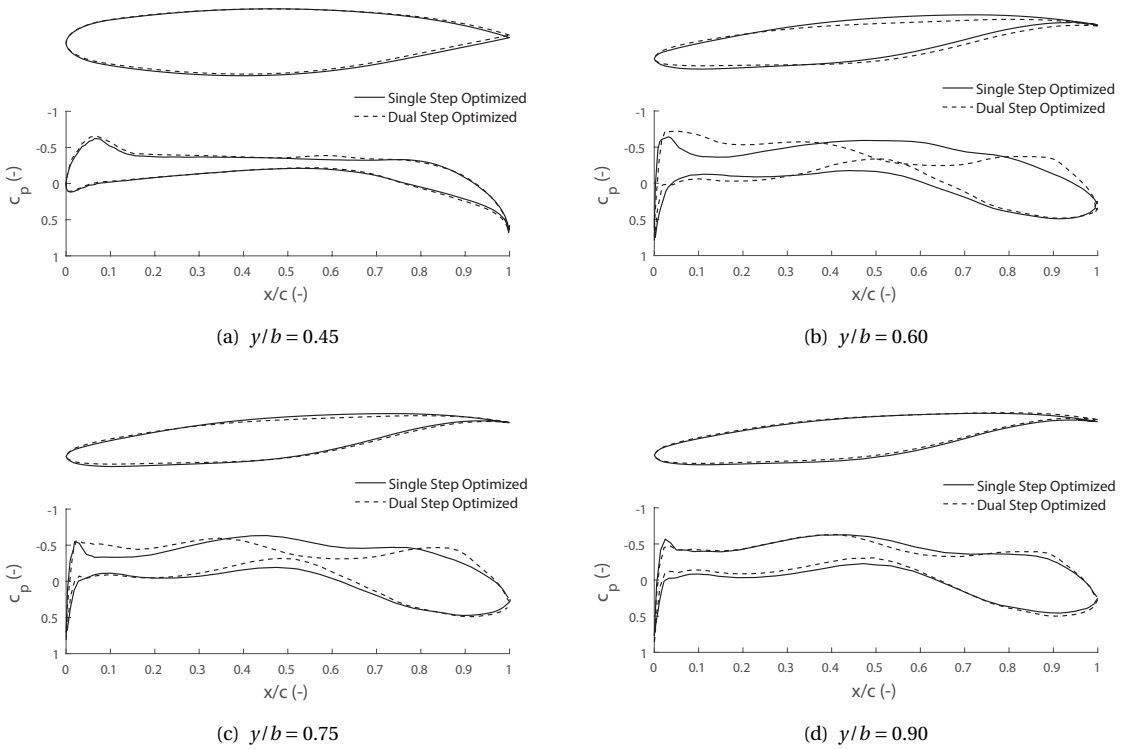

(a) $y/b = 0.45$ (b) $y/b = 0.60$

(c) $y/b = 0.75$ (d) $y/b = 0.90$

Figure 4.7: SU2 Euler single step optimization: comparison of pressure coefficient distributions at 4 spanwise locations (M = 0.85, C_L=0.26)

The lift distribution of the single step optimized configuration (magenta line in Figure 4.1) is in agreement with the double step optimized one (green line). On the other hand, the outboard wing of this configuration is more slender than the dual step optimized one, as visible in Figure 4.3(e), which entails higher outboard local lift coefficient (Figure 4.2). The wing area resulting from the single step optimization is similar to the planform optimized one (about 883 m^2, Table 4.3). The sweep angles Λ_1 and Λ_2 are slightly higher and the

nose down wash out is still present. The pressure coefficient distributions of the single step optimized configuration are compared to the dual step optimized ones in Figure 4.7. Only the profiles at y/b higher than 0.45 are shown, since the inboard rear fairings are fixed.

Again, as discussed in Section 4.3.2, front loading is introduced and the trailing edge pressure recovery is less steep (see Figures 4.7(b) to 4.7(d)). Profile V (Figure 2.6) of the two configurations is really similar, as reported in Table 4.4 and displayed in Figure 4.7(d). In particular, the profile shape found by the optimizer is really similar in the two optimization paths (dual and single step). The local inviscid drag coefficient distribution is shown in Figure 4.5 (same nondimensionalization of the other 2 curves): it features a trend similar to the dual step optimized Flying V, it is slightly lower from $y/b = 0.3$ to $y/b = 0.55$ and higher from $y/b = 0.55$ to $y/b = 0.85$. The maximum Mach number over the wing is 1.25 (Table 4.5), which represents a remarkable achievement. The total drag coefficient is further reduced of 1 count, compared to the dual step optimized Flying V configuration (Table 4.5). The constraints are satisfied. In particular the thickness to chord ratio of profiles IV and V is 9.5% and 9.2% respectively. In a nutshell, the single step optimization provides a better aerodynamic result at a lower computational cost (125.36 hours) if compared to the dual step procedure, which takes around 167 hours in total.

4.5. Fin Sizing Results

The fin sizing procedure, described in Section 2.3, is subsequently applied to the single step optimized configuration. The variables, bounds and optimum values are reported in Table 4.6.

Variable	Initial value	Bounds	Optimum value
Λ_{fin} (deg)	30	$20 < \Lambda < 50$	36
A_{fin} (-)	2.0	$1.0 < A < 3.0$	2.3
λ_{fin} (-)	0.60	$0.45 < \lambda < 0.70$	0.45

Table 4.6: Fin design variables, bounds and optimum values.

The optimization constraints are represented by the three driving requirements outlined in Table 2.1. In order to check the directional static stability requirement, the tail-off directional stability derivative at the most aft centre of gravity location (obtained with a 2.5% static margin) is computed by SU2 and it is equal to -0.0187 1/rad. This means that the Flying V is directionally unstable without a vertical surface behind the centre of gravity. Perhaps the thick inboard wing, which is ahead of the centre of gravity, has a destabilizing effect. The other two constraints are related to the required rudder deflection at two critical conditions: OEI condition at take off and landing in maximum crosswind.

The fin resulting from this design procedure has a surface area of 13 m^2: considering that two twin fins are used, the total area is 26 m^2. With the engines line of thrust located at $y/b = 0.1$, the OEI condition is not the most critical condition, whereas the directional static stability target is the most demanding. The optimum design variables are reported in Table 4.6: the taper ratio is on the lower bound where the area is minimum, the aspect ratio is 2.3 in order to guarantee the required lift slope and the sweep angle is slightly higher than the initial value to ensure a longer arm. Since the design is purely aerodynamic, the impact of the taper ratio on the structure is not taken into account, hence a multidisciplinary analysis will be needed. A sweep angle of 36° is also beneficial to handle maximum sideslip angles: the value is within the range proposed by Obert [38] for jet transport aircraft, from 33 to 45.

The required fins area is about 50% higher than the one predicted by Benad [8], equal to 16 m^2, based on a

dynamic stability study, in which the derivatives are computed by a vortex lattice method. If the static stability constraint is relaxed (neutral stability required), the OEI condition becomes the most critical, therefore the surface area is slightly reduced to 24 m^2. If the neutral stability constraint is the only one active, the total area required is 20 m^2: in this case the rudder deflection required in OEI condition is 28°, higher than the maximum allowed. The fin of Table 4.6 is used to analyse the full Flying V (wing, fins, nacelles and pylons). Being the tail-off stability derivative approximately the same for the 5 configurations, the area of the fins of the different Flying V is within a 5% difference. Therefore, their fin profile drag is within the same deviation.

4.6. Aerodynamic Results Summary

In this section, the overall results of the 5 full Flying V configurations (with fins) are discussed. The drag polar is displayed in Figure 4.8. Since the goal of the analysis is to evaluate the aerodynamic cruise performances, only conditions relatively close to the design point are shown. The drag coefficient at the cruise point is reduced by the multi-fidelity design space exploration of 16 counts and then 4 additional drag counts are saved with the optimization procedures. It is also important to notice that the distance between the curves increases at high lift coefficients: it means that the baseline configuration deteriorates more rapidly. This is even more appreciable in Figure 4.9, where the maximum lift-to-drag ratio is plotted versus the lift coefficient: it can be obtained when the Flying V is trimmed without any elevon deflection. In particular, the maximum lift-to-drag ratio of the optimized configurations (2, 3 and 4) is almost flat above the design lift coefficient, whereas decreases in case of the configurations 0 and 1 (defined in Figure 2.3). As predictable, being the design lift coefficient relatively low, the Flying V is aerodynamically more efficient at higher lift coefficients, which mean higher altitudes at the same Mach number. For instance, even though the Flying V is optimized at the lift coefficient of 0.26, the highest lift to drag ratio of the dual step optimized Flying V is attained at a lift coefficient 10% higher than the design one, at an altitude of 13,600 m. It is expectable that the aerodynamic efficiency will be even higher if the shape optimization is performed at this condition.

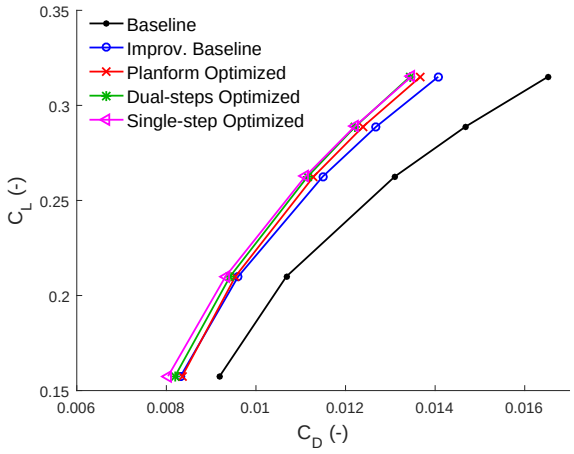

Figure 4.8: Drag polar of the 5 configurations. Limited lift coefficient are used

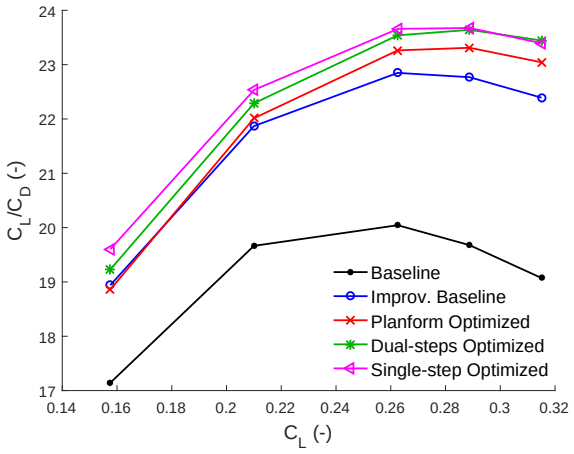

Figure 4.9: Maximum lift to drag ratio versus lift coefficient of the 5 configurations

However, the selection of the cruise altitude involves various disciplines. Even though the maximum aerodynamic efficiency for a given Mach number is obtained at high altitudes, transport airplanes usually end up flying lower due to the following reasons:

- The engine available thrust and specific fuel consumption decrease when increasing the altitude due to the lower air density, which entails lower mass flow rate. Bigger engines are required to fly at higher

speeds.

- At higher altitudes, the pressure difference between inside and outside the pressurised cabin hull is bigger. This usually requires a more resistant structure, hence heavier: perhaps, at this altitude the difference might be negligible.
- The aircraft is subjected to a buffet limit, that can be approached at relatively high Mach numbers and lift coefficients. Therefore, flying at higher lift coefficients decreases the buffet margin. In particular, the maximum local Mach over the wing goes up to 1.3, which is above the limit of 1.25 imposed by design guidelines.

In a nutshell, the cruise altitude decision is based on a careful trade off between multiple disciplines.

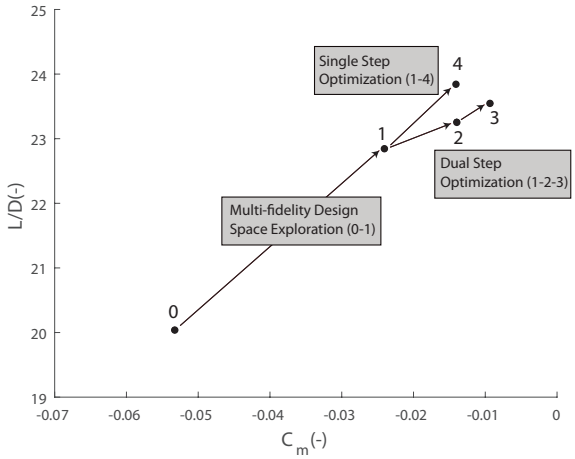

Figure 4.10: Maximum lift to drag ratio versus pitching moment coefficient of the 5 configurations

In Figure 4.10, the maximum lift to drag ratio is plotted versus the pitching moment coefficient for the 5 configurations. The design space exploration allows to increase the lift to drag ratio from 20.0 to 22.8 and halve the pitch down moment (Table 4.5). Subsequently, two different optimization paths are applied to configuration 1. The single step procedure produces a higher gain in terms of aerodynamic efficiency, compared to the dual step procedure. The pitch down is further diminished by both the procedures: in particular, as reported in Table 4.2, the pitching constraint of the airfoil optimization is more strict, hence a lower coefficient (in absolute value) is achieved.

4.7. Results Comparison with NASA CRM

The fundamental goal of this project is to assess whether the aerodynamic performances of the Flying V are better than the reference aircraft ones. The most reliable and effective way of comparing the Flying V aerodynamic performances with the A350-900 ones would require testing the two configurations with the same tool. However, this is not applicable within this research project for two relevant reasons:

- The reference aircraft data is not available.
- Implementing the full conventional configuration (geometry, mesh generation and verification) within ParaPy exceeds the time limit available to complete the project.

Therefore, as mentioned in Section 1.1, the NASA CRM configuration is taken a benchmark. The geometry of the NASA CRM is introduced in Section 3.3.2. The geometry of the NASA CRM used in the simulation features wing, fuselage, horizontal tail plane and wing-body fairing. Hence, engine nacelles, pylons and vertical tail

are not included in the simulations: the same holds for the Flying V model. They are separately analysed by the viscous module only. Moreover, in order to make a fair comparison, the following expedients are adopted:

- The same nacelle and pylon drag of the Flying V is assumed. This is computed with empirical equations, described in Section 2.5.1.
- The vertical tail geometry is provided by ONERA[1]. The dimensions are extracted by the CAD file and they prove to be really similar to the Boeing 777-200ER.
- The same flight conditions, namely Mach number, air temperature and pressure are considered.
- A similar grid refinement is adopted.

	C_L(-)	C_D(-)	C_{D0}(-)	$C_{D0}S_{\text{ref}}$(m^2)	$C_{D_{\text{inv}}}(-)$	$C_L/C_D(-)$
Flying V (config. 4)	0.26	111	57	5.1	54	23.7
NASA CRM	0.5	264	140	5.4	124	18.9

Table 4.7: Aerodynamic results comparison between Flying V and NASA CRM. The drag coefficients are reported in counts

The results are reported in Table 4.7. The profile drag of the NASA CRM computed by the viscous module is equal to 140 drag counts: this corresponds to a parasite drag area of 5.4 m^2, slightly higher than the one of the Flying V (5.1 m^2). This difference is a result of the bigger wetted area of the NASA CRM. The inviscid drag computed by SU2 is 124 counts. Therefore, the lift to drag ratio of the Flying V is 23.7, 25% higher than the one of the NASA CRM (18.9). The comparison between the two arrangements present one limitation, which needs further investigation. In particular, the twin fins of the Flying V are placed on the wing tips, hence the interference with the wing can not be neglected: this interference can be both beneficial in terms of vortex induced drag (winglet function) and detrimental in terms of wave drag. This is in contrast with the NASA CRM, where the vertical tail is attached to the fuselage and the interference is less critical. However, the difference in lift to drag ratio is 25%, therefore the Flying V would perform better than the NASA CRM also if a considerable drag penalty is taken into account. To conclude, the objective of this investigation is satisfactory achieved: additional aerodynamic studies are necessary to analyse low speed performances and maximum lift capabilities.

4.8. From Conceptual to Preliminary Design

The main research question of the MSc project can be answered positively. The aerodynamic advantages claimed by the preliminary assessment performed at Airbus [8] are confirmed by this analysis. The maximum lift to drag ratio is 23.7, slightly lower than the value computed by Benad, 25. This difference might come from a underestimation of the wave drag, since a vortex lattice method with compressibility correction was used by Benad. In particular, he selects the profiles by engineering judgement and states that transonic flow numerical studies are required to verify his assumptions and estimations [8].

The two major transformations of the Flying V configuration are the wing planform and the cabin cross sections. They are compared to the results of conceptual study in Section 4.8.1 and Section 4.8.2 respectively.

[1] Nasa Common Research Model. Retrieved in September 20, 2016 from https://commonresearchmodel.larc.nasa.gov/geometry/vertical-tail-geometry/

4.8.1. Wing Planform Modification

In this project, transonic flow simulations are run in order to assess the results of the conceptual design. In addition, a stepwise design procedure is followed in order to find the best aerodynamic configuration. The planform resulting from this preliminary aerodynamic design is compared to the conceptual design in Figure 4.11. The most visible modification is the increase in outboard sweep angle from 15° to 38°: this allows to avoid the generation of a strong shock wave at the design cruise condition. Therefore, the overall length of the Flying V increases of 10 m: it is still smaller than the length of the A350-900, which is 66.8 m as shown on the right hand side of Figure 4.11. The great aerodynamic efficiency improvement is achieved by modifying also the profiles shape.

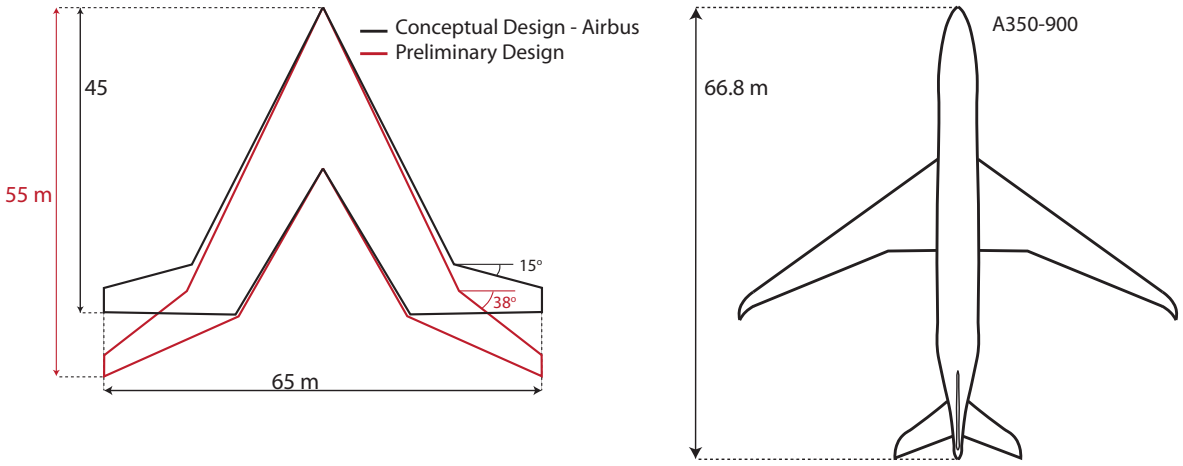

Figure 4.11: Flying V planform comparison. The A350-900 planform is shown on the right hand side

4.8.2. Cabin Cross Section Transformation

As thoroughly described in Section 2.4, the idea of the cylindrical cabin section is abandoned in favour of a more flexible oval section. In Figure 4.12, the cabin section of the conceptual study is reported on the left hand side: being a A320 type of cabin, it accommodates 6 passengers per row with a single aisle. The new oval cabin, whose cross section is reported on the right hand side of Figure 4.12, is twin-aisle with 10 passengers per row. This arrangement is different from the one proposed by Benad, with the cargo compartment placed behind the passenger cabin. According the new layout, the cargo compartment is placed outboard, as explained in Section 2.4.2.

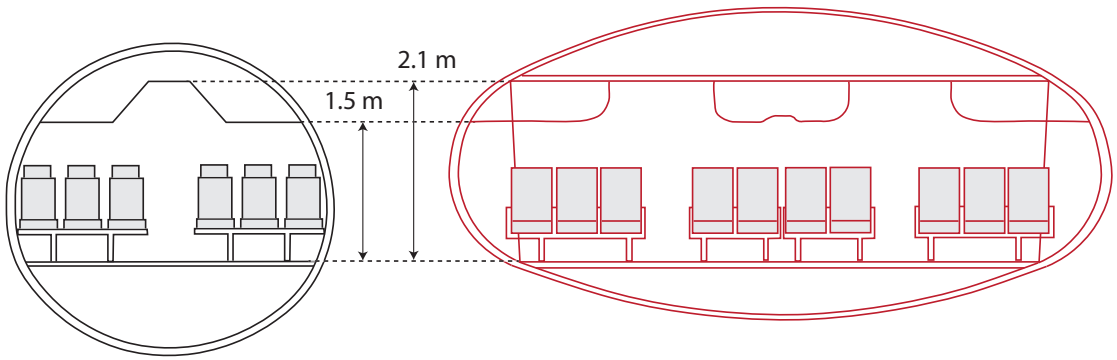

Figure 4.12: Cabin cross section: from cylindrical (conceptual design) to oval

5

Conclusions and Recommendations

5.1. Conclusions

Commercial transport aviation has been expanding in the last decades, and an additional rapid growth is predicted for the coming years: this brings about a remarkable environmental impact, pollution and noise. Moreover, the conventional tube-and-wing configuration has been extensively exploited and optimized. Therefore, manufacturers and researchers have been investigating unconventional configurations, such as flying wings and blended wing bodies. These arrangements boast relevant aerodynamic and structural benefits: a low wetted area and interference drag, and an advantageous weight distribution. On the other hand, non-cylindrical fuselages, typical of these configurations, entail a relevant structural penalty, and control and stability issues must be tackled carefully. The Flying V is a concept investigated at Technishe Universitat Berlin in collaboration with the Future Project Office at Airbus GmbH in order to overcome the mentioned limitations. The results of the conceptual study are really promising: the aerodynamic and structural performances are better than the A350-900. Therefore, the goal of the present research is to perform the aerodynamic design of the Flying V and verify the initial estimations with in-depths analyses, in order to assess whether the Flying V is aerodynamically more efficient than the reference conventional configuration, the NASA Common Research Model.

The aerodynamic design approach chosen for the Flying V is stepwise: a multi-fidelity design space exploration, which uses a vortex lattice method and an Euler solver, is adopted to move towards a feasible configuration, then SU2 Euler optimization for minimum cruise drag is used to find the optimum design. In particular, two different optimization paths are tested: a dual step optimization, characterised by a planform optimization followed by an airfoil optimization, and a single step procedure, in which planform and airfoil parameters are simultaneously varied. The differential evolution optimization algorithm is used for this purpose. An Euler solver on an unstructured grid is used to accurately compute the wave and vortex-induced drag, whereas an empirical module is created to estimate the profile drag, since viscosity is neglected by the Euler flow model. The geometry is created by a multi model generator according to a parametrization based on 10 wing planform variables, 43 profile parameters and 3 fin variables. Subsequently, the grid is automatically generated and fed into the Euler solver. The twins fins are sized separately according to stability and control requirements, and then added to the wing.

The aerodynamic design is performed at one single cruise point, namely: Mach number equal to 0.85, lift

coefficient of 0.26, and altitude of 13,000 m. The baseline configuration, resulting from the conceptual study, features too much load in the outboard wing: a strong shock wave appears at a really aft location, where the maximum Mach number is 1.47, the lift distribution is not optimal, and a considerable pitch down needs to be balanced. The improved-baseline configuration, resulting from the design space exploration, achieves better aerodynamic performances. The outer wing is swept back from 15° to 30° and twisted down, hence the lift distribution is closer to a triangular-elliptical one. The wave and vortex induced drag components are reduced by 16 counts and the pitching moment coefficient is halved. The dual step optimization entails a remarkable improvement in lift to drag ratio from 22.8 to 23.5, whereas the single step procedure allows a further cruise drag reduction (the lift to drag ratio is 23.7). The wing area resulting from both the procedure is 883 m^2, slightly lower than the initial one: this contributes to the decrease in profile drag. Moreover, the maximum local Mach number of the two optimized configurations is 1.25, which represents a great improvement. This is mainly achieved by the outboard wing profiles optimization: the leading edge radius is reduced, front loading is introduced and rear loading is partially removed. The single step procedure involves a considerable reduction of computational time, from 167 to 125 hours (dual step optimization), and at the same time produces better aerodynamic results. Not less importantly, the maximum lift to drag ratio of the optimized Flying V configuration has a plateau at lift coefficients higher than the design one: this means that this configuration has acceptable aerodynamic off-design performances. Finally, the aerodynamic performances of the Flying V are compared to the ones of the NASA Common Research Model, state of the art conventional configuration, obtained with the same solver and comparable mesh refinement. The NASA configuration maximum cruise lift to drag ratio is assessed to be 18.9, hence the single step optimized Flying V proves to be 25% more efficient from an aerodynamic perspective at the design cruise condition. The Flying V proves to be a promising concept and this investigation can be regarded as one of the initial steps of a long iterative design and development procedure. It is now worth investigating low speed performances and maximum lift capabilities, and, at the same time, dealing with other design disciplines.

5.2. Recommendations for Future Work

While this study has been successful in addressing the aerodynamic design of the Flying V and results prove to be satisfactory, additional research is required to investigate other aspects concerning the overall design of the Flying V.

First of all, from an aerodynamic perspective, the twin fins are treated separately from the wing and sized according to semi-empirical correlations. Therefore, the interference between wing and fins is not accurately estimated: this interference can be beneficial in terms of induced drag and detrimental in terms of wave drag. Hence, a future development should take into account this interference and optimize the full design. In particular, the Euler flow model is selected for this project since it provides an acceptable accuracy at a relatively low computational cost. During future studies, higher fidelity flow models, such as Euler coupled with boundary layer equations and RANS, should be used.

In addition, since this work focuses only on cruise conditions, low speed characteristics require a dedicated study in order to demonstrate that the Flying V has an acceptable maximum lift coefficient without high lift devices. In particular, the field performances must be compatible with existing airports.

Furthermore, the weight and centre of gravity location estimations are based on some assumptions that need verification. This will be provided by the results of the structural sizing module, which is being concurrently created. Moreover, it is worth performing a multidisciplinary design optimization in order to address multiple disciplines at the same time: in this case, the weight estimation can be included in the loop so that

a change in geometry can be translated into a different aircraft weight.

Finally, a preliminary idea of cabin layout with cargo compartment placed outboard is provided; however, galleys and lavatories arrangement, and more operational aspects such as doors installations are not taken into account. Also emergency evacuation procedures have to be carefully addressed by future work.

Bibliography

[1] R. Martinez-Val. Flying Wings. A New Paradigm for Civil Aviation? *Acta Polytechnica*, 47(1), 2007.

[2] R. Martinez-Val, E. Perez, J. Puertas, and J. Roa. Optimization of planform and cruise conditions of a transport flying wing. In *Proceedings of the Institution of Mechanical Engineers, Part G: Journal of Aerospace Engineering*, volume 224, pages 1243–1251, 2010.

[3] E. Torenbeek. Blended Wing Body and All-Wing Airliners. In *European Workshop on Aircraft Design Education (EWADE)*, Samara, 2007.

[4] R. Martiénez-Val, E. Pérez, P. Alfaro, and J. Pérez. Conceptual design of a medium size flying wing. In *Proceedings of the Institution of Mechanical Engineers, Part G: Journal of Aerospace Engineering*, volume 221, pages 57–66, 2007.

[5] A. L. Bolsunovsky, N. P. Buzoverya, B. I. Gurevich, V. E. Denisov, A. I. Dunaevsky, L. M. Shkadov, O. V. Sonin, A. J. Udzhuhu, and J. P. Zhurihin. Flying wing - Problems and decisions. *Aircraft Design*, 4(4): 193–219, 2001.

[6] R. Martinez-Val, J. F. Palacin, and E. Perez. The evolution of jet airliners explained through the range equation. In *Proceedings of the Institution of Mechanical Engineers, Part G: Journal of Aerospace Engineering*, volume 222, pages 915–919, 2008.

[7] E. Torenbeek. *Synthesis of Subsonic Airplane Design*. Delft University Press, 1976.

[8] J. Benad. Design of a commercial aircraft for high-subsonic speed as a flying wing configuration. Technical report, Airbus, Berlin, 2015.

[9] J. C. Vassberg, M. A. DeHaan, S. M. Rivers, and R. A. Wahls. Development of a Common Research Model for Applied CFD Validation Studies. In *26th AIAA Applied Aerodynamics Conference*, number August, Honolulu, 2008.

[10] R. M. Wood and S. X. S. Bauer. Flying Wings/ Flying Fuselages. In *39th AIAA Aerospace Sciences Meeting & Exhibit*, number January, Reno, 2001.

[11] V. Denisov, L. Shkadov, and S Chernyshev. The Flying Wing Concept - chances and risks. In *AIAA International Air and Space Symposium and Exposition: The Next 100 Years*, number July, pages 1–11, Dayton, 2003.

[12] B. Mialon, T. Fol, and C.. Bonnaud. Aerodynamic optimization of subsonic flying wing configurations. In *20th AIAA Applied Aerodynamics Conference*, number June, pages 1–7, St. Louis, 2002.

[13] T. I. Saeed and W. R. Graham. Design Study for a Laminar-Flying-Wing Aircraft. *Journal of Aircraft*, 52 (5):1373–1385, 2015.

[14] M. Zhang, A. Rizzi, P. Meng, R. Nangia, R. Amiree, and O. Amoignon. Aerodynamic Design Considerations and Shape Optimization of Flying Wings in Transonic Flight. In *12th AIAA Aviation Technology, Integration, and Operations (ATIO) Conference and 14th AIAA / ISSM*, number September, pages 1–17, Indianapolis, 2012.

[15] C. A. Mader. Stability-Constrained Aerodynamic Shape Optimization of Flying Wings. *Journal of Aircraft*, 50(5), 2013.

[16] R. H. Liebeck. Design of the Blended Wing Body Subsonic Transport. *Journal of Aircraft*, 41(1):10–25, 2004.

[17] D. Roman, R. Gilmore, and S. Wakayama. Aerodynamics of high-subsonic blended-wing-body configurations. In *41st Aerospace Sciences Meeting and Exhibit*, number January, pages 1–9, Reno, 2003.

[18] N. Qin, A. Vavalle, A. Le Moigne, M. Laban, K. Hackett, and P. Weinerfelt. Aerodynamic considerations of blended wing body aircraft. *Progress in Aerospace Sciences*, 40(6):321–343, 2004.

[19] N. Qin, A. Vavalle, A. Le Moigne, M. Laban, K. Hackett, and P. Weinerfelt. Aerodynamic Studies for Blended Wing Body Aircraft. In *9th AIAA/ISSMO Symposium on Multidisciplinary Analysis and Optimization*, number September, pages 1–11, Atlanta, 2002.

[20] T. Pambagjo, K. Nakahashi, S. Obayashi, and K. Matsushima. Aerodynamic design of a medium size blended-wing-body airplane. In *39th Aerospace Sciences Meeting and Exhibit*, number January, Tohoku, 2001.

[21] T. A. Reist and D. W. Zingg. Aerodynamic Design of Blended Wing-Body and Lifting-Fuselage Aircraft. In *34th AIAA Applied Aerodynamics Conference*, Washington, D.C., 2016.

[22] P. Li, B. Zhang, Y. Chen, C. Yuan, and Y. Lin. Aerodynamic design methodology for blended wing body transport. *Chinese Journal of Aeronautics*, 25(4):508–516, 2012.

[23] W. H. Mason. Transonic Aerodynamics of airfoils and wings. *Notes in Configuration Aerodynamics, Virginia Tech*, 4, 2006.

[24] C. L. Rumsey and S. X. Ying. Prediction of high hift: review of present CFD capabilities. *Progress in Aerospace Sciences*, 38:145–180, 2002.

[25] S. Deck, F. Gand, V. Brunet, and S. B. Khelil. High-fidelity simulations of unsteady civil aircraft aerodynamics : stakes and perspectives . Application of zonal detached eddy simulation Subject Areas : Author for correspondence :. *Philosophical Transactions of the Royal Society of London A: Mathematical, Physical and Engineering Sciences*, 372, 2014.

[26] R. Vos and S. Farokhi. *Introduction to Transonic Aerodynamics*. Springer, 2015. ISBN 9789401797467.

[27] M. I. Gerritsma. *Computational Fluid Dynamics*. Delft University Press, Delft, 2002.

[28] W. Mason. Applied Computational Aerodynamics, Volume 1: Foundations and Classical Pre-CFD Methods, 1992.

[29] O. Gur, W. H. Mason, and J. A. Schetz. Full Configuration Drag Estimation. In *27th AIAA Applied Aerodynamics Conference*, number June, San Antonio, 2009.

[30] EASA. Certification Specifications for Large Aeroplanes. Technical Report September, 2008.

[31] OACI and ICAO. Annex 14 – Aerodome Reference Code. Technical report, 2001.

[32] FAA. Part 25-Airworthiness standards: Transport category airplanes. Technical report, 1974.

[33] M. Zhang, A. Rizzi, P. Meng, R. Nangia, R. Amiree, and O. Amoignon. Aerodynamic Design Considerations and Shape Optimization of Flying Wings in Transonic Flight. In *12th AIAA Aviation Technology, Integration, and Operations (ATIO) Conference and 14th AIAA / ISSM*, number September, pages 1–17, Indianapolis, 2012.

[34] G. La Rocca and M. van Tooren. A Knowledge Based Engineering Approach to Support Automatic Generation of FE Models in Aircraft Design. In *45th AIAA Aerospace Sciences Meeting and Exhibit*, 2007.

[35] G. La Rocca. Knowledge based engineering: Between AI and CAD. Review of a language based technology to support engineering design. *Advanced Engineering Informatics*, 26(2):159–179, 2012.

[36] R. Storn and K. Price. Differential Evolution: A Simple and Efficient Heuristic for Global Optimization over Continuous Spaces. *Journal of Global Optimization*, 11:341–359, 1997.

[37] V. V. De Melo and G. L. C. Carosio. Evaluating differential evolution with penalty function to solve constrained engineering problems. *Expert systems with applications*, 39:7860–7863, 2012.

[38] E. Obert. *Aerodynamic design of transport aircraft*. IOS Press BV, 2009.

[39] C. D. Perkins and R. E. Hage. Airplane performance stability and control. *Wiley, J.*, 1949.

[40] D. P. Raymer. *Aircraft Design: A Conceptual Approach*. American Institute of Aeronautics and Astronautics, 2004.

[41] J. P. Campbell and M. O. McKinney. Summary of Methods for calculating Dynamic Lateral Stability and Response and for estimating Lateral Stability Derivatives. *NACA Report1098*, 1951.

[42] M. H. Sadraey. *Aircraft design: A systems engineering approach*. John Wiley \& Sons, 2012.

[43] EASA. Type certificate data sheet: Rolls-Royce plc Trent XWB series engines. Technical report, 2013.

[44] R. Vos, F. J. J. M. M. Geuskens, and M. F. M. Hoogreef. A New Structural Design Concept for Blended Wing Body Cabins. In *53rd AIAA/ASME/ASCE/AHS/ASC Structures, Structural Dynamics and Materials Conference*, number April, Honolulu, 2012.

[45] H. Kim, D. Harding, D. T. Gronstal, and M. Liou. Design of the Hybrid Wing Body with Nacelle : N3 - X Pr opulsion - Airframe Configuration. In *34th AIAA Applied Aerodynamics Conference*, number June, Washington, D.C., 2016. doi: 10.2514/6.2016-3875.

[46] T. Korakianitis. Prescribed-Curvature-Distribution Airfoils for the Preliminary Geometric Design of Axial-Turbomachinery Cascades. *Journal of Turbomachinery*, 115(2):325, 1993.

[47] K. M. Selvan. On the effect of Shape Parameterization on Aerofoil Shape Optimization. *IJRET: International Journal of Research in Engineering and Technology*, 2015.

[48] V. Braibant and C. Fleury. Shape optimal design using B-splines. *Computer Methods in Applied Mechanics and Engineering*, 44(3):247–267, 1984.

[49] M. H. Straathof, M. J. L. van Tooren, M. Voskuijl, and B. Koren. Aerodynamic Shape Parameterisation and Optimisation of Novel Configurations. In *Proceedings of the 2008 Royal Aeronautical Society Annual Applied Aerodynamics Research Conference*, London, 2008.

[50] B. M. Kulfan. Universal Parametric Geometry Representation Method. *Journal of Aircraft*, 45(1):142–158, 2008.

[51] A.I. Azamatov, J. W. Lee, Y. H. Byun, and S. H. Kim. Advanced configuration generation technique for the complex aircraft geometry. *IEEE/ASME International Conference on Advanced Intelligent Mechatronics, AIM*, pages 1141–1146, 2008. doi: 10.1109/AIM.2008.4601823.

[52] M. H. Straathof. Parametric study of the class-shape-refinement-transformation method. *Optimization. A Journal of Mathematical Programming and Operations Research*, 61(6):637–659, 2012.

[53] F. Palacios, M. R. Colonno, A. C. Aranake, A. Campos, S. R. Copeland, T. D. Economon, A. K. Lonkar, T. W. Lukaczyk, Thomas W. R. Taylor, and J. J. Alonso. Stanford University Unstructured (SU 2): An open-source integrated computational environment for multi-physics simulation and design . In *51st AIAA Aerospace Sciences Meeting including the New Horizons Forum and Aerospace Exposition*, number January, Grapevine, 2013.

[54] J. D. Anderson. *Computational Fluid Dynamics - The basics with applications*. McGraw-Hill, 1995. ISBN 0070016798.

[55] W. M. Chan, R. J. Gomez, S. E. Rogers, and P. G. Buning. Best practices in overset grid generation. In *32nd AIAA Fluid Dynamics Conference*, St. Louis, 2002.

[56] J. Roskam. *Airplane Design: Preliminary Sizing of Airplanes*. DARcorporation, 1985.

[57] P. R. Woodard, J. T. Batina, and H. T .Y. Yang. Quality assessment of two and three-dimensional unstructured meshes and validation of an upwind Euler flow solver. *NASA Technical Memorandum 104215*, 1992.

[58] V. Schmitt and F. Charpin. "Pressure Distributions on the ONERA-M6-Wing at Transonic Mach Numbers," Experimental Data Base for Computer Program Assessment. Technical report, Fluid Dynamics Panel Working Group 04, AGARD AR 138, 1979.

[59] J. Mayeur, A. Dumont, D. Destarac, and V. Gleize. RANS simulations on TMR test cases and M6 wing with the Onera elsA flow solver. In *53rd AIAA Aerospace Sciences Meeting*, Kissimmee, 2015.

[60] N. Durrani and N. Qin. Comparison of RANS, DES and DDES results for ONERA M-6 Wing at transonic flow speed using an in-house parallel code. In *49th AIAA Aerospace Sciences Meeting*, number January, Orlando, 2011.

[61] F. Palacios, T. D. Economon, A. D. Wendorff, and J. J. Alonso. Large-scale aircraft design using SU2. In *53rd AIAA Aerospace Sciences Meeting*, number January, pages 1–20, Kissimmee, 2015.

[62] M. Ueno, K. Yamamoto, K. Tanaka, M. Murayama, and R. Tognaccini. Far-Field Drag Analysis of NASA Common Research Model Simulations by JAXA. In *AIAA Computational Fluid Dynamics Conference*, number June, pages 1–14, Honolulu, 2011.

[63] G. K. W. Kenway, J. R. R. A. Martins, and G. J. Kennedy. Aerostructural optimization of the Common Research Model configuration. In *15th AIAA/ISSMO Multidisciplinary Analysis and Optimization Conference*, pages 1–19, Atlanta, 2014.

[64] R. T. Whitcomb. Review of NASA supercritical airfoils. In *9th International Council of the Aeronautical Sciences Congress*, Haifa, 1974.

A

Code Documentation

In this chapter, the code of the Flying V design application within the ParaPy framework is documented.

A.1. Structure of the Code

In this paragraph, the structure of the code is explained and the most relevant classes are outlined into detail. A UML diagram is displayed in Figure A.1 to show the relationships between different classes and objects. In Figure A.2, the ParaPy interface is displayed.

The main class is named *Aircraft*: it is composed of geometry parts (*outer_shape*, *fuselage*, *wing_structure* and *pylon_and_engine*) and capability parts (*PaxCapacity*, *CADoutput*, *AeroAnalysis* and *performance*). The *Wing* class is composed of some inboard profiles, outboard profiles and wing trunks: for sake of synthesis, the names of all of them are not reported in the UML diagram of Figure A.1. Furthermore, a dotted line is used to indicate the dependency between the *AerodynamicDiscipline* class and *ViscousDrag* and *ViscousDragNacelle*: in particular the attributes *cd_viscous_nacelle*, *cd_viscous_lifting_body* and *cd_viscous_pylons* are estimated by using the above mentioned classes. The classes *Fuselage* and *WingStructure* are mainly created by Luuk van der Schaft, hence he will provide an extensive documentation about them.

It is important to briefly explain the ParaPy syntax. A ParaPy class is composed of: a *ClassName*, *Superclass* if the class is built from another class and *Slots*, which define the engineering relations. Three different types of slots can be distinguished:

- Inputs, which indicate information that the object instance uses when it is created.
- Attributes, which specify engineering rules associated to the class.
- Parts, which, unlike attributes, create a parent-child relation with another class. Hence, they represent instantiations of other classes.

In the following sections, the inputs, attributes and parts of the most relevant classes are described.

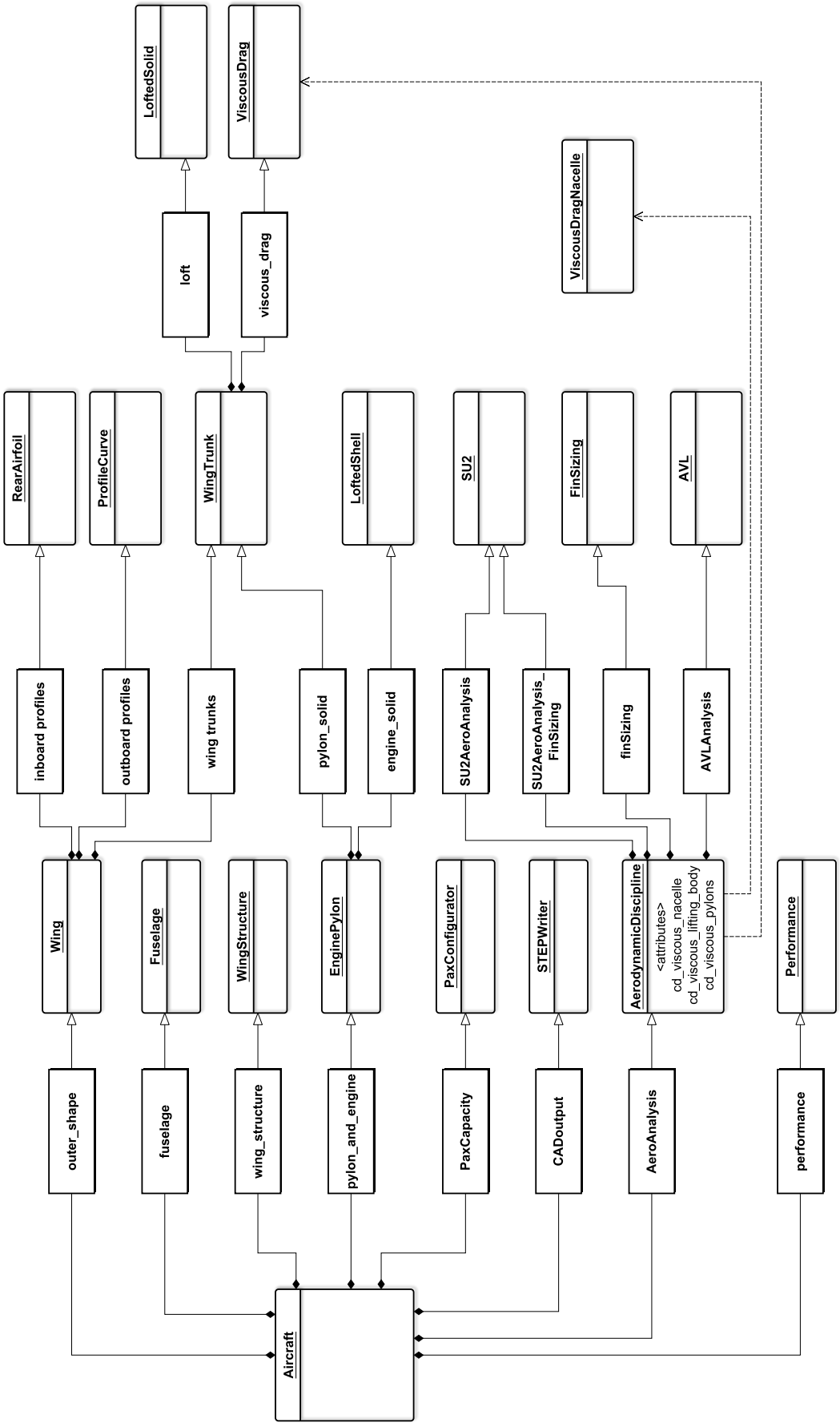

Figure A.1: UML diagram of the Flying V design application developed within the ParaPy framework

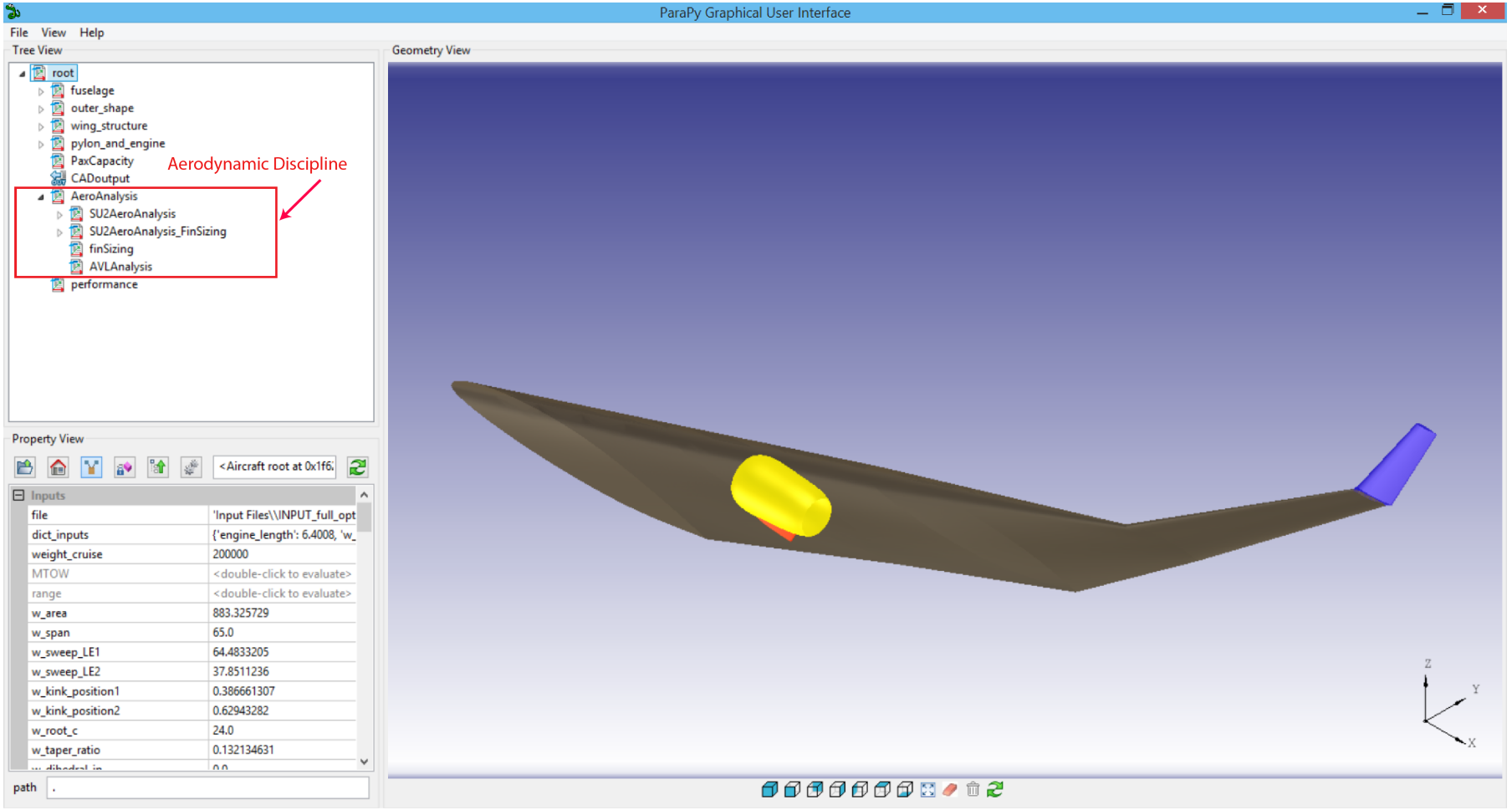

Figure A.2: ParaPy GUI: objects tree (top left), input management (bottom left) and geometry view (right)

A.2. User's Input File

The user's input file is a text file, where the geometry design parameters and some mission details are defined. The user may either change the input file or directly set the values of the inputs in the ParaPy graphical user interface (GUI), shown in Figure A.2. The different entries of the input file are explained in Table A.1.

	Name	Description
Wing planform variables	*w_area*	Area (m^2)
	w_span	Span (m)
	w_sweep_LE1	Leading edge sweep angle 1 (deg)
	w_sweep_LE2	Leading edge sweep angle 2 (deg)
	w_kink_position1	Kink relative position 1 (-)
	w_kink_position2	Kink relative position 2 (-)
	w_root_c	Root chord (m^2)
	w_taper_ratio	Taper ratio (-)
	w_dihedral_in	Dihedral of the inboard part (-)
	w_dihedral_out	Dihedral of the outboard part (-)
	w_kink2_twist	Twist kink 2 (deg)
	w_tip_twist	Twist tip (deg)
Winglets/fins variables	*winglet_A*	Winglets/fins aspect ratio (-)
	winglet_dihedral	Winglets/fins dihedral (deg)
	winglet_sweep	Leading edge sweep angle (deg)
	winglet_taper_ratio	Taper ratio (-)
Oval sections parameters	*height_up_2*	H_1 of section 2 (m)
	height_cabin_2	H_2 of section 2 (m)
	height_low_2	H_3 of section 2 (m)
	height_up_3	H_1 of section 3 (m)
	height_cabin_3	H_2 of section 3 (m)
	height_low_3	H_3 of section 3 (m)
	width_floor_3	W_F of section 3 (m)
	height_up_4	H_1 of section 4 (m)
	height_cabin_4	H_2 of section 4 (m)
	height_low_4	H_3 of section 4 (m)
	width_floor_4	W_F of section 4 (m)
	height_up_5	H_1 of section 5 (m)
	height_cabin_5	H_2 of section 5 (m)
	height_low_5	H_3 of section 5 (m)
	width_floor_5	W_F of section 5 (m)
Nose cone parameters	*a_upper*	Coefficient a_{up} of the front cone ($\sqrt{\text{m}}$)
	a_lower	Coefficient a_{low} of the front cone ($\sqrt{\text{m}}$)
	e_upper	Coefficient e_{up} of the front cone ($1/\text{m}^2$)
	e_lower	Coefficient e_{low} of the front cone ($1/\text{m}^2$)

Rear airfoil parameters	*c_up_root*	c_{up} of section I (1/m)
	c_low_root	c_{low} of section I (1/m)
	z_TE_root	z_{TE} of section I (m)
	c_up_inb	c_{up} of section II (1/m)
	c_low_inb	c_{low} of section II (1/m)
	z_TE_inb	z_{TE} of section II (m)
	c_up_kink1	c_{up} of section III (1/m)
	c_low_kink1	c_{low} of section III (1/m)
	z_TE_kink1	z_{TE} of section III (m)
Outboard airfoils	*w_kink2_CST*	List of 12 CST coefficients of section IV (-)
	w_tip_CST	List of 12 CST coefficients of section V (-)
Engine-nacelles	*engine_length*	Engines nacelles length (m)
	engine_diameter	Engines nacelles diameter (m)
	engine_position_y	Engines spanwise relative position (-)
	engine_max_continuousT	Engines maximum continuous thrust (N)
Mission and speeds	*range*	Design range (m)
	cruise_mach	Cruise Mach number (-)
	cruise_altitude	Cruise altitude (m)
	takeoff_speed	Take-off speed (m/s)
Weights	*MTOW*	Maximum take-off weight (kg)
	weight_cruise	Design cruise weight (kg)

Table A.1: User's input file description

A.3. Aerodynamic Discipline Class (*AerodynamicDiscipline*)

The *AerodynamicDiscipline* class coordinates the different aerodynamic analysis modules, namely SU2, AVL and the viscous drag estimation.

	Name	Description
Inputs	*weight_cruise*	Cruise design weight (kg)
	engine_length	Engine nacelles length (m)
	engine_diameter	Engine nacelles diameter (m)
	engine_max_continuousT	Engine maximum continuous thrust (N)
	engine_position_y	Engine relative spanwise position (-)
	SU2path	Path of the SU2 aerodynamic results (*string*)
	AVLpath	Path of the AVL aerodynamic results (*string*)
	w_planform	Dictionary containing the planform variables (*dict*)
	flight_conditions	Dictionary containing the flight conditions (*dict*)
Attributes	*cd_viscous_lifting_body*	Profile drag coefficient of wing and fins (-) (from class *ViscousDrag*)
	wetted_area_lifting_body	Wetted area of wing and fins (m^2)
	cd_viscous_nacelle	Profile drag coefficient of engine nacelles (-) (from class *ViscousDragNacelle*)
	cd_viscous_pylons	Profile drag coefficient of engine pylons (-) (from class *ViscousDrag*)
	cd_viscous_total	Total profile drag coefficient (-)
	lift_to_drag	Flying V lift to drag ratio (-)
Parts	*SU2AeroAnalysis*	SU2 Aerodynamic analysis (type of *SU2*)
	SU2AeroAnalysis_FinSizing	SU2 Aerodynamic analysis for twin fins sizing (type of *SU2*)
	finSizing	Fin sizing (type of *FinSizing*)
	AVLAnalysis	AVL aerodynamic analysis (type of *AVL*)

Table A.2: Aerodynamic discipline class

A.3.1. AVL Analysis Class (*AVL*)

	Name	Description
Inputs	*AVLpath*	Path of the AVL aerodynamic results (*string*)
	AVLfilename	Name of the AVL input file (*string*)
	span	Wing span (m)
	MAC	Wing mean aerodynamic chord (m)
	S	Wing reference area (m^2)
	le_points	List of the leading edge points of different spanwise sections (*list of points*)
	chords	List of wing chords at different spanwise sections (*list*, m)
	twists	List of wing twist angles at different spanwise sections (*list*, deg)
	mach_number	Mach number (-)
	flight_speed	Flight speed (m/s)
	rho	Air density (kg/m^3)
	alpha	Angle of attack (deg)
	cl	Lift coefficient (-)
	is_cl_input	Input to select whether the angle of attack or lift coefficient is given (*boolean*)
	control_chord_ratio_kink1	Chord ratio of the elevon at the kink1 position (-)
	control_chord_ratio_tip	Chord ratio of the elevon at the tip position (-)
	CG_x	Centre of gravity x location for moment calculations (m)
Attributes	*hinge_line_angle*	Angle between elevons hinge line and y axis (deg)
	control_chord_ratio_kink2	Chord ratio of the elevon at the kink2 position, given a straight hinge line (-)
	Airfoil_files	Creation of airfoil files, required by AVL (from method *create_dat_file_from_points*)
	AVLFile	Writing of the AVL input file in which moments are calculated about *CG_x* (from class *AVLWriter*)
	AVL_output	Runs AVL with *AVLFile* and returns the output (from class *run_AVL*)
	CG_allowed	List of three allowed CG positions at 2.5, 6 and 10% MAC ahead of neutral point, which is among *AVL_output* (*list*, m)
	AVLFile_CG	Writing of the AVL input file in which moments are calculated about a point of *CG_allowed* (from class *AVLWriter*)
	AVL_output_CG	Runs AVL with *AVLFile_CG* and returns the output (from class *run_AVL*)
	trim_output	Runs AVL with *AVLFile* in the trim mode and returns the output (from class *run_AVL*)
	lift_plot	Display lift distribution of *AVL_output*
	cl_plot	Display lift coefficient distribution of *AVL_output*

Table A.3: AVL analysis class

A.3.2. SU2 Analysis Class (*SU2*)

	Name	Description
Inputs	*half_model*	If True only half Flying V is analysed (*boolean*)
	SU2path	Path of the SU2 aerodynamic results (*string*)
	SU2filename	Name of the SU2 input file (*string*)
	far_field_width	Width of the computational domain (m)
	far_field_length	Length of the computational domain (m)
	far_field_height	Height of the computational domain (m)
	problem_type	Type of problem, direct or adjoint (*string*)
	span	Wing span (m)
	MAC	Wing mean aerodynamic chord (m)
	S	Wing reference area (m^2)
	mach_number	Mach number (-)
	pressure	Air pressure (Pa)
	temperature	Air temperature (K)
	alpha	Angle of attack (deg)
	cl	Lift coefficient (-)
	is_cl_input	Input to select whether the angle of attack or lift coefficient is given (*boolean*)
	beta	Sideslip angle (deg)
	ref_moment_x	Reference x location for moment calculations (m)
	marker_euler	List of markers where the Euler boundary condition applies (*list, string*)
	marker_far	List of markers where the far field conditions apply (*list, string*)
	marker_sym	List of markers where the symmetry condition applies (*list, string*)
	y_cp	Relative spanwise position at which the pressure coefficient distribution is plotted (-)
Attributes	*FusedSolidToMesh_faces*	List of faces of the *FusedSolidToMesh* (*list*)
	unv_mesh	Mesh in the unv format, Salome output from part *mesh*
	su2_mesh	Mesh translated into the su2 format (method *write_su2*)
	SU2File	Configuration file, input of SU2 (from class *SU2Writer*)
	runSU2	Run SU2
	output	Read SU2 output (method *read_SU2output_forces*)
	load_plot	Display the lift distribution
	cp_plot	Display the pressure coefficient distributions at the selected *y_cp*
	pressure_contours	Open the solution file in Paraview to view the pressure contours
Parts	*mesh*	Mesh part (type of *WingMesh*)
	FusedSolidToMesh	Flying V part that has to be meshed (type *SubtractedSolid*)
	far_field	Computational domain (type of *Box*)

Table A.4: SU2 analysis class

A.3.3. Fin Sizing Class (*FinSizing*)

	Name	Description
Inputs	*span*	Wing span (m)
	MAC	Wing mean aerodynamic chord (m)
	S	Wing reference area (m^2)
	C_N_beta_NoFins	Yawing coefficient derivative without fins, computed by SU2 (1/rad)
	C_N_beta_target	Target directional static coefficient derivative (1/rad)
	Mach	Mach number (-)
	w_tip_x_LE	x position of the leading edge of the wing tip (m)
	ref_moment_x	Reference x location for moment calculations (m)
	root_chord_fin	Fin root chord (m)
	engine_max_continuousT	Engine maximum continuous thrust (N)
	engine_position_y	Engine relative spanwise position (-)
	takeoff_speed	Aircraft take-off speed (m/s)
Attributes	*S_fin*	Fin area resulting from the sizing (m^2)
	height_fin	Fin height resulting from the sizing (m^2)
	effectiveA_factor	Coefficient to account for end plate effect (-) [40]
	fin_arm	Fin arm from *ref_moment_x* (m)
	C_L_alpha_Fin	Fin lift slope (1/rad) [40]
	C_N_beta	Flying V yawing coefficient derivative (1/rad)
	C_N_delta_rudder	Rudder contribution to yawing moment coefficient (1/rad), Equation (2.9)
	rudder_deflection_OEI	Rudder contribution in OEI condition (deg), Equation (2.8)
	rudder_deflection_crosswind	Rudder contribution in maximum crosswind condition (deg), Equation (2.10)
	fin_optimal_shape	Run optimization procedure for fin sizing
	A_fin	Fin aspect ratio resulting from the sizing (-)
	sweep_fin	Fin leading edge sweep angle resulting from the sizing (deg)
	taper_fin	Fin taper ratio resulting from the sizing (-)

Table A.5: Fin sizing class

A.3.4. Viscous Drag Estimation Class (*ViscousDrag*)

	Name	Description
Inputs	*S*	Wing reference area (m^2)
	MAC	Mean aerodynamic chord (m)
	thickness_to_chord	Average maximum thickness to chord ratio (-)
	sweep	Mid chord sweep angle (deg)
	S_wet	Wetted area (m^2)
	mach	Mach number (-)
	speed	Speed (m/s)
	viscosity	Kinematic air viscosity (m^2/s)
	roughness	Skin roughness value used to estimate the cut-off Reynolds number (m)
Attributes	*reynolds*	Reynolds number (-)
	reynolds_cutoff	Cut-off Reynolds number (-)
	skin_friction_coeff	Skin friction coefficient for fully turbulent wing (-), Equation (2.20)
	form_factor	Form factor for lifting bodies to account for form drag due to separation (-), Equation (2.21)
	viscous_drag_coeff	Profile drag coefficient (-), Equation (2.19)

Table A.6: Viscous module class for wing, fin and pylon profile drag estimation, based on the empirical equations outlined in Section 2.5.1

A.3.5. Nacelles Viscous Drag Estimation Class (*ViscousDragNacelle*)

	Name	Description
Inputs	*S*	Wing reference area (m^2)
	length	Nacelles characteristic length (m)
	diameter	Nacelles diameter (m)
	S_wet	Nacelles wetted area (m^2)
	mach	Mach number (-)
	speed	Speed (m/s)
	viscosity	Kinematic air viscosity (m^2/s)
	roughness	Skin roughness value used to estimate the cut-off Reynolds number (m)
Attributes	*reynolds*	Reynolds number (-)
	reynolds_cutoff	Cut-off Reynolds number (-)
	skin_friction_coeff	Skin friction coefficient for fully turbulent wing (-), Equation (2.20)
	form_factor	Form factor for lifting bodies to account for form drag due to separation (-), Equation (2.22)
	viscous_drag_coeff	Profile drag coefficient (-), Equation (2.19)

Table A.7: Viscous module class for nacelles profile drag estimation, based on the empirical equations presented in Section 2.5.1

A.4. Performance Class (*Performance*)

The *Performance* class computes the fuel required to complete a certain mission. It is based on the method outlined in Section 2.6.1.

	Name	Description
Inputs	*MTOW*	Aircraft maximum take-off weight (kg)
	range	Mission range (m)
	speed	Cruise speed (m/s)
	c_T	Specific fuel consumption (N/Ns)
	lift_to_drag	Cruise lift to drag ratio (-)
Attributes	*w_end_to_w_start*	Cruise fuel fraction (-)
	w_fuel	Cruise fuel weight (kg)
	w_fuel_to_MTOW	Ratio between fuel weight and maximum take-off weight (-)

Table A.8: Performance analysis class

A.5. Payload Capacity Class (*PaxConfigurator*)

The *PaxConfigurator* class computes the amount of passengers that can be accommodated in the Flying V cabin. It follows the procedure explained in Section 2.6.2.

	Name	Description
Inputs	*pax_cabin*	Cabin loft to estimate the total cabin area (type of *loft*)
	lavatories_area	Area dedicated to lavatories (m^2), Table 2.6
	galleys_area	Area dedicated to galleys (m^2), Table 2.6
	cockpit_area	Cockpit area (m^2), Table 2.6
	cargo_area	Area addressed to cargo (m^2), Table 2.6
	pax_per_area	Number of passengers per square meter (pax/m^2), Table 2.6
Attributes	*floor_area*	Floor area available for passengers (m^2)
	pax_capacity	Maximum number of passengers in the economy configuration (-)

Table A.9: Payload capacity class

B

Relation between Vorticity and Entropy Jump in Inviscid Flows

The Euler equations represent a mathematical model of compressible flows in which the effects of viscosity, heat conduction and external heating can be neglected. The differential form of the Euler equation is:

$$\frac{\partial \rho}{\partial t} + \mathbf{u} \cdot \nabla \rho + \rho \nabla \cdot \mathbf{u} = 0 \tag{B.1}$$

$$\frac{\partial \mathbf{u}}{\partial t} + (\mathbf{u} \cdot \nabla)\mathbf{u} + \frac{\nabla p}{\rho} = 0 \tag{B.2}$$

$$\frac{\partial e}{\partial t} + (\mathbf{u} \cdot \nabla)e + \frac{p}{\rho} \nabla \cdot \mathbf{u} = 0 \tag{B.3}$$

In which ρ is the flow density, $\mathbf{u}$ is the velocity vector, p the pressure and e the specific energy. Equations (B.1) to (B.3) represent the conversation of mass, velocity momentum and energy. From the first law of thermodynamics:

$$T \nabla s = \nabla h - \frac{1}{\rho} \nabla p \tag{B.4}$$

Where s is the specific entropy and h the specific enthalpy. Then, from the vectorial identity:

$$(\mathbf{u} \cdot \nabla)\mathbf{u} = \nabla(\frac{1}{2}\mathbf{u} \cdot \mathbf{u}) - \mathbf{u} \times (\nabla \times \mathbf{u}) \tag{B.5}$$

In which $(\nabla \times \mathbf{u})$ is named vorticity ($\mathbf{w}$). By plugging Equation (B.4) and Equation (B.5) in Equation (B.2), the following expression is derived:

$$\frac{\partial \mathbf{u}}{\partial t} + \nabla(\frac{1}{2}\mathbf{u} \cdot \mathbf{u}) - \mathbf{u} \times \mathbf{w} + \nabla h - T \nabla s = 0 \tag{B.6}$$

Since the $\frac{1}{2}\mathbf{u} \cdot \mathbf{u} + h$ equals the total specific enthalpy H, the Crocco's well know theorem can be derived:

$$\frac{\partial \mathbf{u}}{\partial t} + -\mathbf{u} \times \mathbf{w} + \nabla H - T \nabla s = 0 \tag{B.7}$$

This theorem shows that vorticity is not only related to the viscous forces within the boundary layer. In inviscid flows, vorticity is created by entropy gradients (∇s), total enthalpy gradients (∇H) and unsteady effects ($\frac{\partial \mathbf{u}}{\partial t}$). In transonic regime, the flow accelerates and is subsequently slowed down by a shock wave: the second law of thermodynamics states the a shock wave is characterised by an entropy jump. This proves that shock waves can be captured by the model if the flow is assumed to be rotational, namely with non-zero vorticity [26]. Therefore, the Euler model is the simplest one capable of capturing shock waves.